

TiO₂ photocatalysis in Portland cement systems: fundamentals of self cleaning effect and air pollution mitigation

By Andrea Folli,
M. Sc., University of Milan, ITALY

A thesis presented for the degree of Doctor of Philosophy
at the University of Aberdeen

Department of Chemistry

University of Aberdeen

2010

Declaration

I hereby declare that this thesis:

1. has been composed by Andrea Folli, i.e. the candidate for the degree of Doctor of Philosophy;
2. has not been accepted in any previous application for a degree;
3. has been entirely done by the candidate;
4. all quotations have been distinguished by quotation marks and the sources of information specifically acknowledged.

Aberdeen, 13.10.2010

Andrea Folli

Acknowledgements

...da chimico un giorno avevo il potere

di sposar gli elementi e farli reagire...

”Un chimico”, **Fabrizio De André**

When I look back at the years of my PhD in Aberdeen I see without doubt one of the best periods of my life. Years of discovery: personal discovery above all. I discovered new characteristics and features about myself that I did not know existed. I discovered the thrill of jumping into an unknown culture without properly speaking the language. Along with the day by day quest of learning; learning how to integrate, learning how to handle situations and events far different from what I had learnt from my own culture, yet finding myself at home from the very first moment. I discovered how important it was to question myself and what I do, because my own reality holds its own perspective. I discovered that if I embrace any point of view, any different opinions and any critics I can abandon fear and open myself up to experience life at its greatest purpose. And all of these personal findings, this *alchemy*, this *chemistry*, would have been impossible without the people that walked with me through those days...

La mia famiglia, mio papà Paolo, mia mamma Pinuccia, mia sorella Valentina, i miei nonni Rina, Angelo, Piero e Pina che, anche se lontani, non mi hanno lasciato un singolo giorno solo; persone che hanno saputo consigliarmi e incoraggiarmi in tutte le mie scelte senza mai ostacolarmi.

Begw, my lovely partner, my great love... who not only lives side by side with me, but supports and encourages me with sincere love in everything I do... and Adrien, without whom, Aberdeen and my life there would not have been the same. Without them any laughter would not have been *that* laughter; any experience would not have been *that* experience. Two gorgeous souls that I simply know that anytime I might fall they will help me back on my feet.

Donald, who has been an inspiring guide and a close friend, always present to support me with stimulating ideas and helpful discussions, in my work and in my everyday life. A great man who has been a friend before being a supervisor and showed me how beautiful and amazing Scotland is.

Tutti i miei amici di Melegnano and all my friends from Aberdeen and Cardiff: Viola, Muffo, Degio, Fabio, Mark, Rob, Helena, Denis, Nina, Ash, Magda, Jakub, Sana, Angela, Sian, Jorge, Eva, Meaghan, Adele, Rosie, Dave, Ingvild, Nesta, Daniel, Jean, Cadi, Gwil and many more... who will forever remain in my life and for that I am grateful.

A special thanks to all the members of Nanocem Consortium for the organisation and management of the MRTN-CT-2005-019283 project which this study is part of; in particular to my Industrial and Academic advisors: Dr. Tiziana De Marco, Mr. Claus Pade, Prof. Andre' Nonat and Dr. Tommy Baek Hansen. I am also grateful to Dr. C. Labbez (Universite' de Bourgogne), Prof. James A. Anderson, Dr. Richard P. K. Wells and Dr. Angela Kruth (University of Aberdeen) for their help, suggestions and interesting discussions that I had the pleasure to share with.

A special thanks also to all my friends and PhD students that in these three years have worked with me at the University of Aberdeen and within Nanocem Consortium.

November 2011,

Andrea

Acknowledgements

This study has been supported and fully funded by the European Community under the Marie Curie Research Training Network MRTN-CT-2005-019283 “Fundamental understanding of cementitious materials for improved chemical physical and aesthetic performance” (<http://www.nanocem.org/MC-RTN/>) managed by NANOCEM Network, the Industrial – Academic Research Network on Cement and Concrete. The project gathered a total of five official partners: the University of Aberdeen, UK; CTG-Italcementi Group, ITALY; Danish Technological Institute, DENMARK; the University of Surrey, UK; Aalborg Portland, DENMARK; and a joint partner: Université de Bourgogne, FRANCE. The great part of the work has been carried out at the host institution, the University of Aberdeen, which also covered the role of Project Coordinator. Four different secondments within the partners facilities allowed to complete the experimental work planned: 2 months at CTG – Italcementi for the measurements of NO_x degradation using mortars specimens; 5 months at DTI to carry out the work on TiO₂ dispersion effectiveness and relative SEM investigation; 2 weeks at Université de Bourgogne to perform ζ -potential and surface charge densities measurements and finally 2 weeks at Aalborg Portland to prepare the mortar specimens for the accelerated ageing test.

November 2011,

Andrea

Abstract

The present PhD thesis offers a general overview about fundamentals and applications of titanium dioxide (or titania), TiO_2 , photocatalysis to concrete technology in relation to enhanced aesthetic durability and depollution properties achieved by implementing TiO_2 into cement. Chemistry of degradation of Rhodamine B (RhB), a red dye used to assess self-cleaning performances of concretes containing TiO_2 , as well as oxidation of nitrogen oxides (NO_x), gaseous atmospheric pollutants responsible for acid rains and photochemical smog, is investigated using two commercial titania samples in cement and mortar specimens: a micro-sized, m- TiO_2 (average particle size $153.7 \text{ nm} \pm 48.1 \text{ nm}$) and a nano-sized, n- TiO_2 (average particle size $18.4 \text{ nm} \pm 5.0 \text{ nm}$). Experimental data on photocatalytic performances measured for the two samples are discussed in relation to photocatalyst properties and influence of the chemical environment of cement on titania particles. The study allowed to identify photo-oxidation mechanisms of RhB and NO_x on TiO_2 -containing cement and the analogies/differences with pure unsupported TiO_2 . The high pH, high ionic strength and presence of multivalent counterions, typical of cement systems, appeared to be responsible for the formation of highly attractive ion-ion correlation forces which ultimately promote enhanced TiO_2 particle agglomeration. In the case of degradation of big molecules like RhB, this enhanced agglomeration may reduce the photocatalytic activity (much lower available surface area). On the other hand smaller molecules like NO_x can easily penetrate TiO_2 agglomerates porosity and the negative effect of the enhanced agglomeration can be neglected. Engineering TiO_2 particles with specific crystallite size and tuning the photocatalyst electrokinetic properties by changing the overall pKa of the TiO_2 surface have been proven to be effective methods to control the attractive characters of the ion-ion correlation forces. Impacts on applications in construction concrete as well as suitable casting strategies to enhance the overall photocatalytic activity are also discussed.

Table of content

1. Introduction

1.1. General.....	1
1.1.1. <i>Photocatalysis for environment.....</i>	<i>1</i>
1.1.2. <i>Cement for infrastructures.....</i>	<i>2</i>
1.1.3. <i>Photocatalysis applied to cementitious materials.....</i>	<i>7</i>
1.2. Semiconductor Photocatalysis.....	11
1.2.1. <i>Theory of semiconductor materials 1: fundamentals of band formation..</i>	<i>11</i>
1.2.2. <i>Theory of semiconductor materials 2: band diagrams and excitations in semiconductors.....</i>	<i>15</i>
1.2.2.1. Thermal excitations in semiconductors: charge carriers, Fermi – Dirac distribution and Fermi levels.....	20
1.2.2.2. Optical excitations in semiconductors.....	22
1.2.2.3. Direct gap and indirect gap semiconductors.....	23
1.2.3. <i>TiO₂ colloidal semiconductors.....</i>	<i>24</i>
1.2.4. <i>Preparation of TiO₂ photocatalysts.....</i>	<i>27</i>
1.2.5. <i>Surface chemistry in TiO₂ photocatalysis.....</i>	<i>30</i>
1.2.6. <i>Thermodynamics and kinetics in TiO₂ Photocatalysis.....</i>	<i>35</i>
1.2.6.1. Thermodynamics.....	35
1.2.6.2. Kinetics.....	38
1.2.6.3. Quantum yield and photonic efficiency.....	41
1.3. The cement – TiO₂ system.....	43
1.3.1. <i>Properties and interactions.....</i>	<i>43</i>
1.3.2. <i>Self-cleaning effect.....</i>	<i>43</i>
1.3.2.1. Degradation of adsorbed organics and super-hydrophilicity.....	43
1.3.2.2. Research development and practical applications.....	45

1.3.2.3.	Problems and limitations.....	46
1.3.3.	<i>Depollution effect</i>	47
1.3.3.1.	Outdoor air pollution.....	47
1.3.3.2.	Indoor air pollution.....	49
1.3.3.3.	Research development and practical applications.....	49
1.3.3.4.	Problems and limitations.....	52
1.4.	Aims and Objectives of the Thesis	54

2. Experimental

2.1.	Materials and synthetic methods	60
2.2.	Photocatalyst characterisation	61
2.2.1.	<i>Bulk properties</i>	61
2.2.1.1.	Light absorption – U.V.-vis. Diffuse Reflectance.....	61
2.2.1.2.	Crystallinity and Polymorphism – X-Ray Diffraction.....	63
2.2.1.3.	Thermokinetics of TiO ₂ surface dehydration – Thermogravimetry, Differential Thermal Analysis and Diffuse Reflectance Infrared Fourier Transform Spectroscopy.....	65
2.2.1.4.	Particle size and morphology - Transmission Electron Microscope imaging.....	67
2.2.2.	<i>Surface properties</i>	68
2.2.2.1.	Specific Surface Area and Inter-particle porosity – N ₂ adsorption (B.E.T. and B.J.H. models).....	68
2.2.2.2.	Surface composition analysis – X-Ray Photoelectron Spectroscopy and Energy Dispersion Spectroscopy.....	71
2.2.2.3.	Electrokinetic properties – ζ -potential and surface charge density.....	73
2.2.2.4.	Dispersion effectiveness – sedimentation test.....	75
2.3.	Cement paste and mortar preparation	77
2.3.1.	<i>Cement paste preparation</i>	77
2.3.2.	<i>Mortar preparation</i>	78

2.4. Photocatalytic performance.....	80
2.4.1. <i>Self-cleaning effect – Rhodamine B (RhB) test.....</i>	<i>80</i>
2.4.2. <i>Depollution – NO_x oxidation test and modelling.....</i>	<i>81</i>
2.4.2.1. NO _x oxidation test with mortar specimens.....	81
2.4.2.2. n-TiO ₂ coated glass beads preparation.....	82
2.4.2.3. NO oxidation test with n-TiO ₂ coated glass beads.....	83
2.5. Approaching real world exposure.....	86
2.5.1. <i>Surface texture and surface microstructure design and engineering.....</i>	<i>86</i>
2.5.2. <i>Aesthetic durability – Accelerated weathering test.....</i>	<i>87</i>

3. Results and Discussion

3.1. Photocatalyst characterisation.....	91
3.1.1. <i>Bulk properties.....</i>	<i>91</i>
3.1.1.1. Light absorption – U.V.-vis. Diffuse Reflectance.....	91
3.1.1.2. Crystallinity and Polymorphism – X-Ray Diffraction.....	93
3.1.1.3. Thermokinetics of TiO ₂ surface dehydration – Thermogravimetry, Differential Thermal Analysis and Diffuse Reflectance Infrared Fourier Transform Spectroscopy.....	94
3.1.1.4. Particle size and morphology - Transmission Electron Microscope imaging.....	99
3.1.2. <i>Surface properties.....</i>	<i>100</i>
3.1.2.1. Specific Surface Area and Inter-particle porosity – N ₂ adsorption (B.E.T. and B.J.H. models).....	100
3.1.2.2. Surface composition analysis – X-Ray Photoelectron Spectroscopy and Energy Dispersion Spectroscopy.....	104
3.1.2.3. Electrokinetic properties – ζ -potential and surface charge density.....	106
3.1.2.4. Dispersion effectiveness – sedimentation test.....	109
3.1.2.4.1. m-TiO ₂ and n-TiO ₂ dispersions in the presence of Na ⁺ , Cl ⁻ or deionised water.....	109
3.1.2.4.2. m-TiO ₂ and n-TiO ₂ dispersions in the presence of K ⁺	110

3.1.2.4.3. m-TiO ₂ and n-TiO ₂ dispersions in the presence of Ca ²⁺	111
3.1.2.4.4. m-TiO ₂ and n-TiO ₂ dispersions in the presence of SO ₄ ²⁻	114
3.1.2.4.5. m-TiO ₂ and n-TiO ₂ dispersions in the presence of Na ⁺ , K ⁺ , Ca ²⁺ and SO ₄ ²⁻ , i.e. synthetic cement pore solution.....	115
3.1.3. <i>Photocatalyst characterisation summary</i>	118
3.2. Photocatalytic performance	119
3.2.1. <i>Self-cleaning effect – Rhodamine B (RhB) test</i>	119
3.2.2. <i>Depollution – NO_x oxidation test and modelling</i>	122
3.2.2.1. NO _x oxidation test with mortar specimens.....	122
3.2.2.2. Overall kinetics of photocatalytic oxidation of NO.....	124
3.2.2.3. Surface hydration, N mass balance and regimes of NO oxidation.....	127
3.2.2.4. Synergistic effect of the couple H ₂ O – O ₂	135
3.2.3. <i>Influence of particle agglomeration/dispersion on photocatalytic performance: a surface chemistry approach</i>	136
3.2.3.1. TiO ₂ dispersion in hardened cement: a particle aggregation model.....	136
3.2.3.2. Impacts on photocatalytic performances.....	137
3.3. Approaching real world exposures	141
3.3.1. <i>Surface texture and surface microstructure design and engineering</i>	141
3.3.2. <i>Aesthetic durability – Accelerated weathering test</i>	143
4. Conclusions and Future work	153

List of illustrations

1. Introduction

Figure 1.1 – Hydration of C_3S and heat evolution profile	6
Figure 1.2 – Variation of the luminosity (or brilliance) of the building facade over time	9
Figure 1.3 – Effect of photocatalytic cement TX Active on nitrogen oxides content in the air. Sidewalk and parking area in Segrate, ITALY	10
Figure 1.4 – Bonding and antibonding states for a generic homonuclear diatomic molecule $A - A$	14
Figure 1.5 – Bonding and antibonding states for a generic heteronuclear diatomic molecule $A - B$	15
Figure 1.6 – Schematic diagram of band formation as overlap of AOs in continuous arrays of MOs	16
Figure 1.7 – Bravais cell and first Brillouin zone for the body centred cubic lattice of silicon	18
Figure 1.8 – Electronic band structure of Si (bulk central bands)	20
Figure 1.9 – Electronic band structure of GaAs (bulk central bands)	21
Figure 1.10 – Temperature dependent Fermi – Dirac distribution	22
Figure 1.11 – Optical transitions in direct and indirect semiconductors	24
Figure 1.12 – TiO_2 bulk band structure diagrams and Bravais unit cells: (a) rutile; (b) anatase; (c) brookite	26
Figure 1.13 – Sulphate process operative flow chart	29
Figure 1.14 – Ball and stick models of rutile (110) and corresponding simulated STM images for: (a) vacancy-free surface, (b) bridging oxygen vacancy, (c) bridging OH group and (d) H_2O molecule on top of a 5 – coordinate Ti atom	31
Figure 1.15 – STM image of oxygen vacancies on anatase (101)	31
Figure 1.16 – TiO_2 ζ -potential (suspension in indifferent electrolytes solution)	32
Figure 1.17 – Particle agglomerate profile modelled by the Koch's fractal curve	33
Figure 1.18 – Adsorption modes of rhodamine B on charged TiO_2 surfaces	34

Figure 1.19 – TiO ₂ sensitised photoreaction	35
Figure 1.20 – Redox potentials of rutile and anatase conductance band electrons and valence band positive holes compared to redox potentials of O ₂ and H ₂ O equilibria	36
Figure 1.21 – Catalysed photoreaction	38
Figure 1.22 – Charge carriers photogeneration and recombination	39
Figure 1.23 – Reaction network for TiO ₂ -sensitised photo-oxidation of nitrogen oxides	48

2. Experimental

Figure 2.1 – Light absorption – reflection phenomena	61
Figure 2.2 – StellarNet EPP2000 Diffuse Reflectance U.V.-vis spectrometer	63
Figure 2.3 – X-ray diffraction in a crystal	64
Figure 2.4 – Bruker D8 Advance diffractometer	65
Figure 2.5 – Stanton STA 780 vertical thermo balance analyser	66
Figure 2.6 – DRIFT Spectrometer and cell	66
Figure 2.7 – JEOL Jem 2000 ex Transmission Electron Microscope	67
Figure 2.8 – Micromeritics ASAP 2020	68
Figure 2.9 – VG – Escalab X-Ray Photoelectron Spectrometer	72
Figure 2.10 – FEI Quanta 400 Scanning Electron Microscope	72
Figure 2.11 – Colloidal Dynamics 7020 Electroacoustic ZetaProbe	73
Figure 2.12 – Mixer for cement paste preparation	77
Figure 2.13 – Kenwood mixer for mortar preparation	79
Figure 2.14 – Cement specimen for self – cleaning test	80
Figure 2.15 – Lab plant flow chart for NO _x oxidation	82
Figure 2.16 – Photocatalytic reactor scheme for NO _x oxidation	82
Figure 2.17 – NO oxidation lab plant for n-TiO ₂ coated glass beads	84

Figure 2.18 – Photocatalytic continuous fixed bed reactor for n-TiO ₂ coated glass beads	85
Figure 2.19 – P 320 SiC and Zemdriain™ membrane casting	86
Figure 2.20 – Accelerated aesthetic ageing device (3AD) and relative sub-cycles	88
Figure 2.21 – CIE L*, a*, b* colour space model	89

3. Results and Discussion

Figure 3.1 – U.V.-vis Diffuse Reflectance spectrum for m-TiO ₂ (— R; --- F(R))	92
Figure 3.2 – U.V.-vis Diffuse Reflectance spectrum for n-TiO ₂ (— R; --- F(R))	92
Figure 3.3 – XRD patterns for m- and n-TiO ₂	93
Figure 3.4 – TG (a), DTG (b) and DTA (c) profiles for m-TiO ₂ and n-TiO ₂	95
Figure 3.5 – TG and DRIFT spectra for n-TiO ₂	98
Figure 3.6 – Transmission electron micrographs for m-TiO ₂ (a) and n-TiO ₂ (b)	99
Figure 3.7 – N ₂ physisorption isotherms at 77 K for m-TiO ₂ and n-TiO ₂	102
Figure 3.8 – BJH pore distribution analysis for m-TiO ₂ and n-TiO ₂	103
Figure 3.9 – m-TiO ₂ and n-TiO ₂ XPS spectra (Ti 2p and O 1s regions)	105
Figure 3.10 – m-TiO ₂ and n-TiO ₂ XPS spectra	105
Figure 3.11 – EDS results for m-TiO ₂ . P expressed as P ₂ O ₅ and K as K ₂ O	106
Figure 3.12 – m-TiO ₂ and n-TiO ₂ ζ-potentials vs pH. 1% TiO ₂ suspensions in 0.01 M NaNO ₃ solution	108
Figure 3.13 – m-TiO ₂ and n-TiO ₂ surface charge densities	108
Figure 3.14 – Sedimentation test for m-TiO ₂ and n-TiO ₂ in HCl (pH = 2), deionised water (pH = 7) and NaOH (pH = 12.5)	110
Figure 3.15 – Sedimentation test for m-TiO ₂ and n-TiO ₂ in KOH (pH = 12.5)	111
Figure 3.16 – m-TiO ₂ and n-TiO ₂ ζ-potentials vs [Ca ²⁺]	113
Figure 3.17 – Sedimentation test for m-TiO ₂ and n-TiO ₂ in Ca(OH) ₂ (pH = 12.5)	114

Figure 3.18 – Sedimentation test for m-TiO ₂ and n-TiO ₂ in H ₂ SO ₄ (pH = 2)	115
Figure 3.19 – Sedimentation test for m-TiO ₂ and n-TiO ₂ in synthetic cement pore solution (pH = 12.87)	116
Figure 3.20 – Sedimentation test for: (a) m-TiO ₂ and (b) n-TiO ₂ in synthetic cement pore solution (pH = 12.87)	116
Figure 3.21 – Flocculating/deflocculating sedimentation model. (a) m-TiO ₂ , deflocculated sediment; (b) n-TiO ₂ , flocculated sediment	117
Figure 3.22 – Diffuse reflectance spectra at various illumination time for white cement pastes without photocatalyst: (a) RhB deposition and conditioning under daylight, (b) RhB deposition and conditioning in darkness	120
Figure 3.23 – Diffuse reflectance spectra at various illumination time for white cement pastes containing m-TiO ₂ : (a) RhB deposition and conditioning under daylight, (b) RhB deposition and conditioning in darkness	120
Figure 3.24 – Diffuse reflectance spectra at various illumination time for white cement pastes containing n-TiO ₂ : (a) RhB deposition and conditioning under daylight, (b) RhB deposition and conditioning in darkness	120
Figure 3.25 – RhB-TiO ₂ system under: (a) U.V. light irradiation: <i>photo-sensitised</i> pathway; (b) visible light irradiation: <i>dye-sensitised</i> pathway	121
Figure 3.26 – NO concentration profiles at: (a) 3 l min ⁻¹ , (b) 2 l min ⁻¹ , (c) 1.5 l min ⁻¹ . (d) NO conversion versus flow rate	122
Figure 3.27 – SEM micrograph of an n-TiO ₂ coated glass bead	124
Figure 3.28 – Effect of photolysis on NO (only uncoated glass beads present)	125
Figure 3.29 – Effect of the adsorbed water on NO oxidation in the dark	125
Figure 3.30 – NO, NO ₂ and NO _x concentration profiles	128
Figure 3.31 – DRIFT spectra of n-TiO ₂ coated glass beads at 20 °C, 110 °C and 500 °C	129
Figure 3.32 – NO photoadsorption on light activated TiO ₂ (* adsorption site; /\\V\\V\\ undefined bond)	130
Figure 3.33 – Surface area loss due to NO ₃ ⁻ formation and adsorption compared to the total BET specific surface area (data referred to the TiO ₂ – coated glass beads)	134

Figure 3.34 – Effect of initial water content on total moles of NO_3^- formed on TiO_2 surface	135
Figure 3.35 – Hardened cement structures with: (a) m- TiO_2 and (b) n- TiO_2	137
Figure 3.36 – SEM surface micrographs for cement specimens (1 day cured) prepared with: (a) m- TiO_2 , (b) n- TiO_2 . SEM conditions adopted: no impregnation, no coating, low vacuum mode	139
Figure 3.37 – SEM polished cross section micrographs for cement specimens (1 day cured) prepared with: (a) m- TiO_2 , (b) n- TiO_2 . SEM conditions adopted: impregnation, no coating, low vacuum mode	139
Figure 3.38 – SEM polished cross section micrographs for cement specimens (14 days cured) prepared with: (a) m- TiO_2 , (b) n- TiO_2 . SEM conditions adopted: impregnation, C coating, high vacuum mode	140
Figure 3.39 – Cement front casting surface obtained with Zemdrain™ membrane	142
Figure 3.40 – Cement front casting surface obtained with P 320 SiC paper	142
Figure 3.41 – Cement front casting surface obtained with P 320 SiC paper, magnified detail of Figure 3.40	143
Figure 3.42 – Accelerated weathering test; L^* axis (lightness)	144
Figure 3.43 – Accelerated weathering test; a^* axis (red - green component)	145
Figure 3.44 – Accelerated weathering test; b^* axis (yellow – blue component)	146
Figure 3.45 – Accelerated weathering test; L^* axis (lightness), average values	147
Figure 3.46 – Accelerated weathering test; a^* axis (red – green component), average values	148
Figure 3.47 – Accelerated weathering test; b^* axis (yellow – blue component), average values	148

List of tables

1. Introduction

Table 1.1 – Examples of TiO ₂ – sensitized photomineralisation of organic substrates	3
Table 1.2 – Ceramic nomenclature used in cement chemistry	4
Table 1.3 – OPC composition expressed as phases present	4
Table 1.4 – OPC composition expressed as oxides	5
Table 1.5 – First, second and third Brillouin zones for simple cubic, body-centred cubic and face-centred cubic systems	19
Table 1.6 – TiO ₂ crystal structure data	27
Table 1.7 – TiO ₂ – sensitised photosynthetic and photocatalytic processes	38
Table 1.8 – Primary processes and associated characteristic time domains in the TiO ₂ -sensitized photoreactions	40

2. Experimental

Table 2.1 – Sample identification	60
Table 2.2 – Physical-chemical properties declared in manufacturer specs	60
Table 2.3 – Synthetic cement pore solution and pH	76

3. Results and Discussion

Table 3.1 – Particle size evaluation by TEM, XRD and BET	104
Table 3.2 – Data on hydration of aqueous Group IA ions and NH ₄ ⁺	112
Table 3.3 – TiO ₂ main physico – chemical properties investigated	118
Table 3.4 – Fix bed reactor fluid dynamic parameters	126

Introduction

1.1. General

1.1.1. Photocatalysis for environment

Air and water pollution is a major problem that modern societies are facing. On a daily basis, civil, industrial and military activities generate an enormous amount of organic and inorganic pollutants which inevitably end up in our atmosphere, rivers, seas and soil. Traditional water remediation techniques (on-site or off-site) involve: biological treatment (organic hazardous are used as a feedstock for bacteria), chemical treatment (contaminants are removed by reaction with added chemicals), thermal treatment (bacteria to be removed from water can be killed by high temperatures), precipitation, flocculation, filtration techniques, etc... Air pollution abatement strategies are essentially based on: electrostatic filters and membranes to reduce fine particulates, chemical and catalytic processes to purify air from hazards like SO_x, NO_x, CO, vaporised organics and formaldehyde, etc...

The work of Fujishima and Honda in the early nineteen seventies about the photocatalytic properties of titanium dioxide ¹, TiO₂, opened a new broad area of research that soon after provided valid alternatives for air and water remediation. After two decades from that milestone discovery, in the area of air, water and wastewater treatment using photocatalytic techniques, the rate of scientific publication exceeded 200 papers per year ² and in 2009 out of more than 2500 papers dealing with photocatalysis, over 800 involved air and water treatment. These figures reflect the large number of applications present nowadays on the market. Typical examples are: photocatalytic reactors for water treatment ²⁻⁵, industrial and civil air purifiers containing photocatalytic membranes ⁵, self-cleaning and antifogging glasses coated with a thin layer of photocatalyst ⁶ and construction materials (cement, concrete, paving blocks and others) containing photocatalysts in their solid structures and used for both self-cleaning and air remediation ⁷⁻¹¹.

Compared to other techniques, photocatalysis provides the great advantage to be highly environmentally friendly. To oxidise organics and inorganics indeed, the only

requirements, beyond the semiconductor photocatalyst, are water, oxygen and light with suitable energy to promote electron transitions in the band structure of the photocatalyst.

Organic compounds are generally mineralised according to Equation 1.1, generating carbon dioxide, water and potential mineral acids deriving from functional groups present in the organic structure ²:

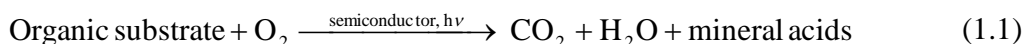


Table 1.1 ⁴ groups typical classes of organic substrates that can be degraded, even though not completely mineralised, by semiconductor photocatalysis.

Inorganics have been proved to be sensitive to light – sensitised photoreactions involving semiconductor surfaces too. Common examples are ²: compounds of transition metals involving copper, manganese, gold, chromium, iron, silver, mercury, rhodium, palladium, platinum, sulphur oxides, a large variety of nitrogen compounds like ammonia, dinitrogen, azides, nitrogen oxides, nitric acid, nitrates, nitrites, oxygen compounds like dioxygen and ozone.

1.1.2. Cement for infrastructures

Portland cement is the main binding material for concrete, one of the world most used construction material, consisting of hard and chemically inert mineral particulates (aggregate) bonded together by cement itself and water. Ordinary Portland Cement (OPC) is obtained by burning calcium carbonate (CaCO₃) found in *limestone* or *chalk* with silica (SiO₂), alumina (Al₂O₃) and iron oxide (Fe₂O₃) found in *clay* or *shale* at about 1450 °C in a rotary kiln followed by addition of a few percentages of *gypsum* (CaSO₄·2H₂O) ¹². Calcination of limestone and clay produces a solid mixture called *clinker* where the major components are: *alite* (main component tricalcium silicate, Ca₃SiO₅), *belite* (main component dicalcium silicate, Ca₂SiO₄), *aluminate* (main component tricalcium aluminate, Ca₃Al₂O₆) and *ferrite* (main component tetracalcium aluminate, Ca₄Al₂Fe₂O₁₀). According to the ceramic nomenclature these species are

usually indicated as: alite C_3S , belite C_2S , aluminate C_3A and ferrite C_4AF . Table 1.2 shows the ceramic nomenclature used in cement chemistry.

Table 1.1 - Examples of TiO_2 – sensitized photomineralisation of organic substrates.

Class	Example
Alkanes	Methane, isobutane, pentane, heptane, cyclohexane, paraffin
Haloalkanes	Mono-, di-, tri- and tetrachloromethane, tribromoethane, 1,1,1-trifluoro-2,2,2-trichloroethane
Aliphatic alcohols	Methanol, ethanol, isopropyl alcohol, glucose, sucrose
Aliphatic carboxylic acids	Formic, ethanoic, dimethylethanoic, propanoic, oxalic acids
Alkenes	Propene, cyclohexene
Haloalkenes	Perchloroethene, 1,2-dichloroethene, 1,1,2-trichloroethene
Aromatics	Benzene, naphthalene
Haloaromatics	Chlorobenzene, 1,2-dichlorobenzene, bromobenzene
Nitrohaloaromatics	3,4-Dichloronitrobenzene, dichloronitrobenzene
Phenols	Phenol, hydroquinone, catechol, 4-methylcatechol, resorcinol, o-, m-, p-cresol
Halophenols	2-, 3-, 4-Chlorophenol, pentachlorophenol, 4-fluorophenol, 3,4-difluorophenol
Aromatic carboxylic acids	Benzoic, 4-aminobenzoic, phthalic, salicylic, m- and p-hydroxybenzoic, chlorohydroxybenzoic acids
Polymers	Polyethylene, poly (vinyl chloride) (PVC)
Surfactants	Sodium dodecylsulphate (SDS), polyethylene glycol, sodium dodecyl benzene sulphonate, trimethyl phosphate, tetrabutylammonium phosphate
Herbicides	Methyl viologen, atrazine, simazine, prometon, propetryne, bentazon
Pesticides	DDT, parathion, lindane
Dyes	Methylene blue, rhodamine B, methyl orange, fluorescein

Table 1.2 – Ceramic nomenclature used in cement chemistry.

Symbol	Oxide
C	CaO
S	SiO ₂
A	Al ₂ O ₃
F	Fe ₂ O ₃
H	H ₂ O
\bar{S} , Š or \$	SO ₃
\bar{C} or Č	CO ₂

Typical OPC compositions limits are shown in Table 1.3 and in Table 1.4 in terms of both phases and formal oxides ^{12, 13}.

Table 1.3 – OPC composition expressed as phases present.

Phase	%	Major component	Minor Component
Alite	50 – 70	C ₃ S	Al ₂ O ₃ , MgO, P ₂ O ₅ , Fe ₂ O ₃ , Na ₂ O, K ₂ O
Belite	15 – 30	C ₂ S	Al ₂ O ₃ , MgO, P ₂ O ₅ , Fe ₂ O ₃ , Na ₂ O, K ₂ O
Aluminate	5 – 10	C ₃ A	MgO, Fe ₂ O ₃ , Na ₂ O, K ₂ O, SiO ₂
Ferrite	5 – 15	C ₄ AF	MgO, SiO ₂ , TiO ₂ , Mn ₂ O ₃
Gypsum	2 – 4	C\$·2H	

Cement hydration refers to the chemical combination of cement and water. When water is added to anhydrous cement the overall process can be described as follow ¹²:

- Dissolution (partial or complete) of cement grains;
- Formation of different compounds (see below) in solution accompanied with an increase of its ionic strength;

- iii. Precipitation of the hydration products once their saturation concentration in solution is reached;
- iv. In later stages, products form on or very near the surface of anhydrous cement grains;

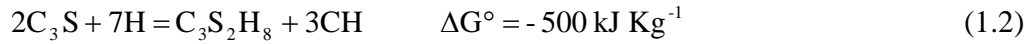
Table 1.4 – OPC composition expressed as oxides.

Oxide	%
CaO	60 – 67
SiO ₂	17 – 25
Al ₂ O ₃	3 – 8
Fe ₂ O ₃	0.5 – 6
MgO	0.1 – 4
Na ₂ O + K ₂ O	0.2 – 1.3
SO ₃	1 – 4

Hydration of Portland cement is a highly exothermic process. Although the actual mechanism of hydration is not yet fully understood, its kinetics is very well known.

Each phase has a specific reaction with water to produce a range of hydration products. Between all, **CH** (Ca(OH)₂, mineral name Portlandite) and **CSH** (xCaO·SiO₂·yH₂O, generic term for calcium silicate hydrate) play an important role in defining the pH and chemical behaviour of the material. CSH is a poorly crystalline product of variable composition in terms of its H₂O/SiO₂ ratio and Ca/Si ratio with a very high specific surface area. It forms a gel that is nearly X- ray amorphous and is responsible for the development of strength in Portland cement. In Portland cement Ca/Si ratio is usually ~ 1.1 - 2.0. However it is believed that the range of single phase homogenous gel extends to much lower Ca/Si ratios, in the range to about 0.8.

Hydration of C₃S occurs according to the reaction in Equation 1.2 ¹²:



whilst Figure 1.1 shows the heat evolution associated to the same reaction. Before the steady state is reached, the hydration process is characterised by four distinct periods ¹²:

- Preinduction period*; Ca^{2+} and OH^- ions are released from the C_3S grain surface due to direct contact with water, the pH rises over 12 and a very rapid heat evolution occurs. This initial stage is very short and usually over within 15 minutes.
- Induction or dormant period*; Ca^{2+} concentration approaches saturation levels and consequently the hydrolysis of C_3S slows down (drop of the heat evolution profile). The plastic behaviour of cement is developed in this stage of hydration. The induction period usually lasts for 2 – 4 hours.
- Acceleration period*; Ca^{2+} saturation activity reached during the induction period leads to crystallisation of CH from solution and precipitation of the CSH at the C_3S grain boundaries in the form of a coating. The drop of Ca^{2+} activity in solution is the driving force for further C_3S to hydrolyse (heat evolution increases again). The maximum rate of heat evolution is reached in between 4 and 8 hours.
- Deceleration period*; during this stage the reaction slows down again reaching a steady state within 12 to 24 hours.

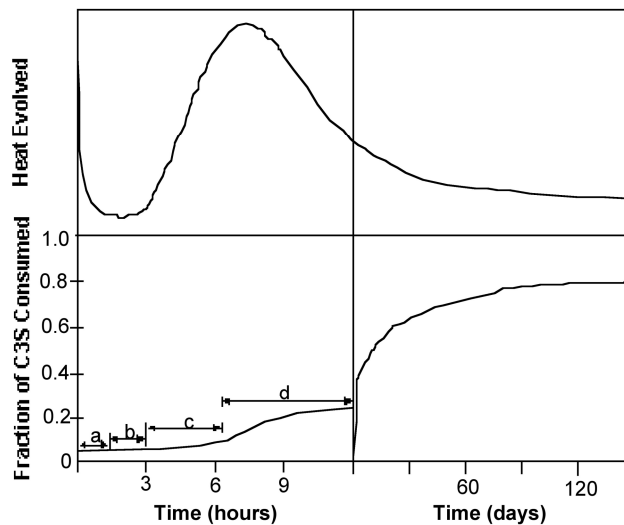
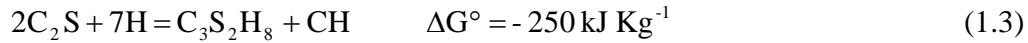


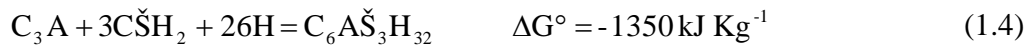
Figure 1.1 – Hydration of C_3S and heat evolution profile ¹⁴.

Once the steady state is achieved, C₃S hydration goes through a slow diffusion controlled regime. Indeed water needs to diffuse through the CSH coating around C₃S grain to reach the unreacted core and promote further hydrolysis¹². The grain hydration is usually never completed and unreacted grains are found in hardened cement even after years.

C₂S hydrolyses similar to C₃S with the difference that the overall reaction is much slower and the related heat evolved much lower (Equation 1.3)¹²:



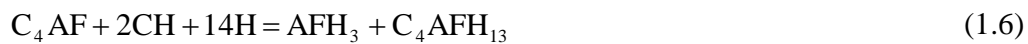
C₃A hydrolyses very quickly and the reaction unleashes much heat (*flash set*)¹². Addition of few percentages of gypsum after clinker production aims therefore to control C₃A hydration and delay initial set through *ettringite*, C₆AŠ₃H₃₂, formation:



If gypsum is totally consumed but further unreacted C₃A is still available, the remaining C₃A reacts with ettringite forming *monosulfoaluminate*, C₄AŠH₁₂:



Finally, hydration of C₄AF is similar to C₃A but characterised by much less reactivity for C₄AF and much less gypsum consumption in the reaction¹². Reaction with CH and water forms an amorphous ferric aluminum hydroxide and a compound similar to monosulfoaluminate where Š is replaced with F:



The reaction rate of the different phases follows the series: C₃A > C₃S > C₄AF > C₂S¹².

1.1.3. Photocatalysis applied to cementitious materials

Application of photocatalysis to construction materials began towards the end of the 1980s. Two important effects related to the nature of photoactive TiO₂ coatings had by this time been discovered:

- i. the self-cleaning effect due to redox reactions promoted by sunlight (or in general, weak U.V. light) on the photocatalyst surface ¹⁵;
- ii. the photo-induced hydrophilicity ^{16, 17} of the catalyst surface, which enhances the self-cleaning effect (inorganics causing dirt and stains on surfaces can be easily removed due to rainwater soaking between the adsorbed substance and the TiO₂ surface).

Photocatalytic glasses provide an example of self-cleaning and anti-fogging (wetting) properties, e.g. Pilkington Active™ ^{6, 18}. Recently, photocatalytic cementitious materials have been patented by Mitsubishi Corp.(NOxer™), and Italcementi SpA (TX-Aria™ and TX-Arca™) ^{9-11, 19}. In all these construction materials the active photocatalyst is anatase TiO₂ (the most active between the three TiO₂ polymorphs: anatase, rutile and brookite). The main reasons why TiO₂ is, so far, the most used photocatalyst for such applications are:

- i. Its brilliant white colour, hence very suitable for white cement concrete;
- ii. TiO₂ is very cheap compared to other semiconductor photocatalysts;
- iii. TiO₂ is extremely stable; it does not undergo photoanodic corrosion (like other semiconductors used in photocatalysis, e.g.: CdS ⁴) and does not react with cementitious phases.

Although the use of *photocatalytic cement* (common designation for the solid mixture cement – photocatalyst) is still restricted and limited compared to ordinary cement, many buildings and city roads have been designed and constructed since 2000 using concrete and paving blocks containing TiO₂. Relevant examples are: Church “Dives in Misericordia”, Rome, ITALY; Music and Arts City Hall, Chambéry, FRANCE; Police Central Station, Bordeaux, FRANCE; Air France Building, Roissy – Charles de Gaulle Airport, FRANCE; Saint John’s Court, Montacarlo, MONACO; several city side walks and roads in Italy and a parking area in Antwerp, BELGIUM ⁷.

The application of TiO₂ photocatalysis to concrete aims to achieve two main goals, the self-cleaning effect discussed above (in particular for structure based on white cement concrete) and the *depolluting* effect due to the oxidation of nitrogen oxides (NO_x) in the

atmosphere to NO_3^- , especially in street canyons (deep, narrow, valley-like space above a street in a city, created by tall buildings on both sides) where NO_x concentrations can be considerable due to combustion engine exhausts. Scientific tests carried out on these structures highlighted the high level of aesthetic durability achieved and the impact on air pollutants when TiO_2 is present. Figure 1.2 shows the Music and Arts City Hall in Chambéry, FRANCE, where the different sampling points are indicated. After 30 months the level of brilliance of the façade is well maintained and no significant variation compared to the initial values are observed.

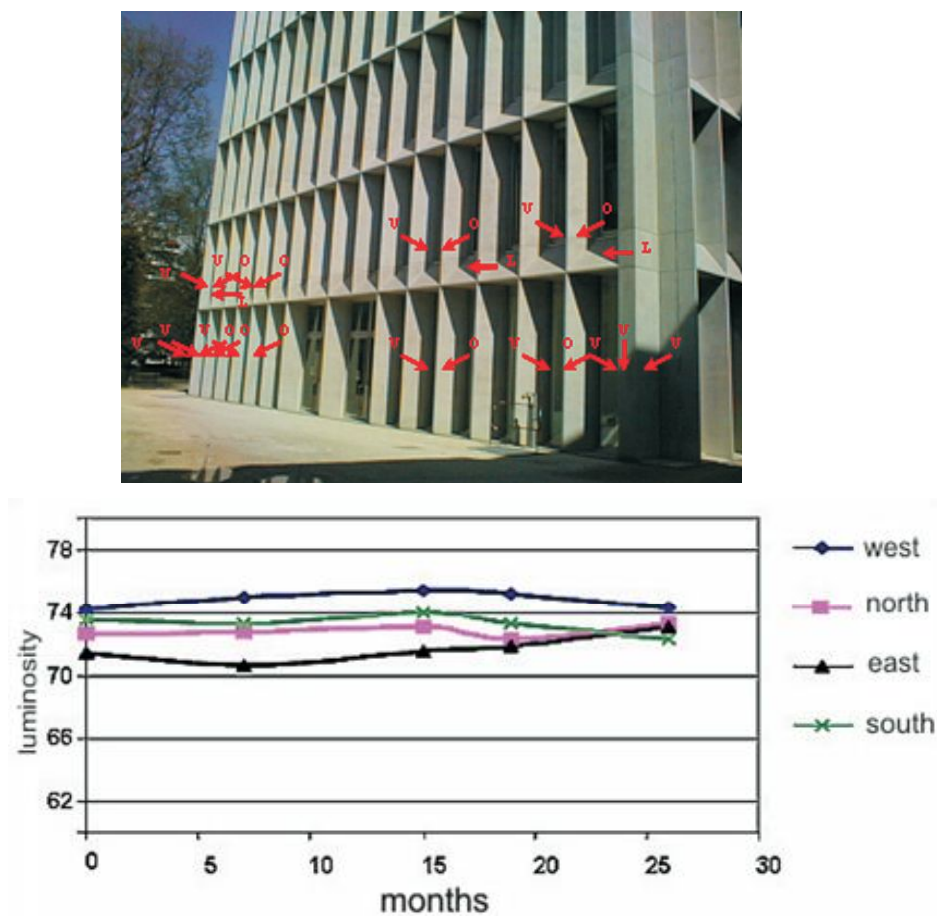


Figure 1.2 – Variation of the luminosity (or brilliance) of the building facade over time.

The absence of significant drops in the brilliance trends is taken as an indication of the self-cleaning effect promoted by TiO_2 in the cementitious structure.

Figure 1.3 shows the average level of nitrogen oxides over a period of nine months in proximity of a sidewalk/parking area rebuilt using Italcementi's photocatalytic cement TX Active Aria™ compared to a similar area made out of ordinary asphalt⁷.

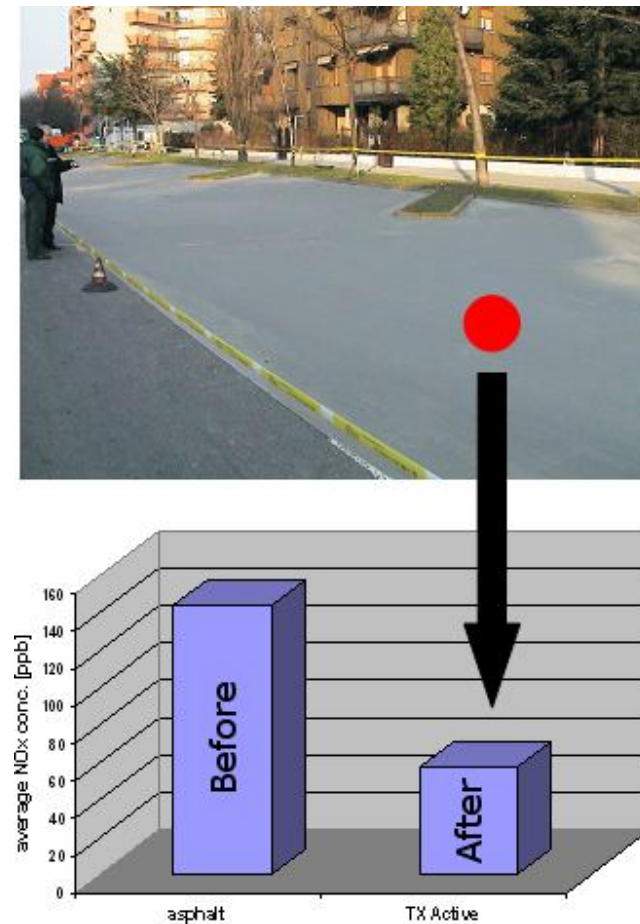


Figure 1.3 – Effect of photocatalytic cement TX Active on nitrogen oxides content in the air around the sidewalk and parking area in Segrate, ITALY (picture above the graph)⁷.

The graph shows the average content of NOx before the renovation of the area with TX Active cement and after. Both the values, before and after, are the average estimations of 9 months of constant monitoring.

1.2. Semiconductor photocatalysis

1.2.1. Theory of semiconductor materials 1: fundamentals of band formation

The electronic structure of a crystal lattice can be derived through two different theoretical approaches. The first one, mainly used by physicists, implies the development of electronic wavefunctions which satisfy the periodic properties of the crystal followed by a suitable modification in order to fulfil the characteristics of the interatomic bonding. The second approach, widely used in chemistry, implies a molecular orbital description for the intermolecular bonding in the unit cell as a starting point. Subsequently symmetry conditions are sought to extend the wavefunctions to the entire crystal. This approach is used here to describe the electronic properties of semiconductor materials²⁰.

Energy and wavefunctions for two hydrogenic 1s orbitals in an isolated A₁-A₂ homonuclear diatomic molecule represent the simplest case which can be extended to more complex crystalline structures and with different types of orbitals (p, d, etc..). At an infinite distance the two atoms have an equal energy identified as E_g, ground state energy, and their Schrödinger equations (as eigenfunction equations):

$$H_1|1\rangle = E_g|1\rangle \quad (1.7)$$

$$H_2|2\rangle = E_g|2\rangle \quad (1.8)$$

can be solved analytically to obtain the radial 1s wavefunctions ψ_1 and ψ_2 , here simply indicated with $|1\rangle$ and $|2\rangle$ respectively, relative to the eigenvalue E_g²⁰⁻²². The parameter H₁ and H₂ are the Hamiltonian operators for the two atoms:

$$H = -\frac{\hbar}{2m}\nabla^2 + V \quad (1.9)$$

$-\frac{\hbar}{2m}\nabla^2$ accounts for the kinetic energy while V the potential one²⁰⁻²².

At the bond distance (formation of molecule), the Schrödinger equation is no longer analytically soluble (two electrons system) and an approximate solution has to be found. The most accepted method is the linear combination of atomic orbital, often referred to as LCAO. The ground state for the molecule A_1-A_2 , Ψ , solution of the new Schrödinger equation:

$$H|\Psi\rangle = E|\Psi\rangle \quad (1.10)$$

is obtained as:

$$|\Psi\rangle = c_1|1\rangle + c_2|2\rangle \quad (1.11)$$

where c_1 and c_2 are combinatorial constants to be calculated ²⁰⁻²². $|1\rangle$ and $|2\rangle$ are assumed to be orthonormal so that ²⁰⁻²²:

$$\langle 1|2\rangle = \langle 2|1\rangle = \int \psi_1^* \psi_2 = \int \psi_2^* \psi_1 = 0 \quad (1.12)$$

and

$$\langle 1|1\rangle = \langle 2|2\rangle = \int \psi_1^* \psi_1 = \int \psi_2^* \psi_2 = 1 \quad (1.13)$$

This orthonormality is a pure mathematical artefacts which in reality cannot be true when the 1s orbitals get closer and start overlapping each other. It is generally known as *Hückel approximation* and introduced to simplify the problem, indeed the generic qualitative features of the molecular bond survive this assumption ²⁰⁻²². A more general and precise solution can be derived without the Hückel approximation. $\langle 1|2\rangle = \langle 2|1\rangle$ are also known as *overlap integrals* ²⁰⁻²².

Replacing Ψ in the molecular orbital (MO) Schrödinger equation according to Equation 1.11 and multiplying both members for the atomic 1s ground states $|1\rangle$ and $|2\rangle$ alternatively, a set of two linearly independent equations is obtained ²⁰:

$$\langle 1|H(c_1|1\rangle + c_2|2\rangle) = \langle 1|E(c_1|1\rangle + c_2|2\rangle) \quad (1.14)$$

$$\langle 2|H(c_1|1\rangle + c_2|2\rangle) = \langle 2|E(c_1|1\rangle + c_2|2\rangle) \quad (1.15)$$

The matrix product between atomic ground states and the Hamiltonians at the first member of each equation generates 2x2 Hamiltonian matrixes indicated as H_{ij} as follow²⁰:

$$c_1 H_{11} + c_2 H_{12} = \langle 1 | E (c_1 | 1 \rangle + c_2 | 2 \rangle) \quad (1.16)$$

$$c_1 H_{21} + c_2 H_{22} = \langle 2 | E (c_1 | 1 \rangle + c_2 | 2 \rangle) \quad (1.17)$$

Applying now the Hückel approximation, the equations are reduced to:

$$c_1 H_{11} + c_2 H_{12} = c_1 E \quad (1.18)$$

$$c_1 H_{21} + c_2 H_{22} = c_2 E \quad (1.19)$$

The H_{11} and H_{22} Hamiltonians (“on-site Hamiltonians”) represent the energy related to electrostatic interaction between the two atoms. This is E_0 with an additional contribution due to the presence of the second atom at a distance $\neq \infty$ and usually indicated as E_0^{20-22} . The H_{12} and H_{21} Hamiltonians represent the energy released once the bond is formed, so, if the electrostatic repulsive energy is assumed positive, this term is negative. Hamiltonians are hermitian matrixes which implies $H_{12} = H_{21}^*$. Nevertheless, 1s orbitals are real and not complex (spherical symmetry), so $H_{12} = H_{21}$. This energetic contribution is usually indicated as β^{20-22} . Rewriting now the system of equations in matrix form where c_1 and c_2 are the unknowns:

$$\begin{vmatrix} (E_0 - E) & \beta \\ \beta & (E_0 - E) \end{vmatrix} \quad (1.20)$$

Equations 1.20 in their matrix form are known as *secular equations* and, to obtain not trivial solutions for the coefficients c_1 and c_2 , the matrix has to be singular (determinant equal to zero)²⁰⁻²². This lead to the following Equation 1.21:

$$E_0^2 - 2E_0E + E^2 - 2\beta^2 = 0 \quad (1.21)$$

Having as solutions (for E):

$$E_a = E_0 + \beta \quad (1.22)$$

and

$$E_b = E_0 - \beta \quad (1.23)$$

The normalised MO wavefunctions corresponding to the eigenvalues E_a and E_b are respectively:

$$|\Psi_a\rangle = \frac{1}{\sqrt{2}}(|1\rangle + |2\rangle) \quad (1.24)$$

$$|\Psi_b\rangle = \frac{1}{\sqrt{2}}(|1\rangle - |2\rangle) \quad (1.25)$$

with an energy gap equal to 2β ²⁰⁻²². The two new molecular orbitals are called σ (bonding, lower energy) and σ^* (antibonding, higher energy) with analogy to the starting s atomic orbitals (p atomic orbitals become π molecular orbital and so on). The bonding and antibonding states for the homonuclear diatomic molecule are shown in Figure 1.4.

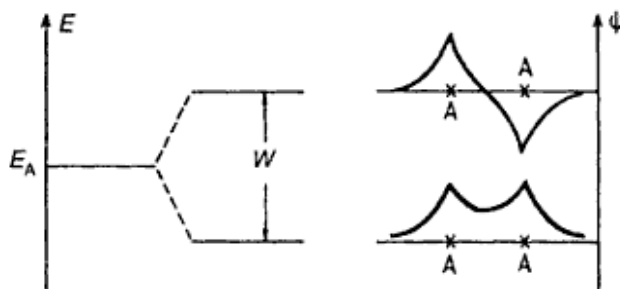


Figure 1.4 – Bonding and antibonding states for a generic homonuclear diatomic molecule $A - A$ ²⁰.

The MO bonding state carries the same sign all over the space where it is confined whilst the MO antibonding state has a node centred in between the two nuclei. For heteronuclear diatomic molecules, the bonding wavefunction has always one sign but different electron densities around the nuclei and the node in the antibonding state is shifted according to this different electron density, see Figure 1.5.

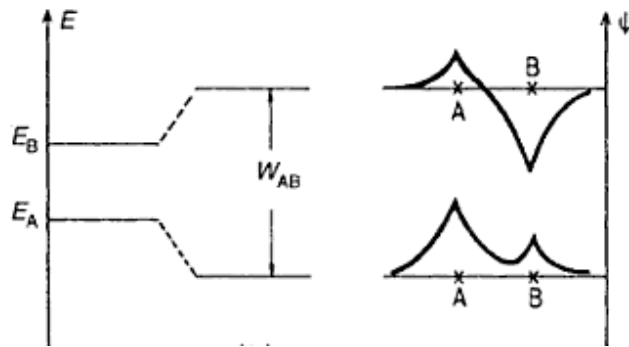


Figure 1.5 – Bonding and antibonding states for a generic heteronuclear diatomic molecule A – B ²⁰.

The extension of the LCAO to the case of n atoms forming a crystal lattice and overlapping each other in the formation of the chemical bonds, leads to the presence of n MOs. The energy gap between two adjacent molecular states becomes smaller and smaller with the increase of the number of overlapped atoms until forming a *continuous* of energy states for n very high. This continuous of energy state is usually referred to as *band* ²⁰⁻²². Solving the Schrödinger equation considering that an atom in the crystal lattice interacts only with its immediate surroundings leads to energy gap between the most stable MO and the most unstable MO in the band equals to 4β ²⁰⁻²². It has been proved that β is the same as in the diatomic example; therefore it can be seen as the interatomic potential of nearest neighbours in the lattice. The limit value of 4β for $n \rightarrow \infty$ is known as *bandwidth* ²⁰⁻²². The situation for an n atoms crystal lattice is pictured in Figure 1.6, showing the band formation.

1.2.2. Theory of semiconductor materials 2: band diagrams and excitations in semiconductors

In the previous section the band formation by n atomic orbitals overlapping has been described. The following step is to study the features of the band structure of a crystal lattice.

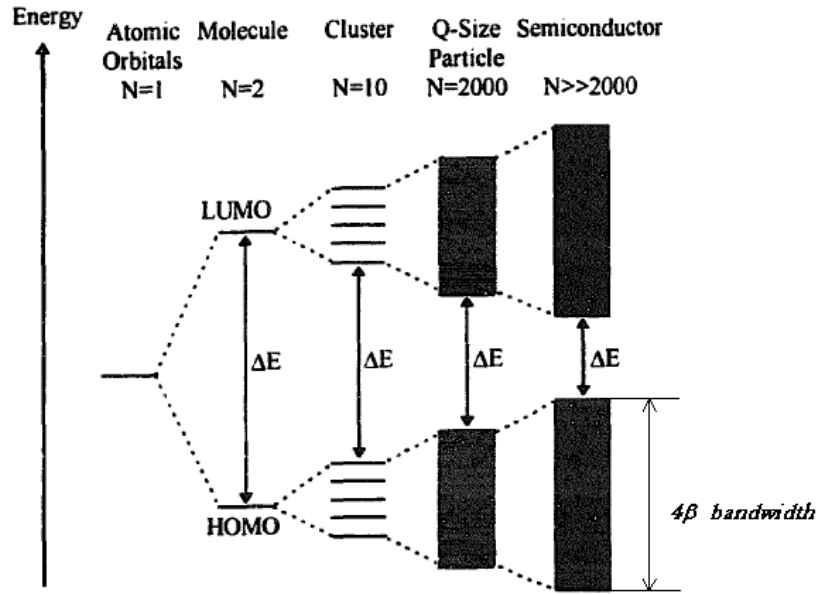


Figure 1.6 – Schematic diagram of band formation as overlap of AOs in continuous arrays of MOs ⁴.

A crystal is a solid structure constituted by a periodical repetition of an elementary basis. Mathematically it can be described as follows, with A_1 being a single element of the crystal lattice (analogously to the A_1 - A_2 diatomic molecule in the previous paragraph) in equilibrium and with coordinates $\mathbf{r} = x\mathbf{u}_x + y\mathbf{u}_y + z\mathbf{u}_z$ in a given reference system. All the elements in the crystal lattice showing the same chemical and physical environment as the element A_1 can be expressed as ²⁰⁻²²:

$$\mathbf{r}' = \mathbf{r} + m_1\mathbf{a}_1 + m_2\mathbf{a}_2 + m_3\mathbf{a}_3 \quad (1.26)$$

m_1 , m_2 and m_3 are integer values whilst vectors \mathbf{a}_1 , \mathbf{a}_2 and \mathbf{a}_3 are the so called *non-coplanar* vectors and specific for the given crystal. They are generators of the crystal unit cell and periods of the *Bravais* lattice ²⁰⁻²².

According to LCAO method a molecular orbital is a combination of atomic orbitals (section 1.2.1), which, for an infinite number of atoms in a structure, means an infinite repeating combination of atomic orbitals. In a periodical crystal lattice as defined in Equation 1.26, this infinite number of AOs combining with each other to generate MOs can be expressed taking into account a single atomic orbital and specifying its periodicity. For example, if in the crystal lattice n 1s orbitals combine to generate n σ MOs, the same

combination can be achieved, instead of considering n 1s orbitals, by considering a single 1s orbital and its periodicity expressed by the function ²⁰⁻²²:

$$|\mathbf{k}\rangle = |1\rangle e^{i\mathbf{k}\mathbf{r}} = |1\rangle (\cos \mathbf{k}\mathbf{r} + i \sin \mathbf{k}\mathbf{r}) \quad (1.27)$$

where, according to the matrix notation used in section 1.2.1, $|\mathbf{k}\rangle = \psi_{\mathbf{k}}(\mathbf{r})$ and $|1\rangle = \psi_1(\mathbf{r})$. A more general expression (Equation 1.27 is indeed referred to 1s orbitals only) is:

$$|\mathbf{k}\rangle = |n,1\rangle e^{i\mathbf{k}\mathbf{r}} \quad (1.28)$$

where n is a quantum number (defined further on). The functions 1.28 form a complete orthonormal basis, indeed ²⁰⁻²²:

$$\langle n, \mathbf{k} | n', \mathbf{k}' \rangle = \delta_{n,n'} \delta_{\mathbf{k},\mathbf{k}'} \quad (1.29)$$

$$\sum_{n\mathbf{k}} |n\mathbf{k}\rangle \langle n\mathbf{k}| = 1 \quad (1.30)$$

Wavefunctions like Equation 1.28 are solutions of the Schrödinger equations for the atoms in the crystal when the potential $V(\mathbf{r})$ in the Hamiltonian has the periodicity of the lattice and known as *Bloch functions* ²⁰⁻²². The quantum number $\mathbf{k} = k_x \mathbf{u}_x + k_y \mathbf{u}_y + k_z \mathbf{u}_z$ is a vector defining a translated space usually referred to as *\mathbf{k} -space* or *reciprocal lattice space* ²⁰⁻²². The crystal unit cell in the reciprocal space (obviously translated compared to the original Bravais unit cell) is called a *Brillouin zone* (or *first Brillouin zone* or *central Brillouin zone*) ²⁰⁻²². The Brillouin zone is defined as a region in the \mathbf{k} -space where the Bloch functions are completely characterised. It represents the analogy of the Bravais unit cell in the domain of the Bloch functions or, more precisely, it is defined to be the Wigner-Seitz primitive cell of the reciprocal lattice. In other words, from a geometrical and symmetrical perspective a crystal can be considered as infinite repetition of its single Bravais unit cell. From a wavefunction (Bloch functions) perspective a crystal can be considered as infinite repetition of its single Brillouin zone (or Wigner-Seitz primitive cell of the reciprocal lattice). Figure 1.7

shows the Bravais cell and the first Brillouin zone for the body-centred cubic lattice of silicon.

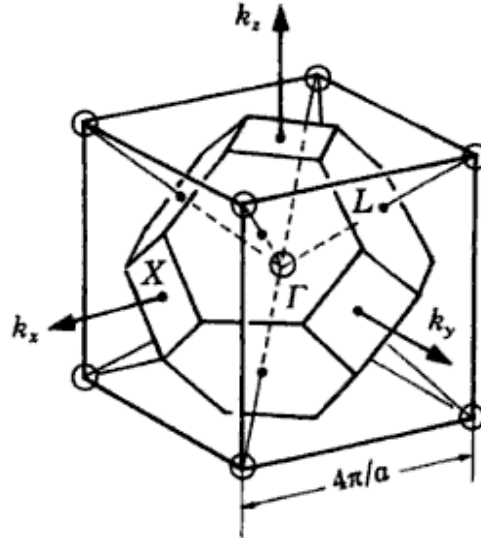


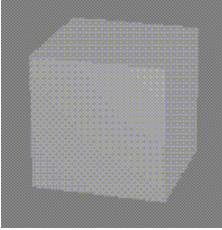
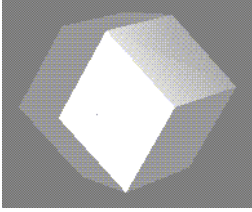
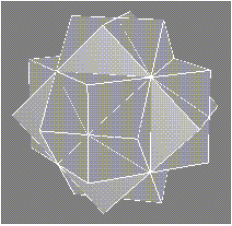
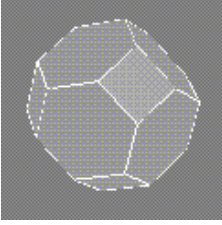
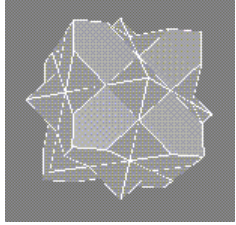
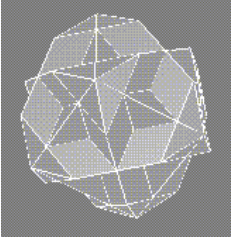
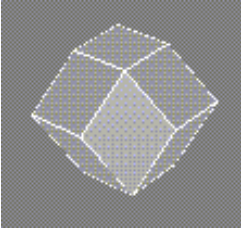
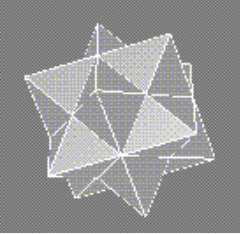
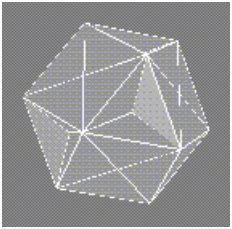
Figure 1.7 – Bravais cell and first Brillouin zone for the body-centred cubic lattice of silicon.

Second, third and higher orders Brillouin zones also exist. In the reciprocal lattice space the first Brillouin zone is the set of points reachable from the origin, $\mathbf{k} = 0$ (symmetry point Γ), without crossing any Bragg plane. The second one is the set of points reachable crossing just one Bragg plane and so on. In general, the n Brillouin zone is the set points reachable from the origin and crossing $(n-1)$ Bragg planes. Table 1.5 shows the first, second and third Brillouin zones for simple cubic, body-centred cubic and face-centred cubic systems.

The Schrödinger equation exhibits a discrete set of solutions for each single value of \mathbf{k} in the Brillouin zone, so, solving it over the entire domain of \mathbf{k} (i.e. the entire Brillouin zone), permitted energy bands, forbidden energy bands and relative band gaps are globally defined. The quantum number n of the Bloch functions represents the *band index* and it unambiguously defines a single band²⁰⁻²². Thus, for a given n (i.e. a given band) the eigenvalue $E_{n,k}$ (energy of the band) can be plotted versus k and an overall diagram showing the energy of all the bands in the crystal obtained. Figures 1.8 and 1.9 show the bulk central bands of the Si crystal (Bravais bcc; Brillouin fcc) and GaAs crystal (Bravais

bcc; Brillouin fcc) in the k domain with the main symmetry points L , Γ (centre of the Brillouin zone) and X highlighted (calculations performed using the Java routine *Bandstructure Lab* ²³).

Table 1.5 – First, second and third Brillouin zones for simple cubic, body-centred cubic and face-centred cubic systems.

Bravais lattice	Reciprocal lattice	1 st Brillouin zone	2 nd Brillouin zone	3 rd Brillouin zone
sc	sc			
bcc	fcc			
fcc	bcc			

$E - \mathbf{k}$ diagrams show the *permitted* energy bands of the solid crystal structure. At $T = 0$ K, the highest energy permitted band *filled* with electrons is conventionally called *valence bands* ²⁰⁻²². The permitted *empty* band found at positive energies immediately above the valence band is conventionally called *conduction* or *conductance* band ²⁰⁻²². Clearly, like the case of atomic and molecular orbitals, when referring to band *filled* with electrons, we do not intend that electrons physically *occupy* the band. We denote a Bloch's wavefunction (i.e. the band) which describes the state of electrons with that

particular energy. The valence band *contains* the electrons that form the bond (usually covalent) between the atoms in the crystal. The bands lying below the valence band *contains* the inner electrons that do not participate in the bonds in the crystals. They are usually referred to as *sub-valence bands* (VB3, VB4, VB5, VB6 in Figures 1.8 and 1.9). Similarly, all the bands lying at energies higher than the conductance band can be referred to as *sub-conductance bands*.

The energy gap between valence and conductance band is known as *band gap* and it is a characteristic of the crystal lattice. Generally in solid state physics, the band gap is the parameter used to classify solid crystals in *semiconductors*, *conductors* or *insulators*²⁰⁻²². Conventionally if the band gap is < 0 , i.e. valence band and conductance band overlap, or $<< 1\text{ eV}$, the crystal is a conductor; if the band gap is $>> 3\text{ eV}$, the crystal is considered as an insulator, crystals with band gap lying between these two limit values are referred to as semiconductors.

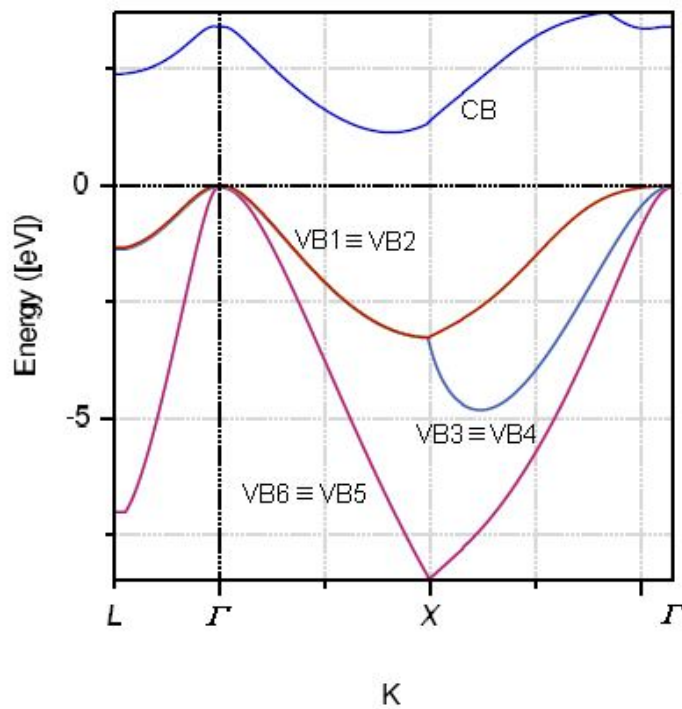


Figure 1.8 – Electronic band structure of Si (bulk central bands).

1.2.2.1. Thermal excitations in semiconductors: charge carriers, Fermi – Dirac distribution and Fermi levels

In *intrinsic* semiconductors (no impurities in the crystal lattice) at temperature higher than 0 K, some electrons in the valence band *may* have enough thermal energy to overcome the energy gap between valence and conductance band and *jump* into the latter²⁰⁻²². This phenomenon leads to the formation of new electron states. A vacant electron state in the valence band is commonly known as *hole*, while the new generated electron state in the conductance band known as *free electron* (electric and thermal conductivities of crystal lattices depend on the mobility of the free electrons in the conductance band)²⁰⁻²². Holes and free electrons are usually denoted as *charge carriers*.

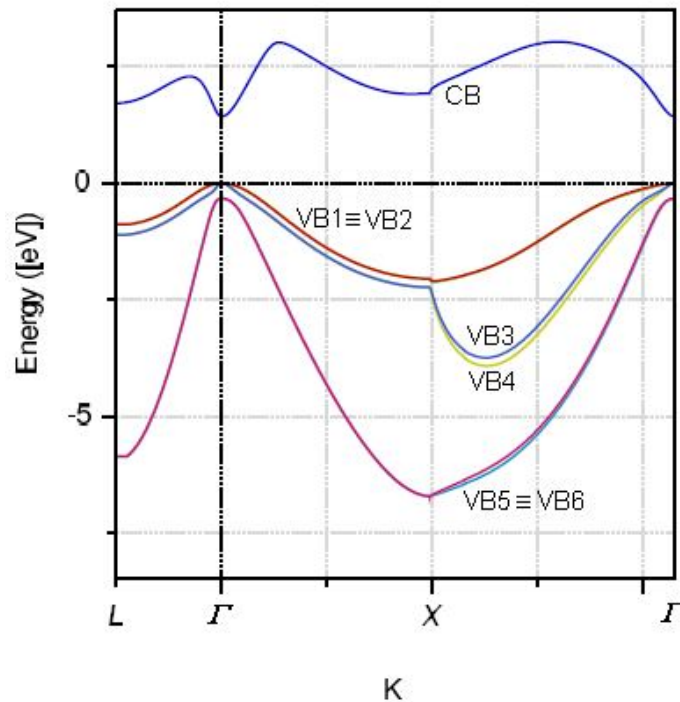


Figure 1.9 – Electronic band structure of GaAs (bulk central bands).

The mobile free electrons in the conductance band can easily recombine with the positive holes during their random motion. The thermal generation of the electron – hole pairs and the subsequent recombination is a continuous dynamic process that, at $T > 0$ K, is temperature dependent²⁰⁻²². Electrons are *fermions* (particle with half integer spin), therefore at a given temperature T , the Fermi – Dirac distribution can be used to describe

the electronic population between valence and conductance bands, Figure 1.10. The probability of occupying an energy state E , is described by the function in Equation 1.31:

$$f_n(E) = \frac{1}{\exp[(E - E_F)/k_B T] + 1} \quad (1.31)$$

where k_B is the Boltzmann constant, T the temperature and E_F , referred to as the Fermi level, the energy level at which the probability of finding an electron is 0.5. At a given temperature T and for equal effective masses for free electrons and holes $m_e^* = m_h^*$, the Fermi level lies exactly in the middle between the valence band and the conductance band²⁰⁻²².

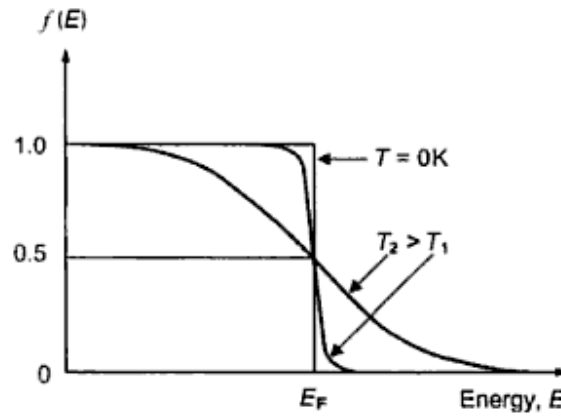


Figure 1.10 – Temperature dependent Fermi – Dirac distribution.

1.2.2.2. Optical excitations in semiconductors

In the previous section we analysed the thermal equilibrium between free electrons and positive holes in semiconductor bands at a temperature > 0 K. However thermal transitions are not the only possible excitation mechanism that semiconductors undergo. Incident photons (light) with energy equal (or higher) than the semiconductor band gap, can promote transitions of electrons from the valence band to the conductance band²⁰⁻²². This process is often referred to as *optical absorption* to distinguish it from the thermal absorption outlined previously. Direct interband absorption of a photon $h\nu$ occurs at all point in the Brillouin zone for which energy is conserved (Equation 1.32)²²:

$$h\nu = \varepsilon_c(\mathbf{k}) - \varepsilon_v(\mathbf{k}) \quad (1.32)$$

where h is the Plank constant, ν the frequency of the incident light, $\varepsilon_c(\mathbf{k})$ the energy of the conductance band and $\varepsilon_v(\mathbf{k})$ the energy of the valence band.

Optical absorption phenomena are mathematically described through an *absorption coefficient* α determined by optical spectroscopy through the Equation 1.33²¹:

$$\frac{I}{I_0} = \frac{(1 - R)^2 \exp(-\alpha d)}{1 - R^2 \exp(-2\alpha d)} \quad (1.33)$$

where I_0 is the intensity of the incident light, I the intensity of the transmitted light, R the reflectivity and d the thickness of the material.

Optical absorption phenomena in semiconductors are the fundamental initial step in all photocatalytic processes since the activation of the photocatalyst occurs exactly through promotion of electrons from the valence band to the conductance band by photon absorption.

1.2.2.3. Direct gap and indirect gap semiconductors

The symmetry of the band structure of a crystal lattice defines whether or not optical absorption phenomena occurring in a semiconductor material are *direct* or *indirect*. Consequently to the absorption of a photon and relative electron transition from the valence band to the conductance band, both energy and electron momentum $\hbar\mathbf{k}$ must be conserved. Energy conservation has been already discussed in Equation 1.32 whilst momentum conservation depends on the symmetry of the band structure²⁰⁻²². For semiconductor like GaAs (Figure 1.9), the maximum of the valence band and the minimum of the conductance band occur at the same value of the wavevector \mathbf{k} , therefore $\Delta\mathbf{k} = 0$ and the momentum is conserved. Electron transitions are direct and the semiconductor indicated as *direct gap* semiconductor²⁰⁻²². When the maximum of the valence band and the minimum of the conductance band lay at different values of the wavevector \mathbf{k} like in the case of Si (Figure 1.8), $\Delta\mathbf{k}$ associated with the electron transition

is $\neq 0$. Direct transitions between these two points are therefore forbidden since the momentum cannot be conserved. In such semiconductors, indicated as *indirect gap* semiconductors, only indirect transitions can occur, where the participation of an extra particle, specifically a *phonon*, allows the momentum to be conserved²⁰⁻²². Phonons are the quanta of crystal lattice vibrational energy, i.e. the elementary energy unit carriers associated with the quantized modes of lattice vibration of a periodic, elastic crystal structure²¹. In other words they are the relative of photons for the crystal lattice vibrational energy. The fact that in indirect gap semiconductors the electronic transition involves the participation of a phonon together with a photon, means that vibrations of the crystal structure is necessary for the electron transition to occur. Schematic diagrams of direct and indirect transitions are pictured in Figure 1.11²⁰⁻²².

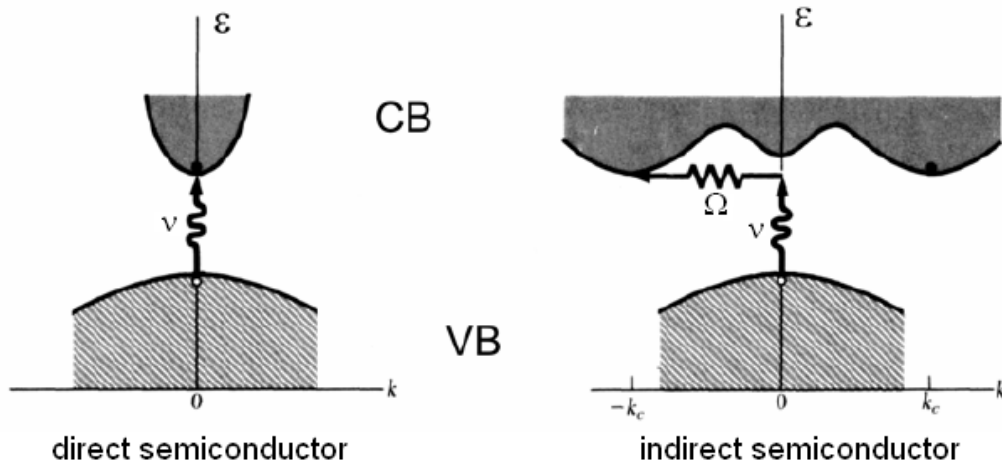


Figure 1.11 – Optical transitions in direct and indirect semiconductors

(v : photon frequency; Ω : phonon frequency).

1.2.3. TiO_2 colloidal semiconductors

After having analysed the basic quantum mechanics associated with solid semiconductors, their band structure, charge carriers and optical excitations, we can now

focus on a single semiconductor, i.e. titanium dioxide which is the main subject of this PhD project.

TiO₂ is a white, highly stable and unreactive metal oxide, present in nature in three different polymorphs: anatase, rutile and brookite. Unlike brookite which is not commonly used, rutile and anatase have been used since the 1920's in many different industrial fields as white pigments due to their high pigmentation power and high stability. In the food industry TiO₂ is also widely used as a colorant (particles are usually coated with thin films of SiO₂) and classified as E171. The anatase polymorph is largely employed in photocatalysis because it is the most photoactive amongst the three polymorphs^{15, 24}. When used in photocatalysis, TiO₂ is usually in the form of small particles with primary particle size (crystallite size) ranging from a few nanometres to one or two hundred nanometres. These colloidal particles are usually used in slurry systems^{3, 15, 25, 26}, anchored to solid supports^{15, 19, 27-31}, used to generate thin films^{6, 15, 32-34} or deposited on conductive supports for the preparation of electrodes used in photoelectrocatalysis^{2, 15, 24, 35}. More recently new photocatalytic systems have been published where TiO₂ is in form of nanotubes³⁶.

TiO₂ is an indirect semiconductor with a band gap of about 3.0 eV^{24, 28, 37, 38} in the case of rutile, 3.2 eV^{24, 28, 37, 38} in the case of anatase and 3.1 eV in the case of brookite³⁹. This means that all the three polymorphs are optically excited by electromagnetic waves in the region of the near UV. Although these are the experimental band gaps derived measuring the absorption edge of the three polymorphs using spectroscopic methods, calculation showed that all of the three polymorphs might show direct transitions too⁴⁰ with band gaps respectively of: 1.78 eV for rutile, 2.22 eV for anatase and 2.20 eV for brookite. These direct gaps are all referred to a $\Gamma - \Gamma$ transition.

Rutile and anatase are both tetragonal and their unit cells contain six and twelve atoms respectively. Ti atoms are coordinated to six O atoms forming TiO₆ octahedra. The octahedra are distorted compared to the regular geometrical structure and in the case of anatase the distortion is greater than the case of rutile. In rutile octahedra share two edges whilst in anatase four. Brookite is structurally different to rutile and anatase. The unit cell is not tetragonal but orthorhombic and the TiO₆ octahedra share a total of three edges.

Figure 1.12 shows the bulk band structure of rutile, anatase and brookite together with their relative Bravais unit cell and octahedra chains ⁴⁰. Table 1.6 groups the crystal structure data for all the three polymorphs ⁴⁰.

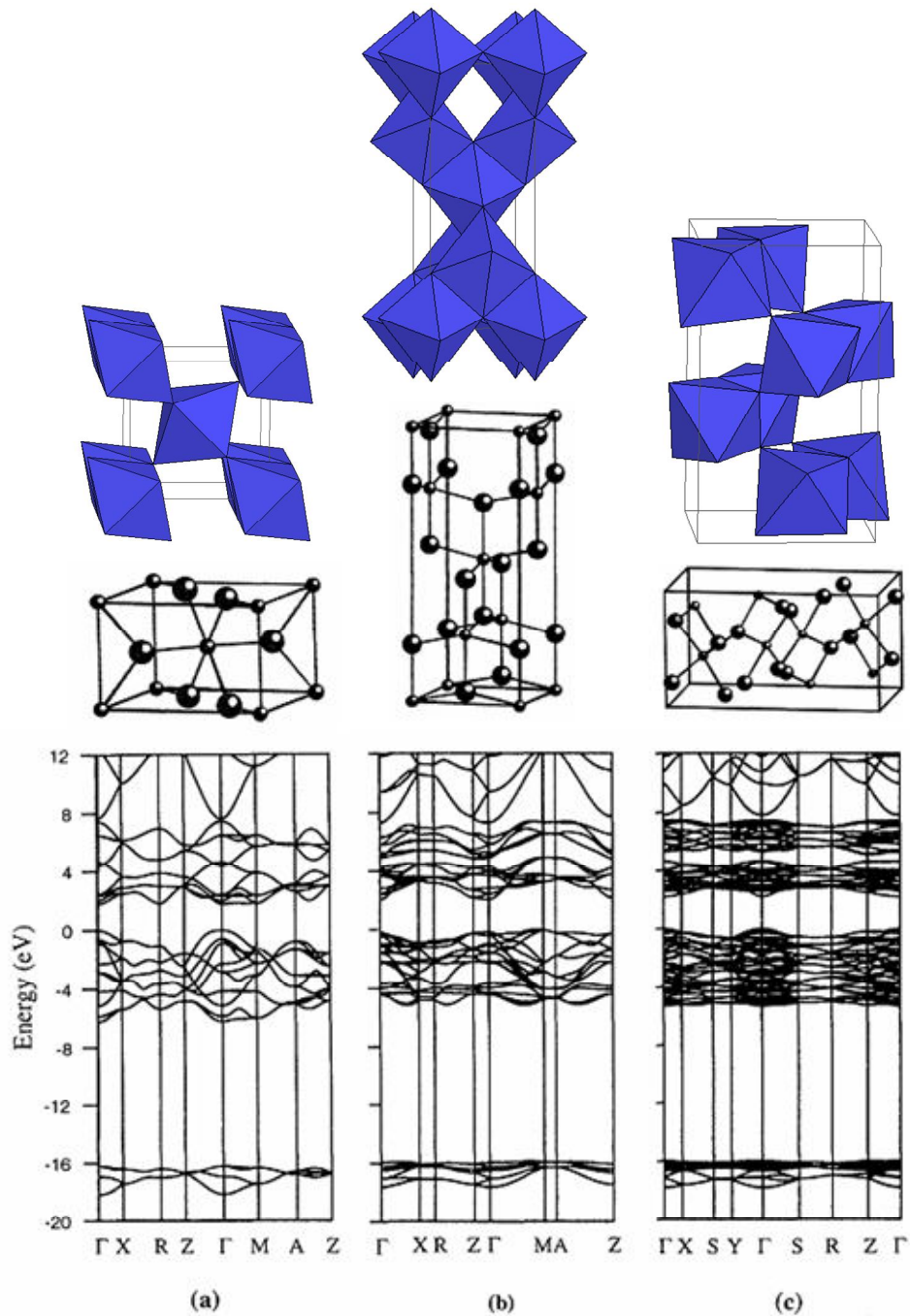


Figure 1.12 – TiO₂ bulk band structure diagrams and Bravais unit cells (ref): (a) rutile; (b) anatase; (c) brookite.

Table 1.6 – TiO₂ crystal structure data.

Parameter	Rutile	Anatase	Brookite
Crystal structure	tetragonal	tetragonal	Orthorhombic
Lattice constants (Å)	a = 4.5936	a = 3.784	a = 9.184
	c = 2.9587	c = 9.515	b = 5.447
			c = 5.145
Space group	P4 ₂ /mmn	I4 ₁ /amd	Pbca
Molecule / cell	2	4	8
Volume / molecule (Å ³)	31.2160	34.061	32.172
Density (g/cm ³)	4.13	3.79	3.99
Ti – O bond length (Å)	1.949(4)	1.937(4)	1.87~2.04
	1.980(2)	1.965(2)	
O – Ti – O bond angle (°)	81.2	77.7	77.0~105
	90.0	92.6	

1.2.4. Preparation of TiO₂ photocatalysts

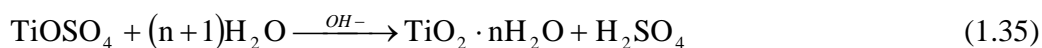
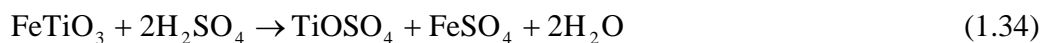
Colloidal TiO₂ particles can be synthesised in several different ways. The final properties of the colloidal TiO₂ extremely depends on the synthetic pathway adopted and the conditions used during the synthesis like temperature, pressure, pH, gas atmosphere in which particles are synthesised, complexing agents and other additional chemical species present during the synthesis, etc... The great majority of the TiO₂ synthetic routes are hydrolytic processes in which a Ti – based compound is hydrolised in controlled pH conditions that usually depend on the starting raw material used. Typical feedstocks are: Ti – based organometallic compounds (like titanium tetra-n-butoxide, Ti(n-C₄H₉O)₄ and titanium tetra-iso-propoxide, Ti(i-C₃H₇O)₄), titanium tetrachloride, TiCl₄ and titanium

sulphate, $\text{TiO}^{2+} \text{SO}_4^{2-}$. Whilst the hydrolysis of Ti – based organometallics is a synthetic route widely used in laboratory and for small scale productions, the processes based upon TiCl_4 and $\text{TiO}^{2+} \text{SO}_4^{2-}$ account for the nearly totality of TiO_2 industrially produced.

In this PhD project the two TiO_2 samples studied are commercially available products manufactured according to the sulphate route. For this reason we focus our attention on the main stages and relative details of the sulphate industrial process and direct the reader to appropriate literature for detailed discussions about the other synthetic route and processes⁴¹⁻⁴⁵.

Figure 1.13 shows a typical operative flow chart of the industrial sulphate process where ilmenite, a mineral containing about 97 – 98 % of FeTiO_3 ⁴⁶⁻⁴⁸, or enriched titanium slags may be used as titanium feedstocks to generate titanium sulphate which undergoes hydrolysis⁴².

The overall process can be summarised by the following reaction series (considering for instance ilmenite as starting feedstock):



Representing respectively:

- i. *digestion of the feedstock*, i.e. TiOSO_4 formation, Equation 1.34;
- ii. *hydrolysis of titanium sulphate*, i.e. hydrated TiO_2 precipitation, Equation 1.35;
- iii. *calcination*, Equation 1.36.

A further surface treatment, involving coating with inorganics (silica is one of the common coatings) and/or addition of organics, is often present when TiO_2 is used as a pigment. Samples designated for photocatalysis are not *usually* treated after calcination.

Particle size and polymorphism are controlled by three crucial steps in the process:

- i. size and type of growth nuclei;
- ii. precalcination additives;

iii. calcination (temperature and residence time).

Hydrolysis of titanium sulphate produces anatase polymorphs (most stable polymorph at low temperature). The nature of the growth nuclei (anatase or rutile) added during precipitation drives phase transitions during calcination and determines, together with calcination temperature and residence time in the rotary kiln, whether or not the final product will be anatase, rutile or a mix of both the polymorphs. Indeed as already stated in the previous section, anatase is the most thermodynamically stable polymorph at low temperature and above 550 – 600 °C it tends to transform into rutile^{49, 50}. Residence time in the rotary kiln can be adjusted (mainly at very high temperature) to control crystal growth. The higher the residence time the higher the probability to sinter small particles into bigger crystallites reducing their specific surface area. Precalcination additives however are often added when big crystallites are needed (> 100 nm). They can be various metal or not metal oxides and control and modulate crystal growth very efficiently, promoting the formation of very big crystallites. During calcination, species introduced with the precalciner may migrate to the surface and modify the surface properties of the final product.

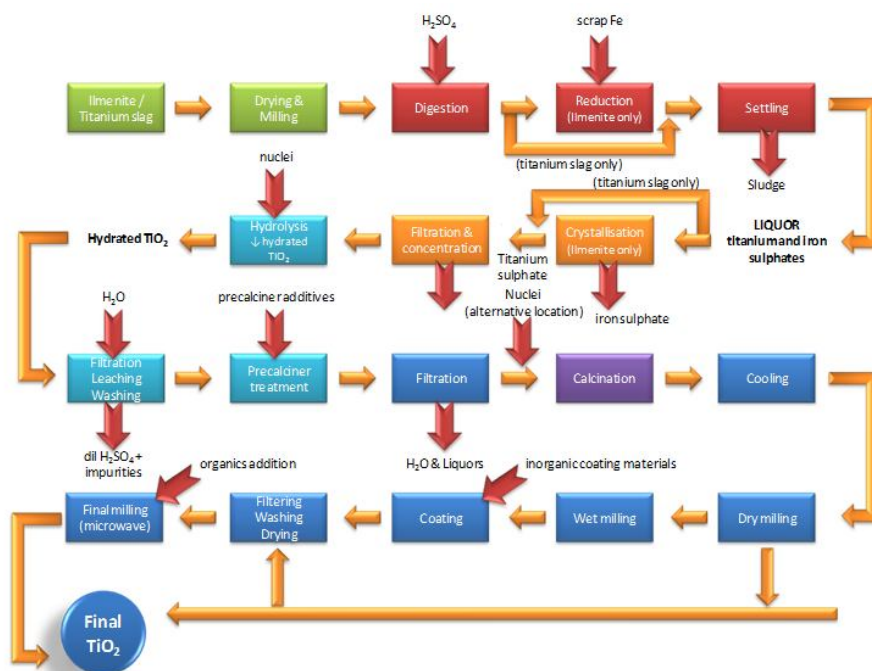
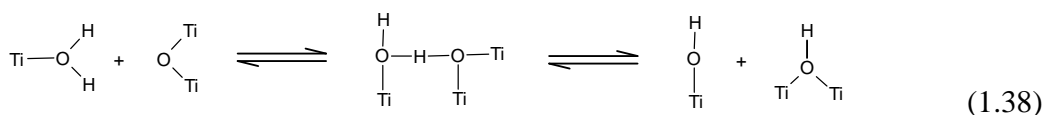


Figure 1.13 – Sulphate process operative flow chart⁴².

1.2.5. Surface chemistry in TiO₂ photocatalysis

The great majority of the studies dealing with TiO₂ surface chemistry refers to specific surfaces^{51, 52}, usually (110) for rutile and (101) for anatase, i.e. the most stable surfaces that these two polymorphs exhibit. In this section however, we adopt a less specific approach and try to offer an overall picture of the surface characteristics of colloidal titania particles.

Unless specifically treated in vacuum and/or high temperature, TiO₂ surfaces are highly hydroxylated^{2, 15, 51-53} resulting in amphoteric titanol groups, Ti – OH, present at the surface. Water on TiO₂ surfaces mainly chemisorbs on oxygen vacancies (V_O) (usually crystal defects), as reported by Trimboli et al.⁵³, Henderson et al.^{54, 55}, Liu et al.⁵⁶, as extensively discussed in the review by Fu et al.⁵⁷ and confirmed by *ab initio* density-functional theory (DFT) calculations by Iacomino et al.⁵⁸. Ti atoms occupy centres of octahedra and coordinate six oxygen atoms. Surface oxygen vacancies lead to five – coordinated titanium atoms able to bind the oxygen of water molecules (Equation 1.37). One of the two hydrogen atoms may form a hydrogen bond with a neighbour bridging oxygen^{53, 55, 57} eventually leading to *terminal* and *bridging* OH groups (Equation 1.38).



Water can also undergoes dissociative chemisorption and generate directly terminal OH groups^{53, 55, 57}. Figure 1.14 (rutile (110) surface) shows some experimental evidence of oxygen vacancies, bridging OH groups and water molecule over a fivefold coordinated Ti atom⁵¹. Similarly Figure 1.15 shows oxygen vacancies on anatase (101)⁵¹.

Electrokinetic properties of TiO₂ depend heavily on the surface hydroxylation. In aqueous suspensions (hydroxylated surfaces) and in the presence of indifferent electrolytes only (i.e. very low polarising ions which do not undergo specific adsorption on the solid particles in suspension), titania exhibits an electrokinetic potential (ζ-potential) that is shown in Figure 1.16.

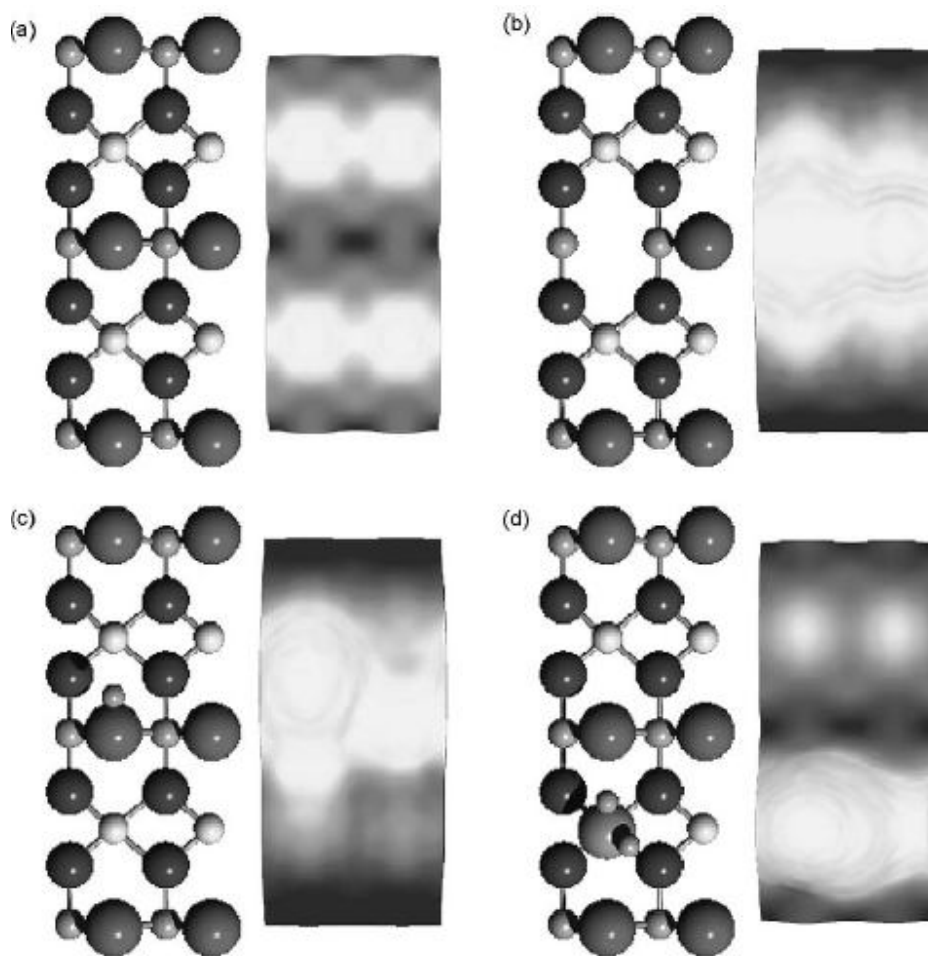


Figure 1.14 – Ball and stick models of rutile (110) and corresponding simulated STM images for: (a) vacancy-free surface, (b) bridging oxygen vacancy, (c) bridging OH group and (d) H₂O molecule on top of a 5 – coordinate Ti atom⁵¹.

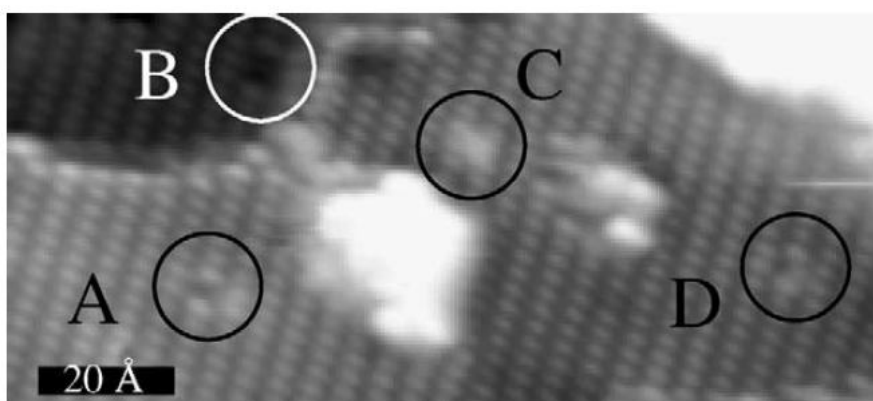


Figure 1.15 – STM image of oxygen vacancies on anatase (101)⁵¹.

This is the electric potential at the shear plane of the *electrical interfacial layer model*⁵⁹ (development of the Gouy – Chapman's *electrical double layer model*⁶⁰) and defines the mobility of the colloidal particles in an electric field as well as agglomeration phenomena if only indifferent electrolytes are present in the solution (DLVO or middle field theory^{61, 62}). The iso-electric point (IEP, pH at which the electrokinetic potential is zero) commonly lies in the range 6 – 7. At pH lower than the IEP colloidal TiO₂ particles form stable suspension since their net positive charge prevents agglomeration phenomena. Similar observations may be made for pH higher than the IEP where the particles show a net negative charge. At the IEP TiO₂ colloidal particles show a net zero charge at the shear plane: agglomeration of particles occurs (no repulsion forces due to same shear plane charges) and, if an electric field is applied to the suspension, they migrate neither towards the positive electrode nor the negative one.

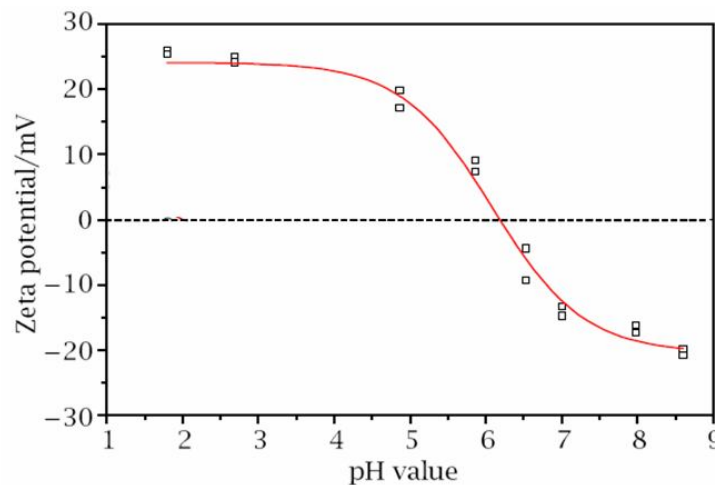


Figure 1.16 – TiO₂ ζ -potential (suspension in indifferent electrolytes solution)²⁵.

The size of the particle agglomerates is known as *secondary particle size*, to differentiate it from the crystallite size commonly referred to as *primary particle size*. These two parameters defines the available surface area of the colloidal TiO₂, therefore they directly influence the adsorption of reactants on the particle surface, i.e. the first step of every TiO₂ photocatalytic reaction (heterogeneous catalysis). In slurry phases at pH far from the IEP and in absence of flocculating ions (usually divalent and trivalent ions), the specific surface area determined by the primary particle size is usually the actual available surface area for any molecule to be adsorbed. In the slurry phase at the IEP or in the presence of

non indifferent electrolytes (presence of highly attractive ion – ion correlation forces⁶³⁻⁶⁶ between particles) as well as in the case of TiO₂ supported to solid materials, the available surface area shown by TiO₂ particle may be much less than the specific surface area. Due to particle agglomeration, complex porous frameworks are formed. If adsorbed molecules have sizes comparable to the interparticle pores, their diffusion in the porous network might be obstructed with the result of a loss of surface area for adsorption. In such cases, the secondary particle size might prevail over the primary particle size in defining the available area for adsorption which might likely be due to the *exposed* area of the particle agglomerates. The area and shape of the agglomerates is a parameter that in many circumstances is extremely difficult to measure experimentally. The case of TiO₂ supported in cement or similar ceramic materials is a typical case. Van Damme in⁶⁷ proposed the application of fractal geometry to theoretically analyse the geometrical features of particle agglomerate in the case of supported TiO₂. Rondet et al.⁶⁸ used the same approach to model the agglomeration of kaolin and concluded that the agglomerate growth process follows fractal geometry laws. Figure 1.17 shows a typical particle agglomerate profile modelled by a Koch's snowflake algorithm where the influence of the primary particle size on the overall profile shape is highlighted.

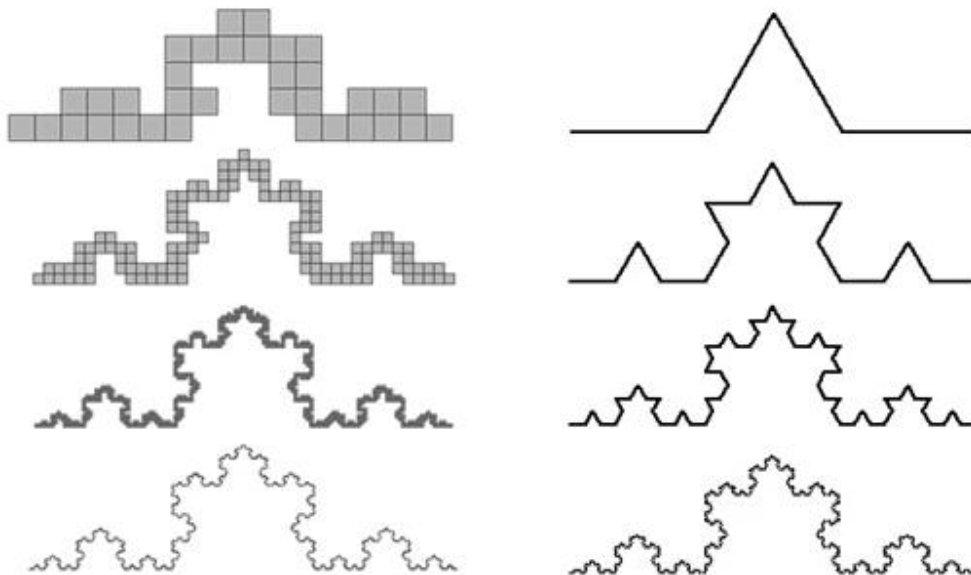


Figure 1.17 – Particle agglomerate profile modelled by the Koch's fractal curve.

Primary particle size can influence agglomeration phenomena too. Abbas et al. showed for a fixed electrolyte concentration that according to the corrected Debye-Hückel theory of surface complexation, the smaller the particles, the higher their surface charge density due to an improved screening efficiency of the counter-ions (see the electrical interfacial layer model ⁵⁹) as the particle surface becomes increasingly curved ⁶⁹. This effect, confirmed by Monte-Carlo simulations, is extremely enhanced below a particle diameter of 10 nm. Since the attractive ion – ion correlation forces introduced before when non indifferent electrolytes are present in the system are expected at high surface charge densities ⁶⁵, it is clear that in these conditions the smaller the primary particle size, the higher the degree of agglomeration.

Finally, TiO₂ electrokinetics does not only influence surface adsorption through agglomeration/dispersion. The charge on particles, when the pH of the medium is far from the IEP, promotes adsorption phenomena if molecules and ions possess opposite charges than the solid surface but inhibits adsorption if adsorbates are characterised by the same charge as the solid. An interesting example of this is provided by Chen et al. ²⁵ for the different adsorption modes of rhodamine B (RhB) on TiO₂ particles in slurry systems at different pHs (Figure 1.18). For pHs higher than the RhB pK_a (3.7 according to Woislowski ⁷⁰) but below the TiO₂ IEP (i.e. positive TiO₂ surface, Figure 1.16), the molecule is adsorbed through the negatively charged carboxylic group. For pHs higher than the IEP, the TiO₂ surface becomes negative and the RhB is adsorbed through the positive charge delocalised across the aromatic ring structure in between the two amino groups.

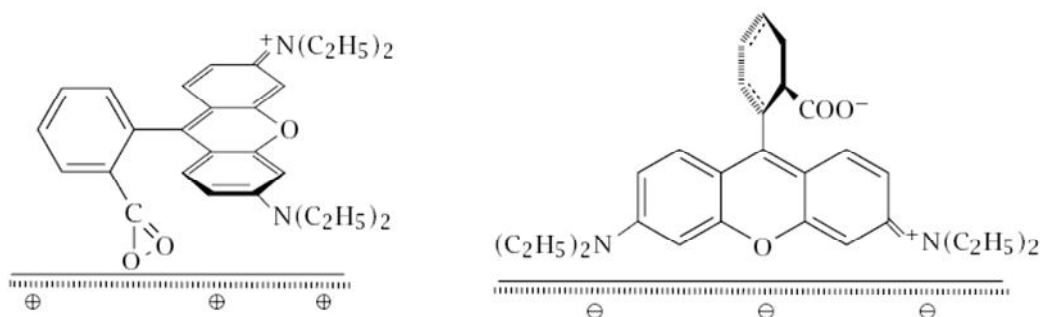


Figure 1.18 – Adsorption modes of rhodamine B on charged TiO₂ surfaces.

1.2.6. Thermodynamics and kinetics in TiO₂ Photocatalysis

1.2.6.1. Thermodynamics

In section 1.2.2 we have already seen that the first step of every semiconductor sensitised photoreactions is the photoactivation of the semiconductor photocatalyst through optical excitations. When the optical transition occurs, valence band positive holes and conductance band free electrons are generated in the TiO₂ band structure. In photocatalysis this is commonly sketched out by the diagram in Figure 1.19.

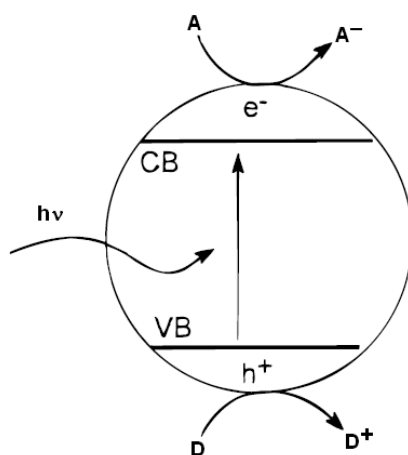


Figure 1.19 – TiO₂ sensitised photoreaction.

The species indicated as A and D represent an electron acceptor and a positive hole scavenger respectively. From a great number of experimental evidences^{2, 4, 15, 24}, it is known that rarely organics and inorganics react directly with positive holes and free electrons, but the oxidation reactions they undergo on photoactivated TiO₂ surfaces are mainly driven by highly oxidative species like hydroxyl radicals, $\cdot\text{OH}$, superoxides, $\text{O}_2^{\cdot-}$, peroxides, HO_2^{\cdot} , etc..., all generated by initial interaction of oxygen with conduction band electrons and water and/or surface OH groups with valence band positive holes. Equations 1.39 – 1.46 show the reaction network involving O_2 and H_2O ⁷¹.





which correspond to the overall reaction:



Figure 1.20 shows the redox potentials of positive holes and free electrons for the two polymorphs rutile and anatase together with the main redox equilibria of O_2 and H_2O at three different pHs.

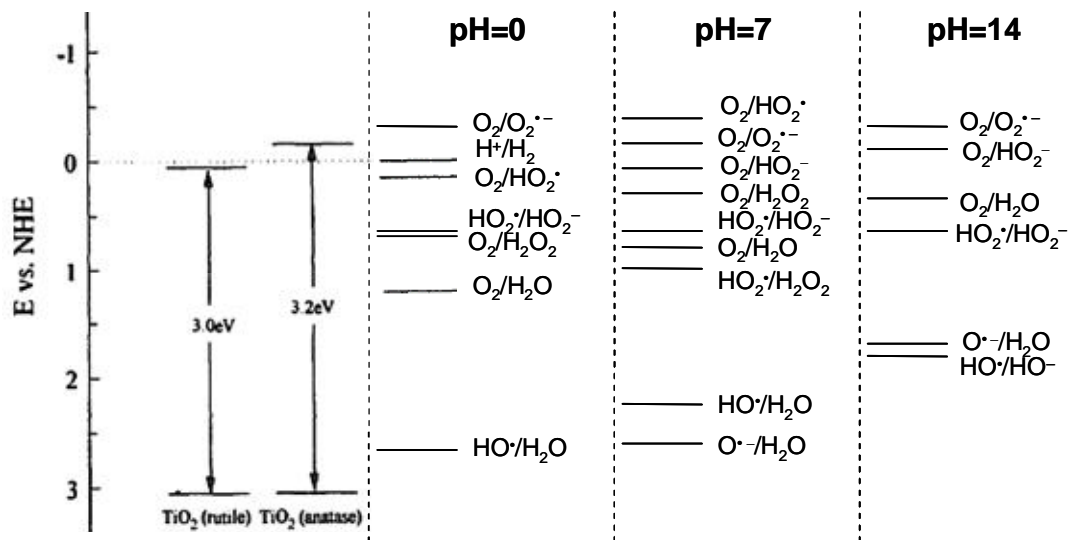


Figure 1.20 – Redox potentials of rutile and anatase conductance band electrons and valence band positive holes compared to redox potentials of O_2 and H_2O equilibria.

Whatever the actual mechanism of reaction and relative species involved, a generic photocatalytic process can be represented through Equation 1.47 ⁴:



where $h\nu$, the energy of the incident light, must be equal or higher than the semiconductor band gap. To catalyse reactions like 1.47, the redox potential of valence band holes must be higher than the half-cell D^+/D and the redox potential of the conductance band electrons lower than the half-cell A/A^- . If, in the absence of light and photocatalyst, the variation of the standard free Gibbs energy, ΔG° , associated with the reaction in Equation 1.47 is positive, the process is referred to as *photosynthesis*; on the other hand, if ΔG° is negative, we refer to proper *photocatalysis*⁴. Table 1.7⁴ shows specific examples for Equation 1.47.

Although the term *photocatalysis* is now a common and universally accepted term to refer to such photochemical processes, questions have been raised as to whether or not it is appropriate. Photocatalysis would indeed suggest that light is acting as a *catalyst*, whilst light is actually a *reactant* consumed in the overall reaction like any other. In this respect the term *photosensitisation* is much more appropriate, indicating a process where a photochemical alteration occurs in one or more chemical species as a result of the initial light absorption by another species called *photosensitizer*^{2, 4}. Such a definition also allows the discrimination between two distinct mechanisms that can occur: *sensitised photoreaction* and *catalysed photoreaction*^{2, 4}. Sensitised photoreactions are the ones described so far in this section and sketched in (Figure 1.19). Catalysed photoreactions on the other hand, often occur when the incident light photons have energy lower than the semiconductor band gap but enough to promote electronic transitions between HOMO (Highest Occupied Molecular Orbital) and LUMO (Lowest Unoccupied Molecular Orbital) of a suitable adsorbed molecule (Figure 1.21). Electrons are further injected from the LUMO of the adsorbed molecule to the conductance band of the semiconductor, where they can react with the electron acceptor species like O_2 and produce oxygen-based oxidative species like superoxides and peroxides. A typical example of such a process is the famous Grätzel cell³³ where dye molecules are degraded on TiO_2 films using visible light. Visible light is indeed not energetic enough to photoactivate TiO_2 but energetic enough to excite the dye molecule as shown in Figure 1.21 and starts its own mineralisation. In the particular case of dyes the catalysed photoreaction is often referred to as *dye sensitised photoreaction*^{25, 28, 33}.

Table 1.7 – TiO₂ – sensitised photosynthetic and photocatalytic processes ⁴.

Reaction	Description	ΔG° <i>kJ mol⁻¹</i>
<i>Photosynthesis</i>		
$H_2O + H_2O = 2H_2 + O_2$	Water splitting	475
$2CO_2 + 4H_2O = 2CH_3OH + 3O_2$	Carbon dioxide reduction	1401
$2N_2 + 6H_2O = 4NH_3 + 3O_2$	Nitrogen reduction	1355
$6CO_2 + 6H_2O = C_6H_{12}O_6 + 6O_2$	Green plant photosynthesis	2895
<i>Photocatalysis</i>		
$3O_2 + 2CH_3OH = 4H_2O + 2CO_2$	Methanol mineralisation	– 1401
$2HAuCl_4 + CH_3OH + H_2O = 2Au + 8HCl + CO_2$	Deposition of metals	–
$6H_2O + C_6H_{12}O_6 = 12H_2 + 6CO_2$	Biomass conversion	– 32

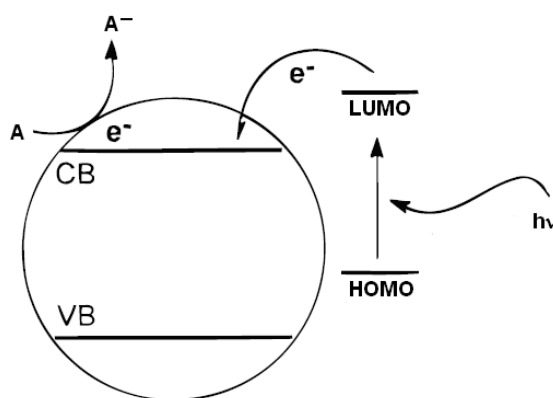


Figure 1.21 – catalysed photoreaction.

1.2.6.2. Kinetics

In the previous section we highlighted how commonly photocatalytic oxidation of organics and inorganics proceeds through initial interactions of oxygen and water with the photogenerated charge carriers in the band structure of the semiconductor TiO₂ forming oxygen-based species which ultimately oxidise the target molecule. In section

1.2.2 however, we also saw how the photogenerated electron – hole pairs may recombine re-establishing the initial ground state. For colloidal TiO_2 particles the overall situation can be represented according to the diagram in Figure 1.22 ⁴.

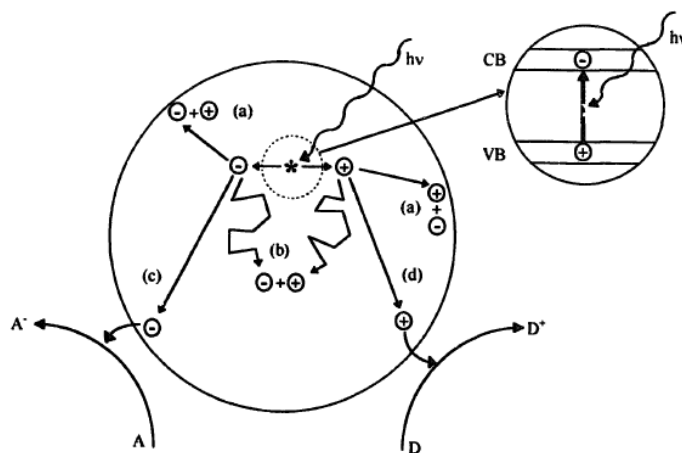


Figure 1.22 – Charge carriers photogeneration and recombination.

Volume wavefunctions representing the photogenerated electron – hole pairs have high probability of recombination and consequent transition to the initial ground state. Surface wavefunctions however are characterised by a lower probability of recombination since adsorbed molecules can *trap* the photogenerated charge carriers and undergo chemical reactions. The kinetics of such dynamic processes is outlined in Table 1.8 in the case of hydroxylated TiO_2 surfaces and in the presence of oxygen.

Interesting features about the TiO_2 sensitised photoreaction primary processes can be observed:

- i. formation of conduction band electron can be associated with the formation of a $\text{Ti}^{(\text{III})}$ centre;
- ii. OH groups play a fundamental role in the trapping of the photogenerated charge carriers;
- iii. the interfacial conduction band electron transfer (Equation 1.55) is the slowest between all the semiconductor charge carrier processes, therefore it is expected to influence the overall photocatalytic reaction rate.

Table 1.8 – Primary processes and associated characteristic time domains in the TiO₂-sensitized photoreactions ².

Primary process	Equation	Characteristic time
Charge carrier generation		
$\text{TiO}_2 + h\nu \longrightarrow h^+ + e^-$	(1.48)	fs (very fast)
Charge carrier trapping		
$h^+ + \text{Ti}^{\text{IV}}\text{OH} \longrightarrow \{ \text{Ti}^{\text{IV}}\text{OH}^\bullet \}^+$	(1.49)	10 ns (fast)
$e^- + \text{Ti}^{\text{IV}}\text{OH} \longleftrightarrow \{ \text{Ti}^{\text{III}}\text{OH} \}$	(1.50)	100 ps (shallow trap, dynamic equilibrium)
$e^- + \text{Ti}^{\text{IV}} \longrightarrow \text{Ti}^{\text{III}}$	(1.51)	10 ns (deep trap)
Charge carrier recombination		
$e^- + \{ \text{Ti}^{\text{IV}}\text{OH}^\bullet \}^+ \longrightarrow \text{Ti}^{\text{IV}}\text{OH}$	(1.52)	100 ns (slow)
$h^+ + \{ \text{Ti}^{\text{III}}\text{OH} \} \longrightarrow \text{Ti}^{\text{IV}}\text{OH}$	(1.53)	10 ns (fast)
Interfacial charge transfer		
$\{ \text{Ti}^{\text{IV}}\text{OH}^\bullet \}^+ + \text{org} \longrightarrow \text{Ti}^{\text{IV}}\text{OH} + \text{ox org}$	(1.54)	100 ns (slow) (*)
$\{ \text{Ti}^{\text{III}}\text{OH} \} + \text{O}_2 \longrightarrow \text{Ti}^{\text{IV}}\text{OH} + \text{O}_2^{\bullet -}$	(1.55)	ms (very slow)

The kinetics of the entire photocatalytic process can be described, once again, considering an overall reaction with no particular focus on the actual mechanism ². For decades, kinetics of photocatalytic processes has been studied according to a *Langmuir – Hinshelwood* (LH) approach. For the generic reaction in Equation 1.47, the rate of reaction is derived through Equation 1.56:

$$r = k_{\text{overall}} \frac{K_A K_D C_A C_D}{(1 + K_A C_A + K_D C_D)} \quad (1.56)$$

where r is the reaction rate, k_{overall} an overall rate kinetic constant, K_A and K_D the Langmuir adsorption constants for the reactants A and D and C_A and C_D the concentrations of the same reactants.

The LH kinetics implies that both the reactants are first adsorbed on the TiO_2 surface and subsequently react generating the products that eventually desorb from the surface. Furthermore the model assumes fast adsorption/desorption equilibrium steps and a slow surface step⁷². In many cases however the LH conditions are only assumed since there is no certain evidence that all these necessary conditions are met. Recently several authors have started to question the applicability of LH kinetics to photocatalytic processes^{72, 73}, proposing other kinetic approaches like for instance kinetic models based upon Freundlich adsorption isotherms⁷⁴.

1.2.6.3. Quantum Yield and Photonic Efficiency

The rate (overall) of a photocatalytic reaction is also used to derive the *overall quantum yield*, Φ_{overall} ^{2, 4}:

$$\Phi_{\text{overall}} = \frac{r}{\varphi} \quad (1.57)$$

where r is the rate of reaction and φ the rate of absorption of radiation. The quantum yield is a fundamental parameter to quantify the efficiency of a given photocatalytic process. The term *overall* is used to differentiate the above mentioned quantity from the *primary quantum yield*. The primary quantum yield refers as to the number of species converted in a process that involves direct absorption of radiation (primary process) over the number of photons absorbed for that given specific process. The overall quantum yield however refers as to the total number of species converted via primary and secondary processes over the total number of photons absorbed.

These quantities are often difficult to measure due to the difficulty in assessing the rate of absorption of ultra band gap photons responsible for the optical excitation⁴. TiO_2 colloidal particles indeed, not only absorb light, they also scatter and transmit the incident

radiation too. For this reason another term is introduced, much easier to assess. It is usually referred to as *photonic efficiency*, ξ , and defined through Equation 1.58⁴:

$$\xi = \frac{r}{I_0} \quad (1.58)$$

where r is again the rate of reaction and I_0 the intensity of the monochromatic incident light. As we said above, the incident light is not 100 % absorbed but also scattered and transmitted. This implies that for any photocatalytic process $\Phi_{overall} \geq \xi$.

1.3. The cement – TiO₂ system

1.3.1. Properties and interactions

TiO₂ is usually dry mixed with cement powder before adding water for hydration. When cement hardens, TiO₂ is present throughout the formed cement structure. TiO₂ is a highly stable, highly inert oxide. It does not react with any cementitious phase and it is not involved in any hydration reaction. From a material structural point of view, it acts as pore filler reducing the degree of porosity with some benefits for the early stage strength. Although no chemical reactions involving TiO₂ occur, once water is added to hydrate the cement powder, the newly formed chemical environment is expected to modify dramatically the surface chemistry and the electrokinetic properties of titania particles. The amphoteric titanol groups, Ti – OH, are titrated by the OH[–] present in the alkaline solution, generating a negative Ti – O[–] surface. The presence of multivalent cations like Ca²⁺ at high ionic activities is expected to establish strong ion – ion correlation forces between Ti – O[–] negative surfaces and Ca²⁺ counterions. As a result, TiO₂ particles agglomeration is expected. This speculation is based upon experimental evidences obtained studying ion – ion correlation forces between SiO₂ colloidal particles in highly coupled systems ⁶⁵ and cohesion of CSH particles ⁶⁴ in cement. No significant data however were present in the literature about TiO₂ electrokinetics in cementitious systems with direct correlations with the surface chemical composition. During this PhD project we have been able to study accurately such systems and contribute to clarify the surface interactions between TiO₂ colloidal particles and cement environment. The reader will find detailed discussions in the experimental section of this thesis and in Folli et al. ⁶³.

1.3.2. Self-cleaning effect

1.3.2.1. *Degradation of adsorbed organics and super-hydrophilicity*

As a common phenomenon the aesthetic of ordinary buildings is gradually lost over time due to aging and the influence of weather. Building surfaces could for example be soiled

by greasy and sticky deposits, which result in a strong adherence of ambient dusts and atmospheric fine particles causing dirt to be built up on the surface. Restoration of the buildings' aesthetic properties is therefore achieved through constant and proper maintenance, which often involves the use of chemicals and energy consuming methods. The applications of self-cleaning building materials provide an excellent solution to this problem.

As a coating on flat, smooth and non porous surfaces like glass, the photoactivated TiO_2 provides self-cleaning properties by:

- i. oxidising organic molecules causing dirt and stains ^{2, 4, 15};
- ii. efficiently removing carbon-based residues (if organics are not completely mineralised) and adsorbed inorganics due to the photo-induced super-hydrophilicity of the TiO_2 surface ^{16, 17}.

In the case of TiO_2 dispersed in cement, photocatalyst particles do not form a homogeneous film on the surface of the solid material. Furthermore hardened cement is a porous medium and real concrete or mortar surfaces are never highly smooth but rather rough. As a result, in the case of cement containing TiO_2 , the photo-induced super-hydrophilic character of the solid surface can be significantly reduced. Self-cleaning properties depend almost entirely by the efficiency of oxidising organic molecules. Visible stains on building surface are constituted by composite materials mainly originated from the atmospheric aerosol pollutants. Small particles and greasy deposits are adhered to building surface by organic binders such as hydrocarbons and fatty acids [30]. Taking fatty acid molecules for example, their carboxylic groups ($-\text{COOH}$) enable them to stick on building surface via chemical binding with calcium ions present in concrete; on the other hand, their long chains link with other hydrophobic molecules perpendicularly to the surface, resulting in fatty stains which trap many atmospheric particles and dusts. The great redox power of the UV induced oxygen based radicals formed on the surface of the irradiated TiO_2 photocatalyst can decompose the organic binders. Water and oxygen necessary to the formation of $\cdot\text{OH}$ radicals are provided by the atmosphere whilst the UV light necessary for the TiO_2 activation is the small percentage of UV radiation contained in sunlight that reaches the Earth surface (average solar

radiation composition is ≈ 48 % visible light, ≈ 44 infrared light and $\approx 7 - 8$ % UV light filtered for more than 90 % by the ozone layer in the lower portion of the stratosphere).

When referring to self-cleaning properties, we are referring exclusively to the surface of the cementitious material. Moreover, chemicals responsible for dirt and stains are usually very big organic molecules present in the atmosphere that adsorb on the exposed cementitious surface. For these reasons, TiO_2 particles in the cementitious binder are required to be highly dispersed in small particle agglomerates and not occluded by potential cementitious phases crystallising on the surface of the forming solid material (reduction of the available TiO_2 surface area). The first requirement can be achieved selecting an appropriate titania sample with adequate particle size and with surface properties allowing formation of small agglomerates. The second one can be optimised adopting specific engineering strategies like casting formliners that reduce the water to cement ratio (W/C) at the surface of the forming solid material during cement hydration (see sections 2.5.1 and 3.3.1).

In outdoor conditions the aesthetic durability of buildings constructed with cement containing TiO_2 is monitored by measuring the variation with time of the colour components (CIE Lab model ^{75, 76}) of the façade ^{9, 19}. This is a direct measure of the self-cleaning activity provided by TiO_2 in the cementitious binder (see example in section 1.1.3). In laboratory, the self-cleaning activity is usually assessed by spectroscopic methods monitoring the degradation of dye molecules deposited on the surface of mortar or concrete specimens at various irradiation times ^{28, 77} (see section 2.4.1).

1.3.2.2. Research development and practical applications

Several research studies have confirmed the self-cleaning effectiveness of photocatalytic cementitious binders. Cassar et al. ⁷⁸ mixed a TiO_2 into white cement pastes to achieve photocatalytic effect. White cement specimens were impregnated with a 0.1 mg/ml phenanthroquinone solution. After UV irradiation, the yellow colour faded allowing a rapid restoration of the white surface. In the European Project PICADA project photocatalytic cementitious products (mortars and cementitious coating paints) were

developed. The self-cleaning effect has been proved by degradation of Rhodamine B, a red organic dye, by colorimetric measurements. The experimental results showed that the samples recovered about 65% of their initial coloration in less than a day of exposure to artificial sunlight ⁷⁹. In addition, the validity of self-cleaning cementitious products was demonstrated by colorimetric monitoring of buildings constructed using this kind of materials. Laboratory results about self-cleaning effect of photocatalytic cementitious surfaces have been also proved to be achieved in *real world* application. In the church *Dives in Misericordia* in Rome, over a total monitoring period of six years, only a slightly difference between the external and internal values of the lightness was observed. The art city hall in Chambéry (France) showed colour variations of the panels caused by inorganic substance could be completely eliminated by washing with water. Regarding the city hall in Chambéry, the primary color almost remained constant for approximately 5 years in different positions of the facade (West/ North/East/South) ¹⁹. Besides self-cleaning cementitious materials, TiO₂-based self-cleaning exterior building products including tiles and glass have been widely commercialized and applied. About 270 patents have been registered in the photocatalytic technology domain by TOTO Ltd. Their representative products are white ceramic tiles for exterior walls and home environments. They are fabricated by spraying a liquid suspension containing TiO₂ powder or gel on the surface and then heated to 600–800 °C.

1.3.2.3. *Problems and limitations*

Durability of the photocatalytic performance is a crucial factor for photocatalytic self-cleaning building materials. For tiles and glass, because of the high temperature treatment, the photocatalyst layer is usually stable and permanent ⁸⁰. In the case of concrete surfaces, the use of organic admixture for concrete and other cementitious materials must be minimized to avoid possible reduction of the photocatalytic activity. Furthermore, if TiO₂ is intimately mixed with cement prior concrete production, the use of specific membranes to decrease the water to cement ratio on the front casting surface is recommended. This helps to decrease extensive Portlandite (Ca(OH)₂) formation on the surface that, crystallising in the form of large plates, significantly occludes TiO₂ clusters

reducing the overall self-cleaning ability of the newly formed photocatalytic surface. The self-cleaning effect may also be limited due to the physical anchoring of the dirt in large pores. Nowadays long term durability of self-cleaning concrete facades is hard to assess because the first buildings have been constructed no more than 10 years ago. However, in this period of time, no significant reductions of photocatalytic performances have been registered and self-cleaning properties are still maintained.

1.3.3. Depollution effect

1.3.3.1. Outdoor air pollution

When referring to the *depollution effect* provided by concretes containing TiO_2 , we mainly refer as to the ability to remediate air pollution through photocatalytic oxidation of NO_x (present in the atmosphere) into nitrates, NO_3^- . Due to the very large exposed surface area of buildings, sidewalk, roads, etc..., photocatalytic strategies like introduction of TiO_2 into concretes and various construction materials may very well offer a chance to significantly improve the air quality of cities and industrialized areas.

NO_x is a term used in atmospheric chemistry to indicate the sum of NO and NO_2 . NO is directly introduced into the atmosphere from a source (e.g. high temperature combustion in transport and industry⁸¹⁻⁸⁴). NO_2 is formed in the atmosphere by reaction between NO and ozone, O_3 , or molecular oxygen (even though the reaction with the latter is kinetically slow) assisted by sunlight⁸¹⁻⁸⁴. Further reactions in the atmosphere can transform NO and NO_2 into nitric acid, HNO_3 , peroxyacyl nitrates (PANs), RC(O)OONO_2 , peroxyxynitric acid, HNO_4 , etc... The sum of all these species and NO_x is known as NO_y , *reactive nitrogen compounds*. NO_x are mainly responsible for *photochemical smog*⁸² (a mixture of hazardous chemicals derived from the interaction of sunlight with atmospheric pollutants), and together with sulphur oxides (SO_x) generate acid rains⁸²⁻⁸⁴. By direct exposure, or from acid vapours arising from their interaction with atmospheric moisture, they can cause emphysemas and bronchitis in humans⁸². Further, they can seriously affect regular metabolic processes in plants⁸².

The control and remediation of atmospheric NO_x has been largely driven by environmental legislation. The prevention and remediation technologies for NO_x, include combustion modifications, dry and wet processes⁸⁵⁻⁸⁷. Photocatalytic oxidation (PCO) of NO_x using titanium dioxide as semiconductor photocatalyst has become, over the past ten years, a competitive alternative, as confirmed by the growing number of commercial products available on the market and the increasing scientific focus^{4, 5, 8, 29-31, 71, 88-94}.

The photocatalytic mechanism is dependent on the semiconductor properties of TiO₂. Under illumination with UV light and in presence of oxygen and water, ·OH radicals are generated (Equations 1.39 – 1.46). The proposed reaction mechanism (Devahasdin et al.⁷¹) is rather complex and involves a long series of reactions where, on the TiO₂ surface, adsorbed NO reacts with adsorbed ·OH forming nitric acid, HNO₃, passing through two intermediates: unstable nitrous acid, HONO, and nitrogen dioxide, NO₂. The photocatalytic reaction network is shown in Figure 1.23.

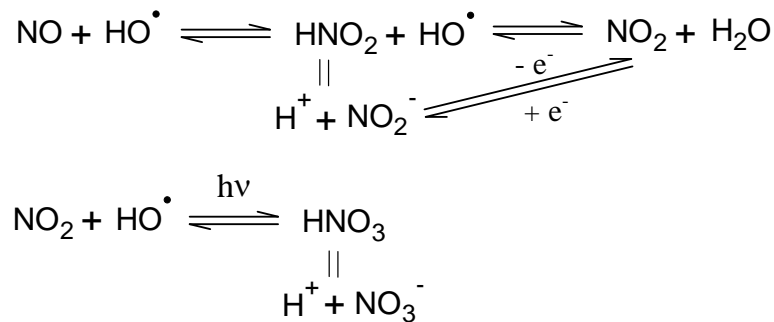


Figure 1.23 – Reaction network for TiO₂-sensitised photo-oxidation of nitrogen oxides.

The same reaction pathway is still considered valid for TiO₂ contained in concretes. However, due to the very high pH typical of the cement environment, the reaction products and the intermediates are likely to be associated with NO₂⁻ and NO₃⁻ rather than HONO and HNO₃.

Outdoor air pollution remediation performances of concretes containing TiO₂ are assessed by measuring the concentration of NO and NO₂ in the air close by the photocatalytic surface and comparing it with the average concentration of NO_x of similar polluted areas where no photocatalytic surface is present. In laboratory specimens are

usually introduced in gas flow reactors where the NO and NO₂ concentration variations with irradiation time are monitored (section 2.4.2.1).

1.3.3.2. Indoor air pollution

Indoor air pollutants mainly include nitrogen oxides, VOCs and particulates. The improvement of indoor air quality is achieved by abatement of organic chemicals (most of which highly volatile) present in the indoor atmosphere due to ordinary human activities. These chemicals (alcohols, aldehydes, hydrocarbon solvents, aromatic compounds, etc...) are common ingredients in a wide series of household products such as: detergents, disinfectants, paint, perfumes, deodorants and cosmetics, and released in the indoor atmosphere during normal usage and storage. Furthermore, active photocatalytic surfaces can help in reducing the proliferation of moisture-induced mold colonies, bacteria and fungi due to the oxidative power of the photocatalyst once irradiated with light of sufficient energy^{2, 4, 15}.

1.3.3.3. Research development and practical applications

In big cities with dense population the pollutant concentration at street level is quite high because the dispersion of the exhausts generated by a large number of vehicles is hindered by the surrounding tall buildings⁸⁰. For these cities applying TiO₂ modified cementitious materials onto the external covering of buildings or roads may be a good supplement to conventional technologies such as catalytic converters fitted on the vehicles for reducing gaseous exhaust emission⁸⁰. Concrete pavement and building vertical surfaces provide optimal substrates for the application of photocatalytic solutions given the large surface area exposed and the relatively flat configuration of the facades that facilitate the exposure of the photocatalyst to sunlight. The whole removal process of pollutants is driven by natural energy alone since, apart from the presence of the photocatalyst, the only requirements are sunlight, atmospheric moisture and rain. The air remediation effect of photocatalytic cementitious materials has been proved by a large number of laboratory studies and *real world* tests. In laboratory nitrogen oxides (NO_x)

and volatile organic compounds (VOCs) have been chosen by most studies as representative airborne pollutants due to their potential health risks and ability to generate photochemical smog ⁸⁰. The NO removal paving blocks made by waste materials and TiO₂ were evaluated by Poon and Cheung ⁹². They found that an optimum mix design which incorporated recycled glass, sand, cement and 10 % TiO₂ achieved 4.01 mg h⁻¹ m⁻² NO removal. Hüsken et al. ^{95, 96} carried out comparative analyses of different photocatalytic cementitious products using a laminar flow reactor. They pointed out that the efficiency with respect to NO_x degradation varied significantly and in the best scenario some products achieved 40 % degradation. The best amongst the tested paving stones was selected for further modeling using a Langmuir-Hinshelwood kinetic approach ⁹⁷. The established model allowed for: i. the prediction of the performance of certain air-purifying concrete products under various conditions; ii. the scale up of the material air mitigation properties in relation to an outdoor site test (Castorweg road, 1000 m², Hengelo, THE NETHERLANDS). Conducting very similar tests on photocatalytic paving blocks (TiO₂ only on the surface of the tiles) Beeldens ⁸ reported enhancement of air-cleaning performances by increasing the surface area, reducing the air flow rate and increasing the turbulence of the pollutant in the test reactor. Strini et al. ⁹⁸ carried out photodegradation of selected VOCs (benzene, toluene, ethylbenzene and *o*-xylene, i.e. BTEX) in gas phase at ppb concentrations on the surface of photocatalytic cementitious materials. They observed that the photocatalytic activity of pure TiO₂ sample was three to ten times greater than the cementitious sample that was prepared with the incorporation of 3% catalyst. The decomposition rate of BTEX was linearly dependent on the concentration of the reactant and the intensity of the irradiation. However, the catalytic activity was not linearly dependent on the TiO₂ content in the samples probably because the formation of highly agglomerated catalyst clusters in the cementitious paste was influenced by the different viscosities of the paste. Other photocatalytic construction material solutions were investigated by Demeestere et al. ⁹⁹, who roofing tiles and corrugated sheets for the removal of toluene from air. They reported toluene removal efficiencies of 78 ± 2 % with an elimination rate higher than 100 mg h⁻¹ m⁻². Results showed that low toluene removal performance occurred at high relative humidity and high inlet concentration, whereas better performance was observed with increased

residence time. They also found a decrease of photocatalytic activity by a factor of 2 when the photocatalytic building materials were operated at high pollutant concentration levels, $[TOL]_{in} > 76 \text{ ppmv}$ ⁹⁹.

The series of laboratory tests presented above served as a scientific basis to support a number of real world applications and pilot tests executed throughout Europe over the past ten years. In Bergamo, ITALY, a street in the city centre was re-paved by the photocatalytic concrete paving blocks (total area of about 12000 m²). NO_x concentration was measured by chemiluminescence analysers simultaneously on two sites: the area where photocatalytic blocks were present and the extension of the road paved with normal bituminous concrete used as a reference. The air monitoring campaign showed an average NO_x abatement of 45% in day time (from 9 am to 5 pm) 29. PICADA project¹⁰⁰ assessed the benefits provided by the use of TiO₂-based photocatalytic cementitious materials and, laboratory results have been compared to results in real world conditions by monitoring the efficiency of photocatalytic pavers in a car park and photocatalytic vertical walls in a simulated street canyon. Experimental evidence showed that abatement of hazardous gas pollutants like NO_x (in climatic conditions typical of South of Europe) can reach and, in some optimal conditions of light exposure, wind circulation, initial pollutants concentration depending on traffic conditions, etc..., breakthrough the threshold of 60 %. This was also confirmed by other independent tests. For instance, the implementation of ordinary TiO₂ in concrete over a total area of about 7000 m² of the roads in Milan, ITALY, contributed to a reduction by 60 % the NO_x concentration in the air in one single year^{7, 101}. In a parking area in Segrate, ITALY, Global Engineering, a contractor nominated by the City Council to repave several areas with Italcementi TX Active products, measured similar abatements over a period of nine months. In Antwerp, BELGIUM, 10000 m² photocatalytic pavement blocks have been used to execute a new parking lane. Measurements on the site indicated a 20 % drop of NO_x concentration due to the presence of the photocatalytic materials⁸. In the municipality of Hengelo, THE NETHERLANDS, 1000 m² pavement area has been replaced with photocatalytic paving stones. First on site results showed a total NO_x abatement between 25 and 45 %¹⁰². A 250 m² pavement area in Lysegrå Malmö, SWEDEN, was executed using photocatalytic paving blocks. A total abatement between 5 and 27 % was recorded. NO_x degradation

performance of the photocatalytic tiles was found highly dependent from seasonal climatic variations and wind conditions¹⁰³.

Together with cement-based materials, a series of photocatalytic paints have been developed and are commercially available. Photocatalytic paints and photocatalytic cementitious coatings are the preferred solutions for indoor applications. Maggos et al.¹⁰⁴ investigated the air remediation potential of a white acrylic TiO₂-containing paint by painting the ceiling of an indoor car park and illuminating it with UV lamps. The artificially closed area of the car park was polluted with car exhausts. Over a total period of 5 h of UV illumination, NO and NO₂ were reduced by 19 % and 20 % respectively. TiO₂-zeolite systems are also very effective for indoor environments. Ichiura et al.^{91, 105} showed that these composites are very efficient in removing NO_x, toluene and formaldehyde, although for the latter lower conversions have been achieved.

1.3.3.4. Problems and limitations

Although the depollution effect of photocatalytic building and construction materials is evident, there are still unresolved problems when these materials are used in real-life applications. The photocatalyst is able to degrade only pollutants which are absorbed on the surface of the construction materials. In widely open spaces, the pollutant removal efficiency may be low as only a small fraction of the pollutants can be trapped. For this reason the applicability of photocatalytic construction materials in outdoor environments is restricted to confined spaces and street canyons where, due to low pollutants dispersion and poor ventilation, the degradation of hazardous substances is significant¹⁰⁶.

Other limitations can derive from the nature of the cementitious support which the photocatalyst is immobilised on. Rachel et al.¹⁰⁷ showed that TiO₂/cement mixtures and red bricks containing TiO₂ were significantly less efficient than TiO₂ slurries in decomposing 3-nitrobenzenesulfonic. It is thought that the reduction of active surface and the presence of ionic species, which could contribute to charge recombination in the activated photocatalyst, are the reasons for the catalytic activity loss. Lackhoff et al.¹⁰⁸ indicated that the photocatalytic activity of TiO₂-containing cement can be reduced over

several months due to carbonation of cement. The change in the cement surface microstructure followed by carbonation seems to be the main cause of the related photoactivity drop. The Hong Kong Environmental Protection Department claimed in a report that the photocatalytic activity of TiO_2 coated paving blocks decreased significantly after 4 month exposure in a city centre area due to the accumulation of contaminants on the block surface ¹⁰⁹. This could imply that periodic servicing and washing the paving blocks might be necessary to maintain the air pollution remediation properties. Finally, as far as indoor applications are concerned, controversy surrounds the question of whether it is safe to apply the photocatalytic materials in closed environments. The main issues remain the possible health effect of by-products formed by incomplete photo-oxidation ¹¹⁰ as well as the potential influence on human health of nanosized particles released from the photocatalytic material surface.

1.4. Aims and Objectives of the Thesis

In the literature review presented in the previous section, a general overview of the photocatalytic action and related performances of TiO₂-containing cements for self-cleaning and air pollution mitigation purposes has been presented and described. This is considered the state of the art of the present PhD project. The work conducted during this PhD program aims to address a series of key questions yet unanswered in the state of the art presented above, namely:

- i. Insights into reaction mechanisms of self-cleaning processes provided by photocatalytic cementitious surfaces;
- ii. Analogies and differences amongst photocatalytic reaction mechanisms responsible for self-cleaning effect when comparing pure TiO₂ and TiO₂ included into cementitious composites;
- iii. Influence of TiO₂ surface hydration on the oxidation of nitrogen oxides for pure TiO₂ and TiO₂ contained in cementitious products;
- iv. General influence of the cement environment, i.e. high pH, high ionic strengths, presence of highly polarising and non-indifferent electrolytes, on the electrokinetic properties of TiO₂ nanoparticles and ultimately on the overall photocatalytic performances.

The experimental work and related discussion presented in this PhD thesis will develop our understanding of the fundamental chemistry of TiO₂ photocatalysis as applied to cementitious materials in order to address those key questions highlighted above. In particular, points i. and ii. will be answered by analysing the mechanism of Rhodamine B degradation on the surface of TiO₂-containing cements and comparing the results with similar systems using unsupported TiO₂, under similar irradiation conditions. Point iii. will be addressed by investigating the state of the water on untreated and thermally treated TiO₂ surfaces through IR spectroscopic techniques. Subsequently performances in oxidising NO_x will be linked to the TiO₂ surface hydration. Finally, point iv. will be addressed by investigating ζ -potentials, surface charge densities, primary and secondary particle size of TiO₂ particles in ionic environments modelling the conditions achieved in

real cementitious specimens. These experimental data will then be used to interpret the different performances of two different TiO_2 samples (one nanosized and one micro-sized) in oxidising Rhodamine B and nitrogen oxides.

In relation to point iv., this work will also try to provide details about methodologies to drive optimal deposition and dispersion effectiveness of the photoactive TiO_2 in cement, in order to achieve higher photocatalytic performances. This represents an important set of data and guidelines useful for manufacturers and end users.

References

1. A. Fujishima and K. Honda, *Nature*, 1972, **238**, 37-38.
2. M. R. Hoffmann, S. T. Martin, W. Choi and D. W. Bahnemann, *Chem. Rev.*, 1995, **95**, 69-96.
3. C. Kormann, D. W. Bahnemann and M. R. Hoffmann, *Environ. Sci. Tech.*, 1991, **25**, 494-500.
4. A. Mills and S. Le Hunte, *J. Photochem. Photobiol. A*, 1997, **108**, 1 - 35.
5. D. Ollis and H. Al-Ekabi, *Photocatalytic purification and treatment of water and air*, Elsevier, New York, 1993.
6. *Pilkington Active*, WO Pat., 1998.
7. TX Actice Applications - pavements (Italcementi Group), http://www.italcementi.it/ITA/Prodotti+servizi+e+qualita/Prodotti+Fotocatalitici/Realizzazioni/Gallerie_Realizzazioni/Pavimentazioni.htm.
8. A. Beeldens, in *International RILEM Symposium on Photocatalysis, Environment and Construction Materials*, eds. L. Cassar and P. Baglioni, RILEM, Florence, 2007, vol. 1, pp. 187-194.
9. L. Cassar, A. Beeldens, N. Pimpinelli and G. L. Guerrini, in *International RILEM Symposium on Photocatalysis, Environment and Construction Materials*, eds. L. Cassar and P. Baglioni, RILEM, Florence, 2007, vol. 1, pp. 131-145.
10. R. Cucitore, S. Cangiano and L. Cassar, *High durability photocatalytic paving for reducing urban polluting agent*, WO/2006/000565, 2006.
11. Y. Murata, H. Tawara, H. Obata and K. Murata, *NOX-cleaning paving block*, EP0786283, 2003.
12. H. F. W. Taylor, *Cement chemistry*, 2 edn., Thomas Telford Publishing, London, 1997.
13. G. C. Bye, *Portland cement*, 2 edn., Thomas Telford Publishing, London, 1999.
14. G. J. Verbeck, *Cement hydration reactions at early ages*, Portland Cement Association, Research and Development Laboratories.
15. A. Fujishima, K. Hashimoto and T. Watanabe, *TiO₂ Photocatalysis: Fundamentals and Application*, 1 edn., BKC, Tokyo, 1999.
16. H. Irie, S. P. Tee, T. Shibata and K. Hashimoto, *Electrochem. Solid-State Lett.*, 2005, **8**, 23-25.
17. R. Wang, K. Hashimoto, A. Fujishima, M. Chikuni, E. Kojima, K. Kitamura, M. Shimohigoshi and T. Watanabe, *Nature*, 1997, **338**, 431-432.
18. D. Rimmer, K. D. Sanderson and T. Paul, *Coated glass*, *United States Pat.*, WO/2004/108619, 2010.
19. G. L. Guerrini, A. Plassais, C. Pepe and L. Cassar, in *International RILEM Symposium on Photocatalysis, Environment and Construction Materials*, eds. L. Cassar and P. Baglioni, RILEM, Florence, 2007, vol. 1, pp. 219-226.
20. J. Singleton, *Band theory and electronic properties of solids*, 1 edn., Oxford University Press Inc., New York, 2001.
21. N. W. Ashcroft and N. D. Mermin, *Solid state physics*, 1 edn., Harcourt Inc., Orlando, 1976.
22. C. Kittel, *Introduction to solid state physics*, 7 edn., John Wiley & Sons, New York, 1996.
23. Bandstructure Lab, <http://nanohub.org>.
24. A. Fujishima, T. N. Rao and D. A. Tryk, *J. Photochem. Photobiol. C*, 2000, **1**, 1-21.
25. F. Chen, J. Zhao and H. Hidaka, *Intern. J. Photoenergy*, 2003, **5**, 209-217.
26. J. Li, W. Ma, P. Lei and J. Zhao, *J. Environ. Sci.*, 2007, **19**, 892-896.

27. N. Daneshvar, D. Salari, A. Niaei, M. H. Rasoulifard and A. R. Khataee, *J. Environ. Sci. Health*, 2005, **40**, 1605-1617.
28. A. Folli, U. H. Jakobsen, G. L. Guerrini and D. E. Macphee, *J. Adv. Oxid. Technol.*, 2009, **12**, 126-133.
29. G. L. Guerrini and E. Peccati, in *International RILEM Symposium on Photocatalysis, Environment and Construction Materials*, eds. L. Cassar and P. Baglioni, RILEM, Florence, 2007, vol. 1, pp. 179-186.
30. M. Kawakami, T. Furumura and H. Tokushige, in *International RILEM Symposium on Photocatalysis, Environment and Construction Materials*, eds. L. Cassar and P. Baglioni, RILEM, Florence, 2007, vol. 1, pp. 163-170.
31. J. Zhao and X. Yang, *Build. Environ.*, 2003, **38**, 645-654.
32. B. P. Nelson, R. Candal, R. M. Corn and M. A. Anderson, *Langmuir*, 2000, **16**, 6094-6101.
33. B. O'Regan and M. Gratzel, *Nature*, 1991, **353**, 737-740.
34. P. Stefanov, M. Shipochka, P. Stefchev, Z. Raicheva, V. Lazarova and L. Spassov, *J. Phys.*, 2008, **100**, 1-4.
35. J. Li, L. Li, L. Zheng, Y. Xian and L. Jin, *Electrochim. Acta*, 2006, **51**, 4942-4949.
36. G. K. Mor, K. Shankar, M. Paulose, O. K. Varghese and C. A. Grimes, *Nano Letters*, 2005, **6**, 215-218.
37. K. Hashimoto, K. Wasada, N. Toukai, H. Kominami and Y. Kera, *J. Photochem. Photobiol. A*, 2000, **136**, 103-109.
38. H. Lin, C. P. Huang, W. Li, C. Ni, S. Ismatshah and Y. Tseng, *Appl. Catal. B-Environ.*, 2006, **68**, 1-11.
39. D. Reyes-Coronado, G. Rodriguez-Gattorno, M. E. Espinosa-Pesqueira, C. Cab, R. De Coss and G. Oskam, *Nanotechnology*, 2008, **19**.
40. S. D. Mo and W. Y. Ching, *Phys. Rev. B*, 1995, **51**, 13023-13032.
41. R. A. Aziz and I. Sopyan, *Indian J. of Chem.*, 2009, **48A**, 951-957.
42. Huntsman_Tioxide_Pigments_Corp., *Manufacture and General properties of titanium dioxide pigments*, Brochure.
43. Y. Masuda and K. Kato, *Cryst. Growth and Design*, 2008, **8**, 3213-3218.
44. H. G. Yang, C. H. Sun, S. Z. Qiao, J. Zou, G. Liu, S. C. Smith, H. M. Cheng and G. Q. Lu, *Nature*, 2008, **453**, 638-642.
45. *Processing of anatase TiO₂ obtained from the chloride process*, United States Pat., 1974.
46. Webmineral data, <http://webmineral.com/data/Ilmenite.shtml>.
47. J. Gambogi, *U.S. Geological Survey*, 2006.
48. *Mössbauer Mineral Handbook*, Mössbauer Effect Data Centre, Asheville (USA), 2005.
49. C. Byun, J. W. Jang, I. T. Kim, K. S. Hong and B. W. Lee, *Mater. Res. Bull.*, 1997, **32**, 431-440.
50. L. E. Depero, P. Bonzi, M. Zocchi, C. Casale and G. De Michele, *J. Mater. Res.*, 1993, **8**, 2709-2715.
51. U. Diebold, *Surf. Sci. Rep.*, 2003, **48**, 53-229.
52. A. Fujishima, X. Zhang and D. A. Tryk, *Surf. Sci. Rep.*, 2008, **63**, 515-582.
53. J. Trimboli, M. Mottern, H. Verweij and P. K. Dutta, *J. Phys. Chem. B*, 2006, **110**, 5647-5654.
54. M. A. Henderson, W. S. Epling, C. H. F. Peden and C. L. Perkins, *J. Phys. Chem. B*, 2002, **107**, 534-545.
55. M. A. Henderson, *Langmuir*, 1996, **12**, 5093-5098.
56. P. Liu, W. Duan, W. Liang and X. Li, *Surf. Interface Anal.*, 2009, **41**, 394-398.
57. X. Fu, W. A. Zeltner and M. A. Anderson, *Stud. Surf. Sci. Catal.*, 1996, **103**, 445.

58. A. Iacomino, G. Cantele, D. Ninno, I. Marri and S. Ossicini, *Phys. Rev. B*, 2008, **78**, 075405.
59. A. V. Delgado, F. Gonzalez-Caballero, R. J. Hunter, L. K. Koopal and J. Lyklema, *Pure Appl. Chem.*, 2005, **77**, 1753–1805.
60. D. J. Shaw, *Introduction to Colloid and Surface Chemistry*, Butterworths, London, 1966.
61. B. V. Derjaguin and L. P. Landau, *Acta Phys. Chim. USSR*, 1941, **14**, 633.
62. E. J. W. Verwey and G. T. J. Overbeek, *Theory and stability of lyophobic colloids*, Elsevier, Amsterdam, 1948.
63. A. Folli, I. Pochard, A. Nonat, U. H. Jakobsen, A. M. Shepherd and D. E. Macphree, *J. Am. Ceram. Soc.*, 2010, **93**, 3360-3369.
64. B. Jönsson, A. Nonat, C. Labbez, B. Cabane and H. Wennerström, *Langmuir*, 2005, **21**, 9211-9221.
65. C. Labbez, B. Jönsson, M. Skarba and M. Borkovec, *Langmuir*, 2009, **25**, 7209-7213.
66. C. Labbez, A. Nonat, I. Pochard and B. Jönsson, *J. Colloid Interf. Sci.*, 2007, **309**, 303-307.
67. H. Van Damme, in *Photocatalysis. Fundamentals and Applications*, eds. N. Serpone and E. Pelizzetti, John Wiley & Sons, New York, 1 edn.
68. E. Rondet, T. Ruiz, M. Deladonde, C. Dupuy and J. P. Desfours, *Int. Journ. Chem. Reactor Eng.*, 2010, **8**.
69. Z. Abbas, C. Labbez, S. Nordholm and E. Ahlberg, *J. Phys. Chem. C*, 2008, **112**, 5715-5723.
70. S. Woislowski, *J. Amer. Chem. Soc.*, 1953, **75**, 5201-5203.
71. S. Devahasdin, C. J. Fan, K. Li and D. H. Chen, *J. Photochem. Photobiol. A*, 2003, **156**, 161–170.
72. A. V. Emeline, V. K. Ryabchuk and N. Serpone, *J. Phys. Chem. B*, 2005, **109**, 18515-18521.
73. N. Serpone, *J. Adv. Oxid. Technol.*, 2007, **10**, 111-115.
74. X. Shen, L. Zhu, G. Liu, H. Yu and H. Tang, *Environ. Sci. Tech.*, 2008, **42**, 1687-1692.
75. Hunter $L^*a^*b^*$ Colour Model,
http://www.labcognition.com/panoramaonlinehelp/englisch/colorimetric_analysis/color_models/cie_1976_l_a_b_color_model.htm.
76. HunterLab, <http://www.hunterlab.com/>.
77. UNI_11259, 2008, 1-6.
78. L. Cassar, *Clean Build Clean Air*, 2004, **29**, 328-331.
79. F. Vallée, B. Ruot, L. Bonafous, L. Guillot, N. Pimpinelli, L. Cassar and E. al., in *RILEM Int. Symp. on environment-conscious materials and systems for sustainable developments*, eds. N. Kashino and Y. Ohama, RILEM, Japan, 2004, pp. 245-345.
80. J. Chen and C. Poon, *Build. Environ.*, 2009, **44**, 1899-1906.
81. F. A. Cotton and G. Wilkinson, *Advanced Inorganic Chemistry*, 5 edn., Wiley-Interscience, USA, 1988.
82. R. M. Harrison, *Pollution: causes, effects and control*, 2 edn., The Royal Society of Chemistry, Cambridge, 1992.
83. D. Elsom, *Atmospheric Pollution*, 1 edn., Basil Blackwell, New York, 1987.
84. J. H. Seinfeld, *Atmospheric chemistry and physics: from air pollution to climate change*, 1 edn., Wiley, New York, 1998.
85. C. A. Latta, *Plant Eng.*, 1998, **52**, 105-112.
86. *Chem. Eng. News*, 2000, **78**, 22.
87. S. K. Gangwal, G. B. Howe, J. J. Spivey, P. L. Silveston, R. R. Hudgins and J. G. Metzinger, *Environ. Prog.*, 1993, **12**, 128.
88. D. H. Chen and K. Li, *Photocatalytic Coating on Road Pavements/Structures for NOx Abatement*, Lamar University, Beaumont, 2007.

89. S. Chen and G. Cao, *Desalination*, 2006, **194**, 127-134.
90. J. S. Dalton, P. A. Janes, N. G. Jones, J. A. Nicholson, K. R. Hallam and G. C. Allen, *Environ. Pollut.*, 2002, **120**, 415-422.
91. H. Ichiura, T. Kitaoka and H. Tanaka, *Chemosphere*, 2003, **51**, 855-860.
92. C. S. Poon and E. Cheung, *Constr. Build. Mater.*, 2006, **21**, 1746-1753.
93. UNI_11247, 2009, 1-11.
94. H. Wang, Z. Wu, W. Zhao and B. Guan, *Chemosphere*, 2007, **66**, 185-190.
95. G. Hüsken, M. Hunger and H. J. H. Brouwers, in *International RILEM Symposium on Photocatalysis, Environment and Construction Materials.*, eds. L. Cassar and P. Baglioni, RILEM, Florence, 2007, pp. 147-154.
96. G. Hüsken, M. Hunger and H. J. H. Brouwers, *Build. Environ.*, 2009, **44**, 2463-2474.
97. M. Hunger, G. Hüsken and H. J. H. Brouwers, *Cem. Conc. Res.*, 2010, **40**, 313-320.
98. A. Strini, S. Cassese and L. Schiavi, *Appl. Catal. B-Environ.*, 2005, **61**, 90-97.
99. K. Demeestere, J. Dewulf, B. De Witte, A. Beeldens and H. Van Langenhove, *Build. Environ.*, 2008, **43**, 406-414.
100. PICADA Project, <http://www.picada-project.com/domino/SitePicada/Picada.nsf?OpenDataBase>.
101. W. Zhu, P. J. M. Bartos and A. Porro, *Mater. Struct.*, 2004, **37**, 649-658.
102. Paving the Road to Clean Urban Air, http://www.eoxolit.com/press/article_01.pdf.
103. Starka Betong Industrier - EcoNox products, <http://www.starka.se/focusmain.asp?focusid=2>.
104. T. Maggos, J. G. Bartzis, M. Liakou and C. Gobin, *J. Hazard. Mater. B*, 2007, **146**, 668-673.
105. H. Ichiura, T. Kitaoka and H. Tanaka, *Chemosphere*, 2003, **50**, 79-83.
106. C. E. Bygott, J. E. Maltby, J. L. Stratton and R. McIntyre, in *International RILEM Symposium on Photocatalysis, Environment and Construction Materials*, eds. L. Cassar and P. Baglioni, RILEM, Florence, 2007, vol. 1, pp. 251-258.
107. A. Rachel, M. Subrahmanyam and P. Boule, *Appl. Catal. B-Environ.*, 2002, **37**, 301-308.
108. M. Lackhoff, X. Prieto, N. Nestle, F. Dehn and R. Niessner, *Appl. Catal. B-Environ.*, 2003, **43**, 205-216.
109. C. M. Yu, *Deactivation and regeneration of environmentally exposed titanium dioxide (TiO₂) based products*, Hong Kong Environmental Protection Department, Hong Kong, 2003.
110. J. Auvinen and L. Wirtanen, *Atmos. Environ.*, 2008, **42**, 4101-4112.

Experimental

2.1. Materials and synthetic methods

Throughout this study two commercially available titanium dioxide samples have been characterised, tested and investigated for their dispersion effectiveness and photocatalytic performances in cement pastes and mortars. Table 2.1 and Table 2.2 group the sample names used, their commercial trade names, the manufacturer, the synthetic process and the main physico-chemical characteristics present in the respective Technical Data Sheets available for the two commercial products ^{1, 2}.

Table 2.1 – Sample identification.

sample name	trade name	manufacturer	synthetic process
m-TiO ₂	Tioxide A-HR	Huntsman Tioxide Corp.	sulphate process
n-TiO ₂	PC-105	Millenium Inorganic Chemicals	sulphate process

The names m-TiO₂ and n-TiO₂ are related to their declared primary particle size (or crystallite size): a particle distribution centred around 170 nm for the Tioxide A-HR ² is identified as *m*- for *micro*sized and a particle distribution centred around 17 nm for the PC-105 ¹ is therefore *n*- for *nan*osized.

Table 2.2 – Physical-chemical properties declared in manufacturer specs.

Sample	TiO ₂ content	surface coating	organic treatment	mean crystal size	specific gravity	Loss at 105 °C
	%			nm	g cm ⁻³	%
m-TiO ₂	99	none	present	170	3.895	0.4
n-TiO ₂	> 95	none	none	17	3.895	–

2.2. Photocatalyst characterisation

2.2.1. Bulk properties

2.2.1.1. Light absorption – U.V.-vis. Diffuse Reflectance

Light absorption measurements were undertaken to derive band-gap information on TiO₂ powders and have been carried out using U.V.-vis diffuse reflectance spectroscopy. This analytical technique is very similar to ordinary U.V.-vis Spectroscopy where reflected light instead of transmitted light is collected, Figure 2.1.

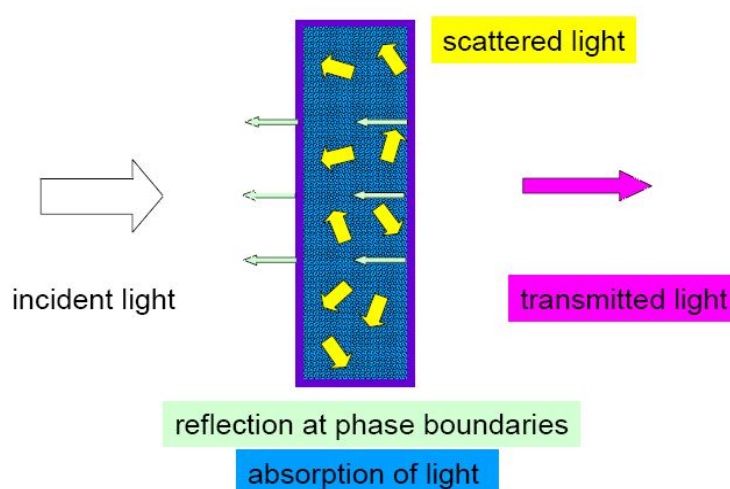


Figure 2.1 – Light absorption – reflection phenomena.

Transmittance, τ , and *absorbance*, A , are defined for ordinary U.V.-vis spectroscopy (liquid media) and are related to each other through the Beer law, equation 2.1:

$$\tau = \frac{I_T}{I_0} = e^{-kcl} = 1 - \alpha \quad (2.1)$$

$$A_e = -\ln \tau = kcl \quad (2.2)$$

$$A_{10} = -\text{Log} \tau = \varepsilon_\lambda cl \quad (2.3)$$

where I_0 is the intensity of incident light, I_T the intensity of transmitted light, α the fraction of light not transmitted (in the most general case sum of light scattered, reflected and absorbed), k and ε_λ the molar extinction coefficients (depending on the base of the logarithm used, $\varepsilon_\lambda = k/2.303$), c the concentration of the absorbing species and l the optical path (length of the

cuvette in case of measurements on liquid media)³. These functions are not longer applicable for diffuse reflectance spectroscopy (solid media) for which other parameters must be defined. Analogous to transmittance for liquids, *reflectance*, R , is an useful parameter to quantify the amount of light reflected by a solid surface, equation 2.4:

$$R = \frac{I_R}{I_0} \quad (2.4)$$

where I_0 is the intensity of incident light, I_R the intensity of reflected light. A correspondent measurement for light absorption can be defined through a parameter called the *Kubelka – Munk function*⁴, analogous to absorbance for liquids, equation 2.5:

$$f(R) = \frac{(1 - R)^2}{2R} = \frac{k}{s} \quad (2.5)$$

where k is an absorption coefficient (as in equation 2.1) and s is a scattering coefficient. Equation 2.5, known as Kubelka – Munk law for solids corresponds to the Beer-Lambert law for liquids.

The spectrometer used was a StellarNet EPP2000 portable spectrometer interfaced to a personal computer through a USB connection and operating through an fibre optic probe as shown in Figure 2.2. The light source is a D₂ lamp with an emission spectrum in the range 200 nm – 700 nm. Light emitted by the lamp is conveyed through the optical fibre cable to the probe which irradiates the powder sample. The latter is in the form of a smooth surface arranged on the sample holder as indicated on the right section of Figure 2.2. The reflected light is then recollected by the same probe and through a series of other optical fibres contained in the same cable, conveyed to the detector inside the spectrometer box. Calibration has been carried out setting the base line (0 % reflectance) by unplugging the cable from the spectrometer end and covering the aperture with a black rubber cap; the top line (100 % reflectance) is set by using a BaSO₄ powder which does not absorb light in the domain of wavelength examined (200 nm – 700 nm). After the calibration TiO₂ powders were arranged as flat and smooth surfaces on the sample holder and relative spectra collected. For each sample three different spectra were collected to have a statistical representation of the band gap comprising a mean value and a standard deviation.

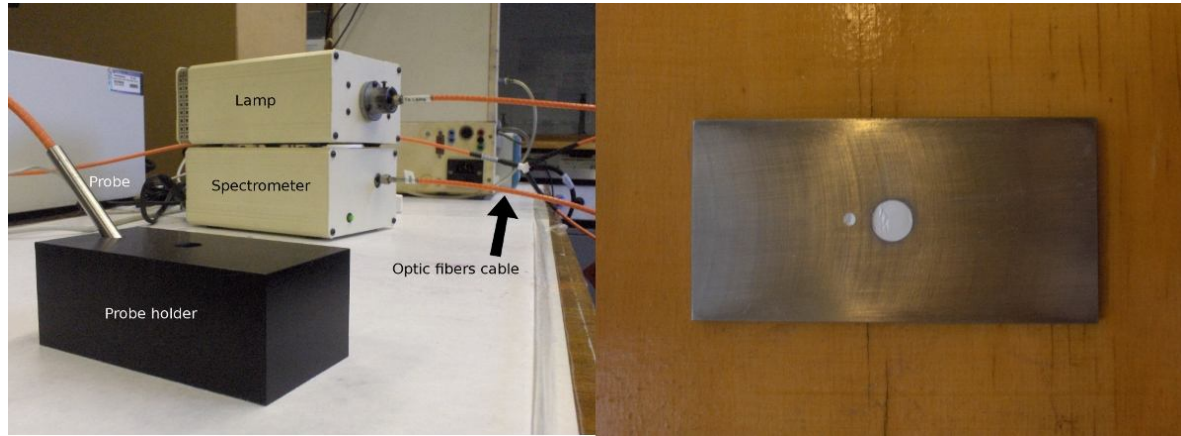


Figure 2.2 – StellarNet EPP2000 Diffuse Reflectance U.V.-vis spectrometer.

Spectra were processed according to the *Kubelka – Munk transform* approach for indirect semiconductors as described in ⁵. The raw data generating the reflectance spectrum were first transformed to Kubelka – Munk function values according to equation 2.5, then Kubelka-Munk function values were reprocessed to obtain the Kubelka – Munk transform (2.6) which has been plotted against incident radiation energy (derived from wavelength according to Planck equation (2.7)).

$$\hat{f}(R_{\infty}) = \sqrt{f(R_{\infty})h\frac{c}{\lambda}} \quad (2.6)$$

$$E = h\frac{c}{\lambda} \quad (2.7)$$

In equations (2.6) and (2.7), $\hat{f}(R_{\infty})$ is the Kubelka – Munk transform, h the Planck constant equal to $6.626 \cdot 10^{-34}$ J·s, c the speed of light in a vacuum equal to $3 \cdot 10^8$ m·s⁻¹ and λ the wavelength of the radiation. In the $\hat{f}(R_{\infty})$ versus E diagram, the band gap has been derived by extrapolation in the energy domain of the linear portion of the plot ⁵ (see section 3.1.1.1.).

2.2.1.2. Crystallinity and Polymorphism – X-Ray Diffraction

X-Ray Diffraction has been used to identify mineralogy and crystallinity of the samples studied. X-rays interacting with matter are generally scattered by electrons in atoms. If the atoms or molecules are organized in a well defined regular array (i.e., the matter is crystalline) and the distances between the atoms are of the same magnitude as the wavelength

of the X-rays, constructive and destructive interference will occur according to the Bragg's law, equation 2.8.

$$n\lambda = 2d \sin \theta \quad (2.8)$$

As a result, diffracted X-rays are emitted at characteristic angles based on the spaces between the atoms organized in crystalline structures called planes occurs ^{6, 7}, Figure 2.3. In equation 2.8 and in Figure 2.3, n is an integer number, λ is the wavelength of the X-rays, d is the distance between planes in the crystal lattice and θ is the angle between the incident ray and the scattering planes.

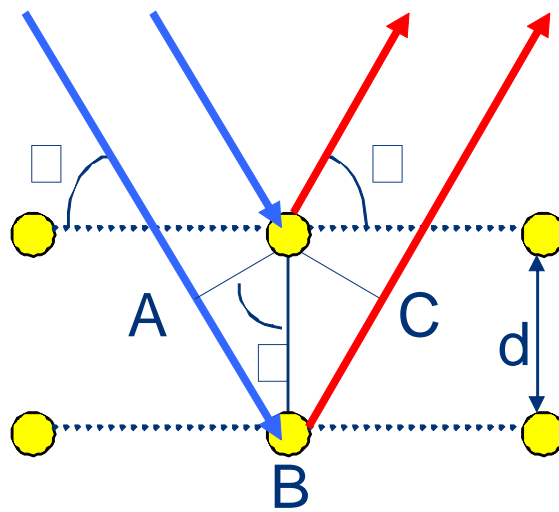


Figure 2.3 – X-ray diffraction in a crystal.

Plotting the intensity of the radiations produced by interference of diffracted X-rays as a function of diffraction angle, provides a pattern characteristic of the crystal structure.

Patterns for the TiO_2 samples here tested have been obtained using a Bruker D8 Advance diffractometer equipped with a $\text{CuK}\alpha 1$ 1.54 \AA X-Ray source, Figure 2.4, operating at room temperature. Phase identification has been carried out with a Bruker database ⁸ provided with the diffractometer and confirmed by computer simulation ⁹. Determination of *FWHM* (**F**ull **W**idth at **H**alf **M**aximum) for the main anatase peak has been also carried out to determine the primary particle size (crystallite size) through the Scherrer equation, as further described in section 2.2.1.4.



Figure 2.4 – Bruker D8 Advance diffractometer.

2.2.1.3. Thermokinetics of TiO₂ surface dehydration – Thermogravimetry, Differential Thermal Analysis and Diffuse Reflectance Infrared Fourier Transform Spectroscopy

The degree of surface hydration (surface Ti-OH groups) and possible phase transitions have been investigated by thermal analysis using a Stanton STA 780 thermal analyser, Figure 2.5, interfaced with a personal computer through a Pico Data Collector and Pico Data Recorder software. The sample holder (small round Pt crucible) was loaded with about 30 mg of TiO₂ powder and set on the thermal balance opposite a similar platinum crucible containing calcined BaSO₄ as inert thermal reference. Both sample and reference are located within the furnace. Two small thermocouples, positioned in proximity of the sample and the reference measured their actual temperatures. Samples experienced a thermal profile from 25 °C·min⁻¹ till 1000 °C·min⁻¹ with a heating rate of 5 °C·min⁻¹. All the thermal analyses have been carried out in N₂ atmosphere.

Thermo – Gravimetry, *TG*, plots have been obtained reporting the weight change (as a percentage of the initial weight at 25 °C) versus temperature. Raw data have been further processed to derive the weight percent variation (first derivative analysis, *DTG*) to better identify the occurrence of thermal phenomena in the temperature domain.



Figure 2.5 – Stanton STA 780 vertical thermo balance analyser.

Differential Thermal Analysis, *DTA*, has been performed plotting the temperature difference between the sample and the reference versus the temperature domain scanned and used to identify the exo – or endo – thermic character of the thermal phenomena identified in the DTG plots.

Diffuse Reflectance Infrared Fourier Transform (DRIFT) spectra have been collected over the temperature range 25 °C – 500 °C (heating rate 5.0 °C min⁻¹) using a Perkin Elmer Spectrum 100 with a diffuse reflectance cell equipped with an electrical heating system (Figure 2.6). Spectra were processed using the associated software.

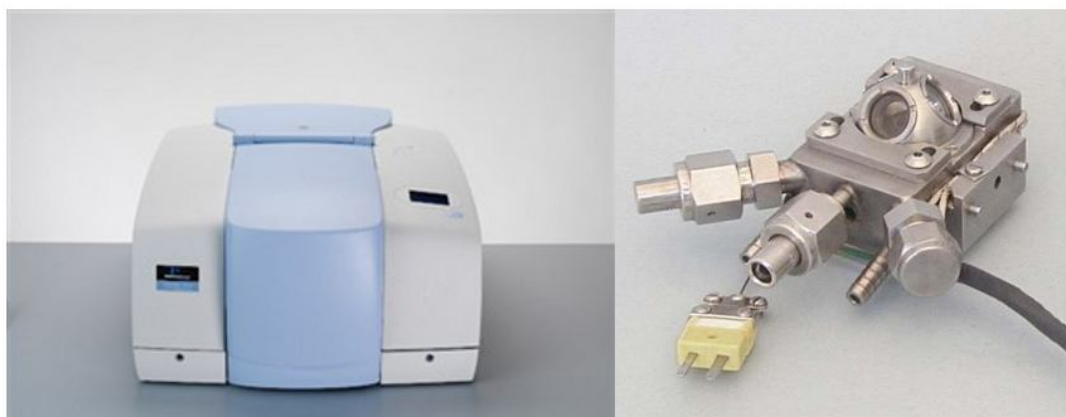


Figure 2.6 – DRIFT Spectrometer and cell.

2.2.1.4. Particle size and morphology - Transmission Electron Microscope imaging

A JEOL Jem 2000 ex Transmission Electron Microscope, Figure 2.7, has been used to evaluate particle size and particle morphology for both the TiO₂ samples investigated here. TEM micrographs have enabled a simple visual image analysis, comprising the examination of more than hundred particles for each sample, to be carried out to determine average particle size and size distribution.

Particle size evaluation has been further developed and improved by comparison between TEM data and results obtained from XRD patterns using the Scherrer equation:

$$d = \frac{0.9\lambda}{FWHM \cos\theta_p} \quad (2.9)$$

where λ is the X-ray wavelength equal to 1.54 Å, FWHM the Full Width at Half Maximum (Anatase 101 peak), θ_p the Bragg's diffraction angle (Anatase 101 peak) and d the average particle diameter. For a complete discussion about the derivation of the Scherrer equation refer to relevant literature^{6,7}.



Figure 2.7 – JEOL Jem 2000 ex Transmission Electron Microscope.

2.2.2. Surface properties

2.2.2.1. *Specific surface area and Inter-particle porosity – N₂ adsorption (B.E.T. and B.J.H. models)*

Specific surface area data have been collected by N₂ physisorption at 77 K using a Micromeritics ASAP 2020 instruments shown in Figure 2.8. Prior to nitrogen adsorption measurements, samples have been degassed at 150 °C for 10 hours in vacuum in order to clean the surface and remove adsorbed water and other adsorbed species. Once degassed, the sample was set in a dewar containing liquid nitrogen to reach the temperature of 77 K and nitrogen adsorption started, scanning a relative pressure range P/P_0 from 0 to 1. The relative pressure P/P_0 is defined as the absolute pressure of nitrogen inside the adsorption chamber divided by the vapour pressure of nitrogen at 77 K. A subsequent nitrogen desorption profile was also carried out, decreasing the relative pressure from 1 to 0. The analysis time for both adsorption and desorption isotherms was 24 hours in total.



Figure 2.8 – Micromeritics ASAP 2020.

Specific surface area data have been derived from N₂ adsorption/desorption isotherms (volume of N₂ adsorbed versus P/P_0) using the B.E.T. model. According to the model proposed by Brunauer, Emmett and Teller¹⁰, the linear trend in the N₂ isotherm (relative pressure between 0.1 and 0.4), which represents the coverage of the first monolayer on the

solid substrate, can be readjust by plotting $\frac{\frac{P}{P_0}}{v\left(1 - \frac{P}{P_0}\right)}$ versus $\frac{P}{P_0}$. The new trend, still linear,

can be interpolated with the B.E.T. equation:

$$\frac{\frac{P}{P_0}}{v\left(1 - \frac{P}{P_0}\right)} = \frac{1}{cv_m} + \frac{c-1}{cv_m} \frac{P}{P_0} \quad (2.10)$$

Where v is the *specific* volume of N_2 adsorbed, v_m the specific volume of N_2 adsorbed when the first monolayer on the solid surface is complete and c a constant measuring the relative strengths of adsorption and condensation¹⁰ and derived as:

$$c = \frac{e^{\frac{\Delta H_{ads}}{RT}}}{e^{\frac{\Delta H_{vap}}{RT}}} \quad (2.11)$$

where ΔH_{ads} is the variation of adsorption enthalpy and ΔH_{vap} the variation of vaporisation enthalpy. Once c and v_m are derived (solving a simple two linear equations system with square matrix using the experimental data measured) the specific surface area can be computed by the equation:

$$s = a_m \frac{v_m}{v_{mol}} N_a \quad (2.12)$$

Where a_m is the approximate area of one single N_2 molecule, v_{mol} the N_2 molar volume at 77 K and N_a the Avogadro's number.

The N_2 adsorption isotherms have also been used to identify TiO_2 porosity by applying the model developed by **Barrett, Joyner and Halenda** (*BJH* model). Assuming cylindrical pores and that the amount of adsorbate in equilibrium with the gas phase is retained by the adsorbent by two mechanisms: (a) physical adsorption on the pore walls, (b) capillary condensation in the inner capillary volume, the following relation between total pore volume and volume of adsorbed N_2 can be derived¹¹:

$$v_{ads}\left(\frac{P_k}{P_0}\right) = \sum_{i=1}^k \Delta V_i \left(r_i \leq r_c \left(\frac{P_k}{P_0} \right) \right) + \sum_{i=k+1}^n \Delta S_i t_i \left(r_i > r_c \left(\frac{P_k}{P_0} \right) \right) \quad (2.13)$$

where $v_{ads}\left(\frac{P_k}{P_0}\right)$ is the volume of nitrogen adsorbed at relative pressure $\left(\frac{P_k}{P_0}\right)$, V_i is the volume, S_i the surface area, t_i the thickness of the adsorbed layer, r_i the *apparent* pore radius, all of them referred to the pore i , and $r_c = r_c\left(\frac{P_k}{P_0}\right)$ a critical radius under which there is free condensation in the pore ¹¹. This equation reads: at any relative pressure $\left(\frac{P_k}{P_0}\right)$ (defining a critical radius r_c), the volume of nitrogen adsorbed is the total volume of liquid nitrogen condensed in pores (totally filled up) having radius smaller than r_c plus the total volume of the adsorbed nitrogen film in pores with radius bigger than r_c . r_i is the *apparent* radius because:

$$\forall \ 0 < \left(\frac{P_k}{P_0}\right) < \left(\frac{P_k}{P_0}\right)_{sat} \quad \wedge \quad \forall \ 1 < i < n \quad | \quad r_i = r_{g,i} - t_i \quad (2.14)$$

where $r_{g,i}$ is the geometric radius of the pore i . Using a high number of $\left(\frac{P_k}{P_0}\right)$ investigated, the pore volume distribution can be obtained by plotting the variation of the pore volume in the pore radii, or pore diameters versus the pore radii, or diameters, i.e.: dV/dr_g versus r_g or dV/dD versus D , where of course D is twice r_g .

Moreover, specific surface area data have been used to validate once more particle size results obtained by T.E.M. and X.R.D. using a simple geometrical model:

$$d = \frac{6}{\rho_{TiO_2} S} \quad (2.15)$$

where d is the mean particle diameter, ρ_{TiO_2} the anatase density equal to 3.895 g cm^{-3} (see Table 2.2) and S the B.E.T. specific surface area. Equation 2.15 assumes spherical particles in contact each other through one single point. It is clearly far beyond the reality but due to the very small particle size of the two TiO_2 samples, it can provide good approximations.

2.2.2.2. *Surface composition analysis – X-Ray Photoelectron Spectroscopy and Energy Dispersion Spectroscopy*

Investigations on the chemical nature of the sample surfaces have been carried out by cross analysis using both *XPS* (**X**-ray **P**hotoelectron **S**pectroscopy) and *SEM – EDS* (**S**canning **E**lectron **M**icroscopy – **E**nergy **D**ispersion **S**pectroscopy). This study has been driven by knowledge acquired through the manufacturers' patents about the commercial titanias used¹²⁻¹⁵. The majority of commercial TiO₂s designated for photocatalysis are not coated, nevertheless during manufacture inorganic materials are often added to control crystal growth and/or to modify their surface chemistry (e.g.: electrokinetic properties), as described in section 1.2.6. (precalciner additives). For this reason analyses have been focused on a systematic and selective search for: Na, Al, Si, P, S, C and K (according to patents¹²⁻¹⁵).

X-ray photoelectron spectroscopy (XPS) is a surface analysis technique that is element specific. It uses soft X-ray photons to eject core level electrons from surface atoms, the kinetic energy of which are analysed by a detector. The kinetic energy of each of these photoelectrons is related to the binding energy of the electron in the solid by the equation:

$$E_k = h\nu - E_B \quad (2.16)$$

where E_k is the kinetic energy, $h\nu$ is the incident photon energy and E_B is the binding energy. The binding energy, and therefore the measured kinetic energy, is specific to the surface atom from which it came from. Consequently, specific elements and potential oxidation states can be identified and peak analysis of the resulting spectrum can allow the calculation of elemental ratios and weight loadings¹⁶.

X-ray photoelectron spectra have been obtained with the VG – Escalab X-Ray Photoelectron Spectrometer VGX900 (Al K α radiation) shown in Figure 2.9 on the untreated sample powders. Spectrum lines have been interpreted using the NIST (National Institute of Standards and Technology) database for XPS analysis¹⁷ together with XI – SDP21 Version 2.1 peak fitting software provided with the instrument.



Figure 2.9 – VG – Escalab X-Ray Photoelectron Spectrometer.



Figure 2.10 – FEI Quanta 400 Scanning Electron Microscope.

SEM – EDS micrographs and relative composition analyses have been carried out using a FEI Quanta 400 Scanning Electron Microscope, Figure 2.10, equipped with a Thermo NSS-UPS-SEM-INORAN System SIX for X-ray microanalysis (EDS). Secondary electron images have been collected for the TiO₂ sample powders (no impregnation, no coating, low vacuum mode). EDS spectra have been analysed using the database provided together with the instrument software.

2.2.2.3. *Electrokinetic properties – ζ -potential and surface charge density*

The pH of Zero Charge (PZC) was evaluated by the zero change of pH consecutive to additions of an indifferent electrolyte. Sodium nitrate was used to increase the ionic strength from 10^{-3} to 10^{-2} mol l⁻¹ of 1%w/w TiO₂ suspensions, in the pH range 4 to 10 for n-TiO₂ and 1.7 to 10 for m-TiO₂. Simultaneously, the dynamic mobility and ζ -potential of the particles was measured using a Colloidal Dynamics 7020 ZETAPROBE CAD apparatus (electroacoustic method), see Figure 2.11.



Figure 2.11 – Colloidal Dynamics 7020 Electroacoustic ZetaProbe.

The electroacoustic method is one of the most commonly applied methods to derive ζ -potential of colloidal particles, together with electrophoretic and sedimentation methods. An

alternating electrical field applied between two electrodes in a colloidal suspension induces vibrations of colloidal particles. These vibrations generate ultrasound which can be collected by an ultrasonic receiver (usually inserted in one of the two electrodes). The electric sonic amplitude, esa , is directly related to the particle averaged dynamic mobility through the O'Brien equation ¹⁸:

$$esa = A(\omega)\phi\left(\frac{\rho_s - \rho_{sol}}{\rho_{sol}}\right)\langle\mu_D\rangle Z \quad (2.17)$$

where $A(\omega)$ is an empirical instrument constant dependent on the frequency used, ϕ the volume fraction of the solid in the colloidal suspension, ρ_s and ρ_{sol} the density of the solid and density of the solution respectively, $\langle\mu_D\rangle$ the particle averaged dynamic mobility and Z another empirical instrument constant. Particle averaged dynamic mobility is, of course, ζ -potential dependent:

$$\langle\mu_D\rangle = \frac{2\varepsilon\zeta}{3\eta}G\left(\frac{\omega a^2}{\nu}\right)[1 + f(\lambda, \omega')] \quad (2.18)$$

where ε is the dielectric constant, η and ν the dynamic and kinematic viscosities respectively, ω the frequency of alternating electric field applied, a the average particle radius and ζ the ζ -potential. G and $f(\lambda, \omega')$ are rather complex functions depending on frequency, electrical conductivities near the particle surface and in the bulk of the solution, density of the solid particles ¹⁸. Therefore, measuring the electric sonic amplitude at each pH value and knowing all the other parameters and constants involved, the particle ζ -potential can be derived.

Titration of the surface charge $\sigma_0(\text{pH})$ was made by measurements of the surface consumption of H^+ or OH^- by 252.5 g of 1 % w/w TiO_2 suspension in $10^{-2} \text{ mol l}^{-1} \text{ NaNO}_3$. Besides the suspension titration, the same procedure was applied to an identical volume of supernatant of the suspension. The H^+ or OH^- consumed by the surface at a given pH could be calculated from the difference in the amount of titrant (HCl or NaOH, both analytical grade) required for the supernatant solution and for the suspension to reach this given pH from the PZC. Namely, the total surface excess charge of the particle is computed from the following equation:

$$\sigma_0 = \frac{F}{mS_{BET}} C_T (V_{susp} - V_{super}) \quad (2.19)$$

Where σ_0 is the surface excess charge in $C\ m^{-2}$, m the mass of particles used in g, A the specific surface of the particles in $m^2\ g^{-1}$, F the Faraday constant equal to $96500\ C\ mol^{-1}$, C_T the titrant concentration equal to $1\ mol\ l^{-1}$ for both HCl and NaOH, V_{susp} the titrant volume added at a given pH for the suspension and V_{super} the titrant volume added for the same pH for the supernatant solution.

ζ -potentials were also measured for 1 % w/w TiO_2 suspensions in calcium hydroxide solutions of various concentrations ranging from 0.05 to 16 $mmol\ l^{-1}$. Calcium concentrations in the solutions were determined using a VISTA-PRO VARIAN ICP Optical Emission Spectrometer. The standardisation was carried out with synthesised standards. Each sample was analysed three times. The estimated error on the concentration was about $0.01\ mmol\ l^{-1}$. The choice of Ca^{2+} depends on the fact that cement pore solutions are saturated with $Ca(OH)_2$, hence understanding how the surface chemistry of TiO_2 could be modified by the presence of calcium ions is an important step in understanding dispersion behaviour.

2.2.2.4. *Dispersion effectiveness – sedimentation test*

The two commercial TiO_2 s have been tested in several different ionic environments to test and verify stabilities of their dispersions. The method used has been already described in ¹⁹. 2% m/v dispersions have been prepared for both samples and 10 ml of each suspension used to fill small test tubes. The position of the interface between supernatant and solid particle sediment was recorded at regular time intervals, precisely at 10, 20, 30, 60 min, 1 day and, sometimes, 4 days. Media used for the dispersions were deionised H_2O and solutions of strong acids or bases at pH = 2 and pH = 12.5 respectively, in order to compare results of dispersion stability with ζ -potential values previously derived. The structure of acids and bases used was H_yX_z for acids and $Me_y(OH)_z$ for bases, in order to provide a potential determining ion, H^+ or OH^- , and a counter ion, X^{y-} or Me^{z+} . The counterions were either an indifferent electrolyte (highly hydrated in solution, less interactions with colloidal particles) or a non – indifferent electrolyte (less hydrated in solution, more interactions with colloidal particles). The choices of $X^{y-}\ Me^{z+}$ were: for indifferent electrolytes, Cl^- and Na^+ and for non – indifferent electrolytes, SO_4^{2-} and Ca^{2+} . Solutions used for dispersion preparation were

therefore HCl, NaOH, H₂SO₄ and Ca(OH)₂. Two further dispersions (one for each TiO₂) in KOH at pH = 12.5 were also prepared to investigate the effect of an indifferent electrolyte such as K⁺ but with higher tendency to interact with colloidal particles than Na⁺ (smaller hydrated radius for K⁺ being less polarising than Na⁺, hence lower shielding effect of H₂O molecules in the hydration shell).

The reason behind the choice of the ions above is the fact that they are all present in the pore solution of hardened cement. A final dispersion stability test have been carried out in a synthetic cement pore solution prepared according to the method described in ²⁰, and with composition and pH shown in Table 2.3.

Table 2.3 – Synthetic cement pore solution and pH.

Ca²⁺	Na⁺	K⁺	SO₄²⁻	OH⁻	pH		
<i>mM</i>	<i>mM</i>	<i>mM</i>	<i>mM</i>	<i>mM</i>			
21.2	97.8	180.1	85.9	148.6	12.87	±	0.02

A structural model comprising TiO₂ aggregation/dispersion in real cement structures has been further proposed. Validation of this qualitative model has been carried out by SEM investigations, using a FEI Quanta 400 Scanning Electron Microscope, Figure 2.9, on real cement paste specimens containing either m-TiO₂ or n-TiO₂ and prepared according to the procedure described in section 2.3.1.

2.3. Cement paste and mortar preparation

2.3.1. Cement paste preparation

Two sets of photocatalytic cement pastes were prepared, one for each of the two commercial TiO_2 products. The TiO_2 and fresh white Portland cement (CEM I 52.5 R) powders were dry mixed in the mass ratio 3.5 : 96.5. 20 g of the mixture was subsequently hydrated with 8 g of distilled water (water : cement ratio, w/c = 0.4). A third set (control) was prepared without photocatalyst. The mixing procedure followed recommendations published previously in ²¹ comprising the following route:

- i. Pouring 20 g cement- TiO_2 mixture (20 g of cement for the set of control samples) *in* 8 g of distilled water;
- ii. Stirring at 500 rpm for 3 min;
- iii. Stop stirring for 2 min (making sure there is no unmixed solid on the bottom of the vessel);
- iv. Stirring at 2000 rpm for 2 min.

The mixer used for cement hydration is shown in Figure 2.12.

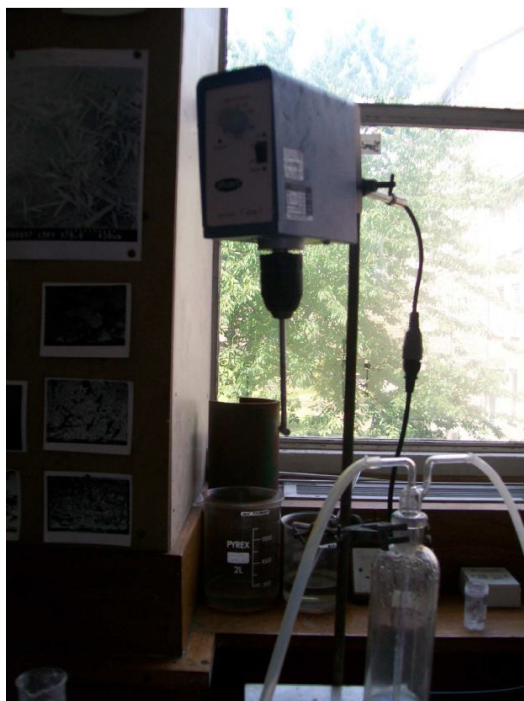


Figure 2.12 – Mixer for cement paste preparation.

After mixing, pastes were cast in 42 mm diameter moulds and let harden for one day at room temperature. Six cement discs were produced for each set.

The same preparation was repeated (two sets of photocatalytic cement pastes containing one m-TiO₂ and the other n-TiO₂ plus a control set without TiO₂) but this time samples were cured for seven days at room temperature in sealed plastic bags and, afterwards, for seven days at room temperature and 60 % of relative humidity. This curing regime is described in an international standard for preparation of cured cement pastes and mortars²².

One day cured and fourteen days cured samples have been evaluated based on Rhodamine B (RhB) discolouration test, Section 2.4.1.

2.3.2. Mortar preparation

The hydraulic binder used for mortar preparation was, a dry mixture of TiO₂ (either m-TiO₂ or n-TiO₂) and fresh white Portland cement (CEM I 52.5 R) in the mass ratio 3.5 : 96.5. In these samples, standard sand was used (DIN EN 196-1 sand). 450 g of the mixture was subsequently hydrated with 225 g of distilled water (water : cement ratio, w/c = 0.5). A third set (control) was prepared without photocatalyst. The mixing procedure used was taken from the European Standard ISO 679²²:

- i. Pouring 450 g cement-TiO₂ mixture (450 g of cement for the set of control samples) in 225 g of distilled water;
- ii. Stirring the paste at speed 1 for 30 s;
- iii. Adding one bag of DIN EN 196-1 sand regularly under stirring for the following 30 s;
- iv. Stirring the obtained mortar at speed 4 for 30 seconds;
- v. Stop stirring for 90 s (making sure there is no unmixed solid on the bottom of the vessel);
- vi. Stirring the mortar at speed 4 for 60 seconds.

The mixer used for mortar preparation is shown in Figure 2.13 and it fulfilled requirements specified in the Standard ISO 679 for the mixing device.

After mixing, mortars were cast in 9 cm diameter x 1 cm thickness plastic Petri dishes and let harden for one day at room temperature. Twelve mortar discs were produced for each set. Samples curing followed, once again, the Standard ISO 679: seven days at room temperature in sealed plastic bags and further seven days at room temperature and 60 % of relative humidity.

Mortars disks have been tested according to the Rhodamine B (RhB) discolouration test, Section 2.4.1 and the NO_x oxidation test (UNI standard 11247-2009 ²³).



Figure 2.13 – Kenwood mixer for mortar preparation.

2.4. Photocatalytic performance

2.4.1. Self-cleaning effect – Rhodamine B (RhB) test

Cement paste samples prepared as described in section 2.3.1. were coated with 20 μl of a 0.5 g/l aqueous rhodamine B solution. The area coated was approximately 1.2 cm^2 , see Figure 2.14, and the samples conditioned for 30 min. The sets cured for one single day were used to evaluate the influence of a different light exposure during the conditioning time. Three of the six discs per set (one set with m-TiO₂, one with n-TiO₂ and one without photocatalyst) were conditioned for 30 minutes under daylight, the remaining three were coated and conditioned for 30 minutes in darkness. All three sets were subsequently irradiated with a UVItec LI-208.m lamp (2 tubes 8W each, main wavelength 312nm). The sets cured for fourteen days were used to evaluate the influence of the cement aging. Three of the six discs per set (one set with m-TiO₂, one with n-TiO₂ and one without photocatalyst) were conditioned for 30 minutes under daylight and irradiated with the same UVItec LI-208.m lamp. In all the experiments the distance between samples and lamp was 10 cm. Reflectance measurements were performed after various illumination times using a StellarNet EPP2000 Spectrometer showed in Figure 2.2.

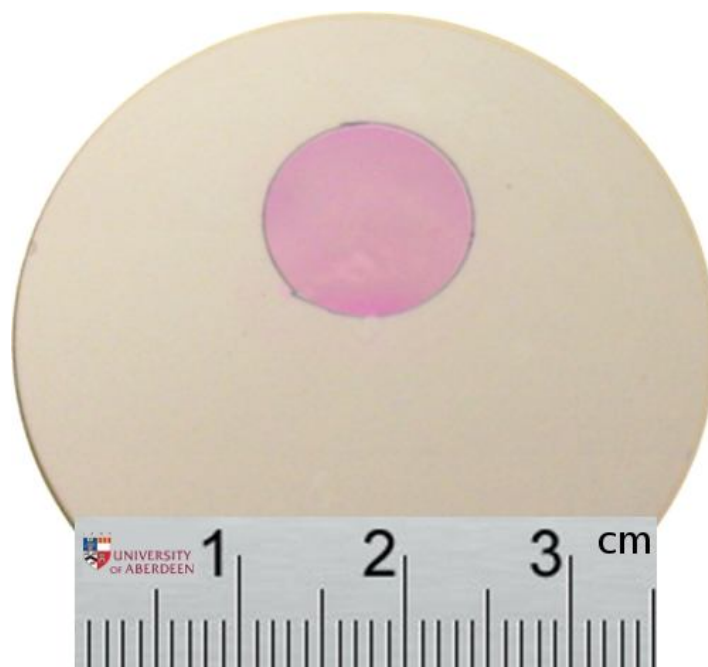


Figure 2.14 – Cement specimen for self – cleaning test.

2.4.2. Depollution – NO_x oxidation test and modelling

2.4.2.1. *NO_x oxidation test with mortar specimens*

NO_x oxidation experiments have been carried out in a continuous fixed bed flow reactor according to the Italian Standard UNI 11247²³. The scheme of the lab plant used is illustrated in Figure 2.15. The photocatalytic reactor consists of a Pyrex glass chamber having a total volume of 3.58 l where the specimen under testing can be located on the bottom part supported by a proper sample holder. The gas inlet tube allows the air/NO_x mixture to flow directly onto the specimen upper surface whilst the gas outlet tube is positioned underneath the sample holder. The system was kept at room temperature: 25 ± 1 °C. U.V. light was provided by an OSRAM ULTRAVITALUX lamp having a main emission in the U.V.-A field distributed around a maximum intensity wavelength of about 365 nm. The lamp – sample distance was set to achieve on the upper sample surface an average irradiance of 20 ± 1 W/m². A schematic diagram of the photocatalytic reactor equipped with the U.V. lamp is illustrated in Figure 2.16. The gas mixture used for the oxidation experiment came from a cylinder containing 40 ppm of NO and 20 ppm of NO₂ in air. Through the other air cylinder and the mass flow meters, the desired flow rates and inlet NO concentration were adjusted. The experiments were carried out at an inlet NO concentration of 500 ppb for a flow rate equal to 3 l min⁻¹, 2 l min⁻¹ and 1.5 l min⁻¹, in order to evaluate the effect of the residence time. All the oxidation experiments have been performed according to the following procedure. The disk sample was wrapped in a sealing film in order to let the upper surface free and protect the side surface. After introducing the disk sample in the photocatalytic reactor the gas stream (at given flow rate) was switched on and the system let to stabilise for half an hour in the dark in order to achieve a constant NO concentration. The U.V. light was then switched on and the NO/NO₂ concentrations monitored for a further 90 minutes.

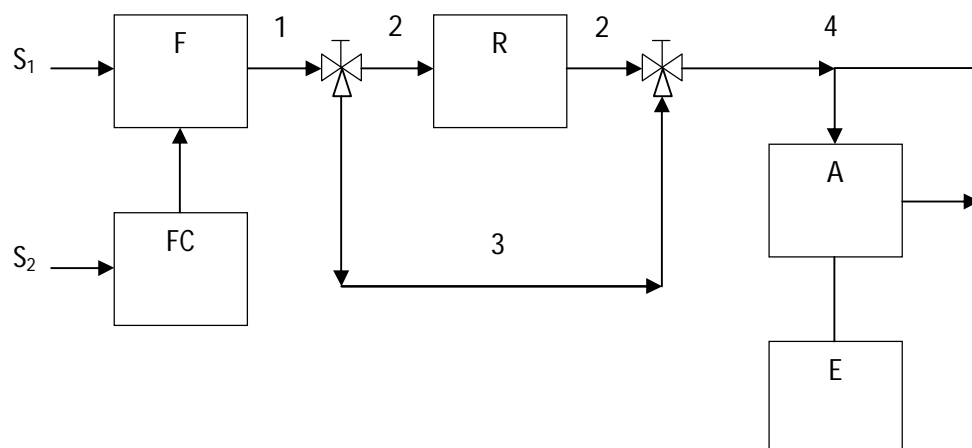


Figure 2.15 – Lab plant flow chart for NO_x oxidation²³. S1 is the NO_x cylinder, S2 the air cylinder, F and FC the mass flow meters for NO and air respectively, R the photocatalytic reactor, A the chemiluminescence analyzer and E the software/computer.

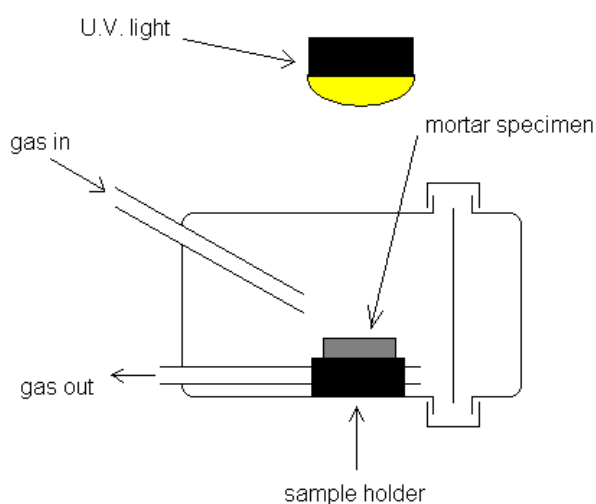


Figure 2.16 – Photocatalytic reactor scheme for NO_x oxidation.

n-TiO₂ has been selected for a further study in order to identify the role of surface water in the photocatalytic oxidation of NO and investigate the different reaction regimes as well as the possible deactivation phenomena. The pure photocatalyst has been deposited on the surface of glass beads and tested in a photocatalytic powder layer reactor.

2.4.2.2. *n-TiO₂ coated glass beads preparation*

Glass beads (Sigma – Aldrich; diameter 450 – 600 μm) were coated with n-TiO₂ by the method of Daneshvar²⁴. 3 g of n-TiO₂ were dispersed in 200 ml of deionised water and

sonicated in an ultrasonic bath for 15 minutes to achieve good dispersion of titania particles. 30 g of glass beads (without any pre-treatment) have been added to the dispersion and left to stand for a further 15 minutes under sonication. The beads were then filtered on a Buchner filter, placed in oven at 106 °C for 3 hours and when dry, fired at 500 °C for 1 hour. After firing the coated beads were placed in a column fitted with a porous disc, washed by flushing 200 ml of deionised water, placed again on a Buchner filter and washed with an excess of deionised water. The final step consisted in a further drying at 106 °C for 30 minutes. Once dry, the n-TiO₂ coated glass beads were stored in a light-tight jar at room temperature in ordinary air conditions. The amount of n-TiO₂ deposited was $0.11 \text{ g}_{\text{TiO}_2} \text{ g}_{\text{glassbeads}}^{-1}$. B.E.T. specific surface area of coated glass beads has been previously measured by N₂ adsorption using a Micromeritics ASAP 2020, see Figure 2.8. SEM micrographs of coated glass beads have been obtained using a Hitachi S – 520 Scanning Electron Microscope.

2.4.2.3. *NO oxidation test with n-TiO₂ coated glass beads*

The apparatus for the photocatalytic study is shown in Figure 2.17. A dry 250 ppm NO in nitrogen gas stream was blended with dry air in a gas blender until the appropriate NO concentration was obtained. The gas mixture, at a given flow rate, was used to feed the photocatalytic reactor, see Figure 2.18. The latter consisted in a 2 cm diameter glass tube equipped with a water jacket for temperature controlling, a porous sintered glass disk to allocate the n-TiO₂ coated glass beads and a quartz window at the top to irradiate the photocatalytic bed. An OSRAM Ultravitalux U.V.A lamp was used to illuminate the photocatalytic bed in the reactor through the quartz window at the top of the reactor. The distance between lamp and photocatalytic bed was set in order to achieve a constant irradiance of $25 \pm 1 \text{ mW m}^{-2}$ at the catalyst surface. The outlet gas stream was conveyed to a Thermo Environmental 42C chemiluminescence NO–NO₂–NO_x gas analyzer. A constant temperature of $26.8 \pm 0.14 \text{ °C}$ was maintained using a water bath circulating water through the external jacket of the reactor.

To address different levels of adsorbed water, photocatalytic oxidation of NO was monitored using beads as prepared (GB20) and beads having undergone further thermal treatment at 110 and 500 °C for 1 hour (GB110 and GB500 respectively) before introduction in the reactor. In addition, two *blank* tests were carried out to evaluate the contribution of non-photocatalytic

oxidation promoted by U.V. light and the potential reaction of the acidic NO with water adsorbed on the catalyst surface without any irradiation. The first was achieved by introducing the NO/air gas stream in the reactor equipped with TiO₂-free glass beads and the second by leaving the gas stream flowing for about 1 hour in the reactor with n-TiO₂ coated glass beads in complete darkness.

Pseudo steady state conversions for n-TiO₂ coated glass beads have also been studied at two different gas flow rates, 50 ml min⁻¹ and 100 ml min⁻¹, and two different initial NO concentrations, 50 ppm and 25 ppm, to derive kinetic constant and NO adsorption coefficient for the assumed Langmuir – Hinshelwood (L–H) kinetics.

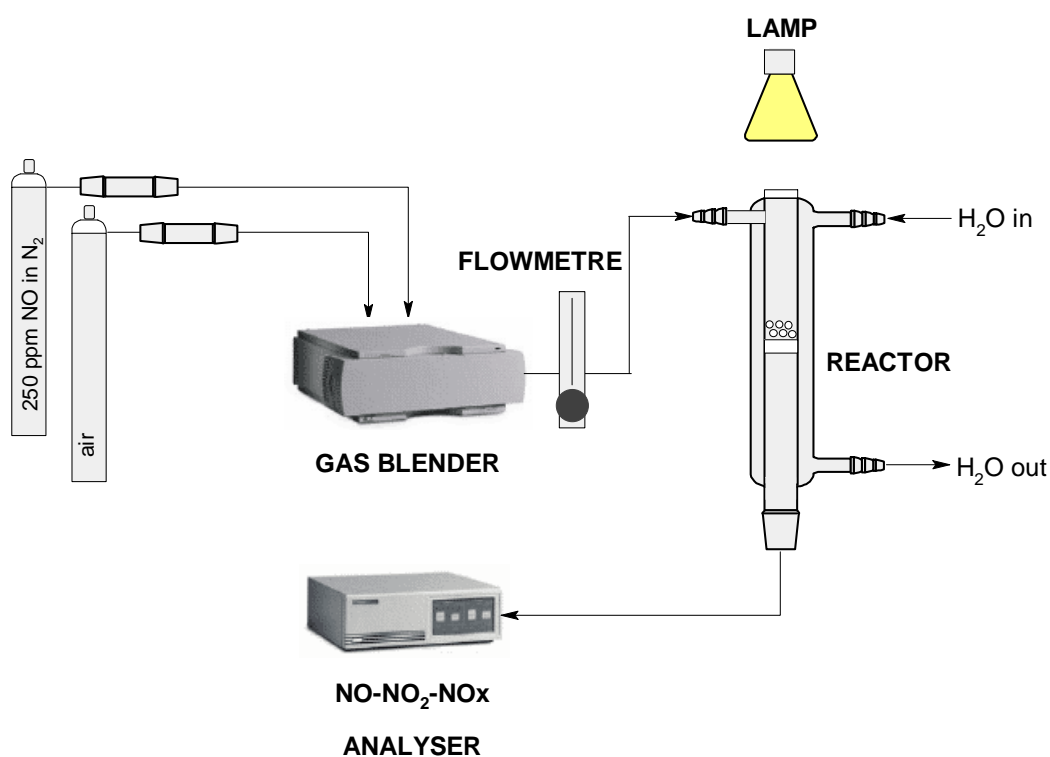


Figure 2.17 – NO oxidation lab plant for n-TiO₂ coated glass beads.

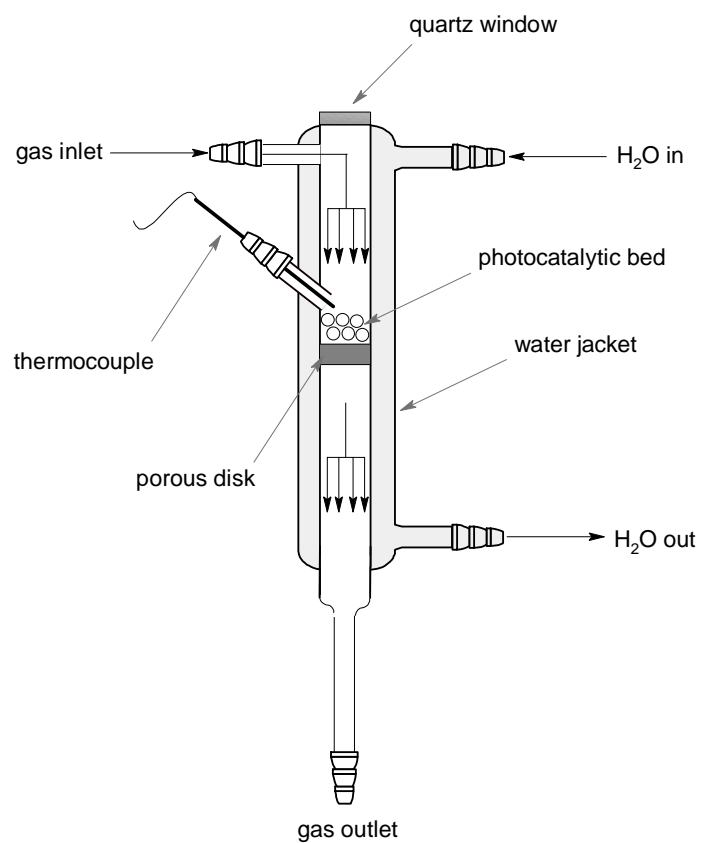


Figure 2.18 – Photocatalytic continuous fixed bed reactor for n-TiO₂ coated glass beads.

2.5. Pilot test

2.5.1. Surface texture and surface microstructure design and engineering

A practical implementation in cement/mortar systems has been carried out in order to identify the influence of surface roughness on the overall self-cleaning performance of big mortar samples, 35 cm x 25 cm x 7 cm, to be tested according to the *accelerated aesthetic ageing method* described in section 2.5.2. Several surfaces were tested and engineered on small cement disks with a diameter of 42 mm and two selected surfaces, a P 320 SiC paper and a *Zemdrain*TM casting membrane, used for the further scale up to prepare the bigger mortars for the accelerated weathering test. The selected surfaces, used to cast mortars on, enable to achieve a similar degree of roughness but the final surface microstructure can be very different. Figure 2.19 shows schematically how these two surfaces work.

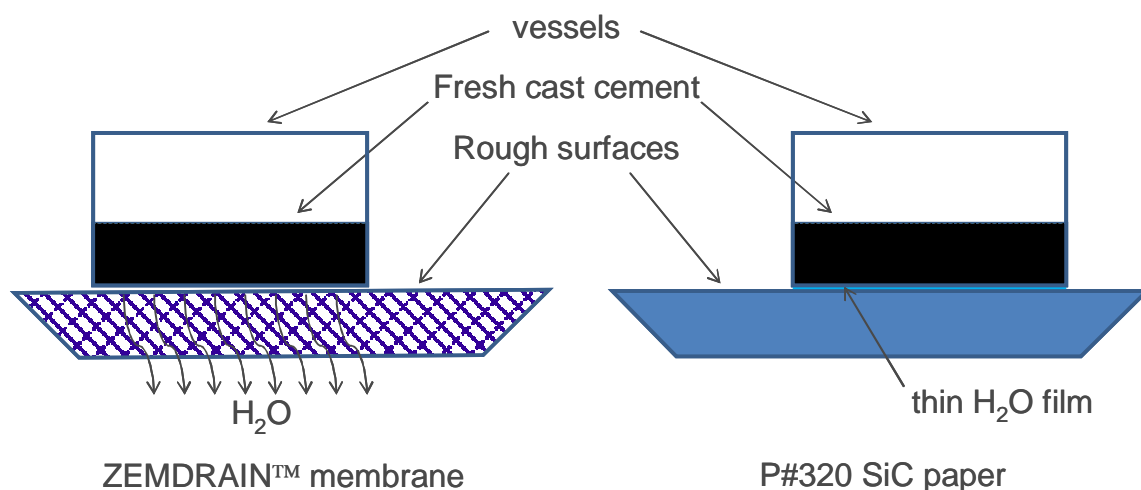


Figure 2.19 – P 320 SiC and ZemdrainTM membrane casting.

ZemdrainTM membrane is able to drain water off the front casting surface during the first day of curing after casting, decreasing the w/c of the surface. Contrary, with the rough SiC paper water is trapped between the forming cement (or mortar surface) and paper itself, leading to a higher w/c ratio on the specimen surface. A further smooth and flat surface was prepared for comparison.

SEM micrographs, using a FEI Quanta 400 Scanning Electron Microscope, Figure 2.10, have been taken for each surface to identify the degree of roughness obtained.

2.5.2. Aesthetic durability – Accelerated Aesthetic Ageing test

Mortar samples for the accelerated aesthetic ageing test have been prepared according to the procedure described in the European Standard ISO 679 ²² and already described in section 2.3.2. The w/c used was 0.4. For each TiO₂ sample, a set of three mortars with different casting surfaces were prepared: one flat and smooth, one with Zemdrain membrane and one with SiC paper. A further set without photocatalyst was prepared as control. In order to minimise the amount of TiO₂ used, mortars were cast in the 35 cm x 25 cm x 7 cm till a thickness of 4 cm and, once hardened (after 1 day), a back-casting with concrete was placed in order to reach the final thickness of 7 cm. The high distance of the mortar – concrete interface, 4 cm from the front casting surface allowed neglecting any “junction” effect of the mortar – concrete interface on the front casting surface itself. Two further sets of three mortars (one for each surface) with no photocatalyst were prepared. On the front casting surface of these specimens, TiO₂ was subsequently sprayed using 20 ml of a 1 % w/v suspension of TiO₂ in ethanol. One set was sprayed with m-TiO₂ and the other with n-TiO₂. Before introduction in the carousel for the exposure test, specimens were cured at 20 ± 0.5 °C and 55 ± 5 % of relative humidity for 28 days.

The accelerated aesthetic ageing device (3AD) and description of each sub-cycle are shown in detail in Figure 2.20 ²⁵. Ageing is accelerated by means of erosion and soiling. The eventual growth of organisms is stimulated but not accelerated. The method exposes mortars to erosion and soiling using dust particles and water, freeze/thaw sub-cycles, wetting/drying sub-cycles and U.V. exposure. The device consists of a central sample holder robot that cyclically places samples inside one of the four exposure chambers. A whole cycle is about one day long, divided in four sub-cycles, each about 6 hours long ²⁵. Mortar specimens have been exposed for a total of 93 cycles corresponding to an equivalent ageing of 5 years in real conditions typical of North Denmark climate (the carousel is indeed property of Aalborg Portland Cement, partner of this PhD project and it has been calibrated according to the climate conditions of the city of Aalborg, North Jutland, Denmark).

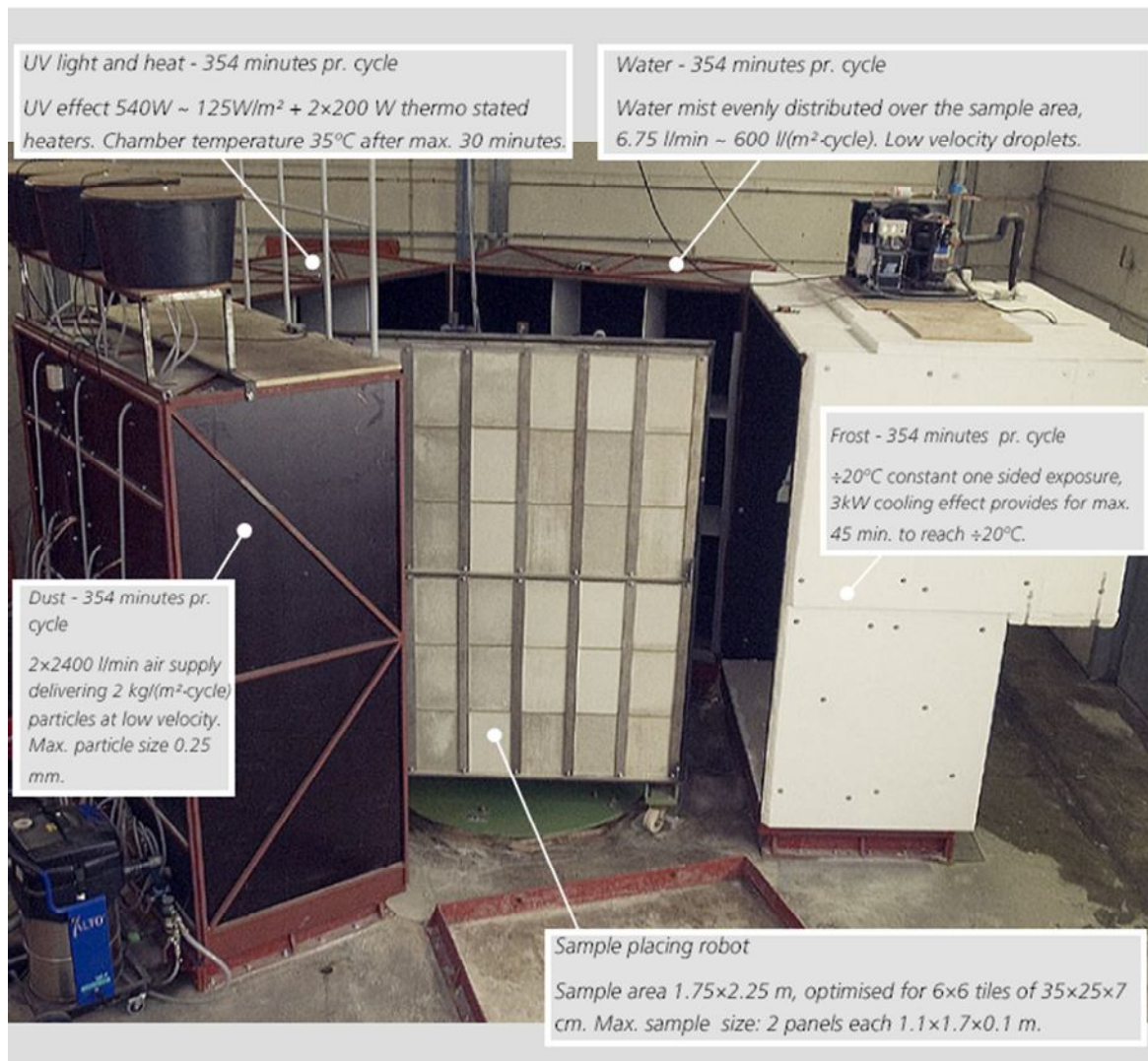


Figure 2.20 – Accelerated aesthetic ageing device (3AD) and relative sub-cycles.

The aesthetic durability of the specimens studied with the 3AD device was monitored by colour measurements using the *CIE L**, *a**, *b** colour model (1976) based on the evolution of the older *Hunter L*, *a*, *b* colour model (1958) ²⁶. The *CIE L**, *a**, *b** colour space is a 3-D polar (the Hunter's was rectangular) colour space based on the opponent – colours theory ²⁶, ²⁷, Figure 2.21. The intensity of the reflected light from the surface passes through three colour filters and is converted into electrical signals, the so-called *tristimulus* colour values: *L**, *a**, *b**:

- i. *L** (lightness) axis – 0 is black, 100 is white;
- ii. *a** (red-green) axis – positive values are red, negative values are green and 0 is neutral;

- iii. b^* (blue-yellow) axis – positive values are yellow, negative values are blue and 0 is neutral;

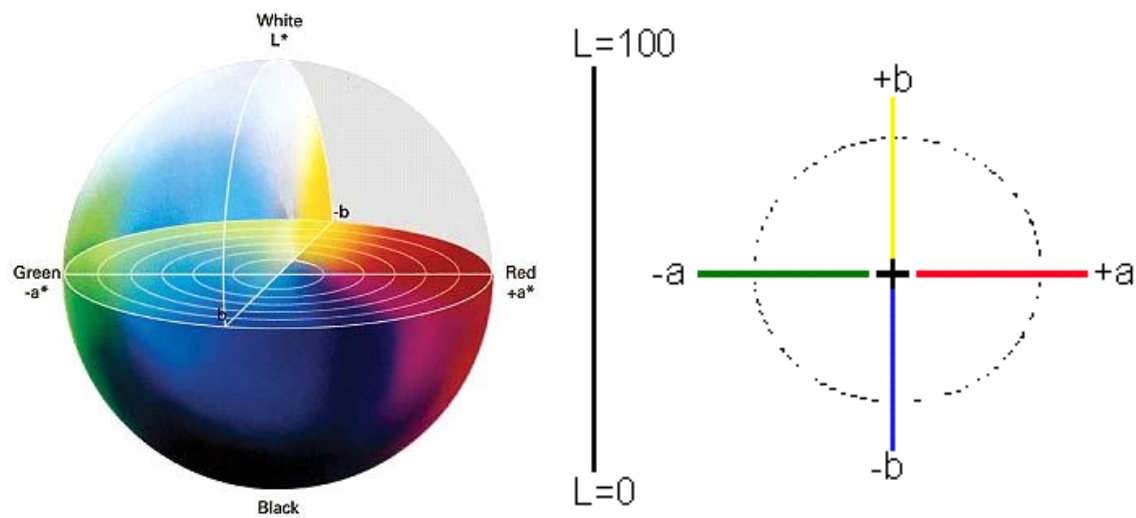


Figure 2.21 – CIE L^* , a^* , b^* colour space model.

Colour measurements have been taken after 7 of the 28 days of preliminary curing (starting point), after 45 cycles and at the end of the 93 cycles.

References

1. Ultrafine TiO₂ - Photocatalysis, http://www.millenniumchem.com/Products+and+Services/Products+by+Type/Specialty+Titanium+Dioxides/p_Ultrafine+TiO2+-+photocatalysis/Ultrafine+TiO2+-+photocatalysis_EN.htm.
2. Tioxide_A-HR_Technical_Data_Sheet, Huntsman Tioxide Pigments Corp. edn., pp. 1-2.
3. D. A. Skoog, F. J. Holler and T. A. Nieman, *Principles of Instrumental Analysis*, 5th edn., Harcourt College Publishers, 1997.
4. The Kubelka - Munk theory, applications and modification, http://webstaff.itn.liu.se/~freco/Publications/Courses/Paper_optics_presentation.pdf.
5. H. Lin, C. P. Huang, W. Li, C. Ni, S. Ismatshah and Y. Tseng, *Appl. Catal. B-Environ.*, 2006, **68**, 1-11.
6. B. D. Cullity and S. R. Stock, *Elements of X-Ray Diffraction*, 3rd edn., Prentice-Hall Inc., 2001.
7. R. Jenkins and R. L. Snyder, *Introduction to X-Ray Powder Diffractometry*, 1st edn., John Wiley & Sons Inc., 1996.
8. Bruker AXS Inc., *DIFFRACplus EVA - Bruker X-ray diffraction pattern database software*, Madison, WI.
9. E. Dowty, *ATOMS Shape Software*, Kingsport, TN.
10. S. Brunauer, P. H. Emmett and E. Teller, *J. Am. Chem. Soc.*, 1938, **60**, 309-319.
11. E. P. Barrett, L. G. Joyner and P. P. Halenda, *J. Am. Chem. Soc.*, 1951, **73**, 373-380.
12. *United States Pat.*, 5,840,111.
13. *United States Pat.*, 4,206,021.
14. *Europe Pat.*, EP 0722905 A1.
15. *Europe Pat.*, EP 0782971 A1.
16. D. Briggs and M. P. Seah, *Practical Surface Analysis*, 1st edn., John Wiley & Sons Inc., 1983.
17. NIST X-ray Photoelectron Spectroscopy Database, Version 3.5 (National Institute of Standards and Technology, Gaithersburg, 2003), <http://srdata.nist.gov/xps/>.
18. M. Kosmulski, *Surface Charging and Points of Zero Charge*, 1956.
19. Z. Jingxian, J. Dongliang, L. Weisensel and P. Greil, *J. Eur. Ceram. Soc.*, 2004, **24**, 2259-2265.
20. Y. F. Houst, P. Bowen, F. Perche, A. Kauppi, P. Borget, L. Galmiche, J.-F. Le Meins, F. Lafuma, R. J. Flatt, I. Schober, P. F. G. Banfill, D. S. Swift, B. O. Myrvold, B. G. Petersen and K. Reknes, *Cem. Conc. Res.*, 2008, **38**, 1197-1209.
21. NANOCEM - The industrial-academic research network on cement and concrete, <http://www.nanocem.org/>.
22. ISO_679, 2009.
23. UNI_11247, 2009, 1-11.
24. N. Daneshvar, D. Salari, A. Niaei, M. H. Rasoulifard and A. R. Khataee, *J. Environ. Sci. Health*, 2005, **40**, 1605-1617.
25. *Accelerated Aesthetic Ageing at Product Technology*, Aalborg Portland A/S.
26. HunterLab, <http://www.hunterlab.com/>.
27. Hunter L*a*b* Colour Model, http://www.labcognition.com/panoramaonlinehelp/englisch/colorimetric_analysis/color_models/cie_1976_l_a_b_color_model.htm.

Results and Discussion

3.1. Photocatalyst characterisation

3.1.1. Bulk properties

3.1.1.1. *Light absorption – U.V.-vis. Diffuse Reflectance*

U.V. – vis diffuse reflectance spectra obtained for the powder TiO₂ samples are shown in Figures 3.1 for m-TiO₂ and 3.2 for n-TiO₂. Indirect semiconductors (like TiO₂) near the absorption threshold have an absorption coefficient expressed by the relation:

$$\alpha = \frac{B_i (h\nu - E_g)^2}{h\nu} \quad (3.1)$$

where B_i is the absorption constant, h the Planck's constant equal to 6.626 10⁻³⁴ J s, ν the frequency of the light and E_g the band gap of indirect allowed transition. Therefore, a transformed Kubelka – Munk function, Equation 2.6, can be built to derive the value of the band gap¹⁻³. The inset in each graph shows the Kubelka – Munk transform versus the Energy of the incident light. The extrapolation of the linear portion is used to derive the band gap. Results for the two titania powders read:

$$E_g(\text{m-TiO}_2) = 3.29 \pm 0.02 \text{ eV}$$

$$E_g(\text{n-TiO}_2) = 3.34 \pm 0.02 \text{ eV}$$

These values are typical for *undoped* anatase TiO₂, as already reported by many other authors^{1, 4}. The band gap between valence and conductance band of about 3.2 – 3.3 eV for both the samples means that they do not absorb light in the visible field and their absorption edge lies completely in the near U.V. portion of the electromagnetic spectrum.

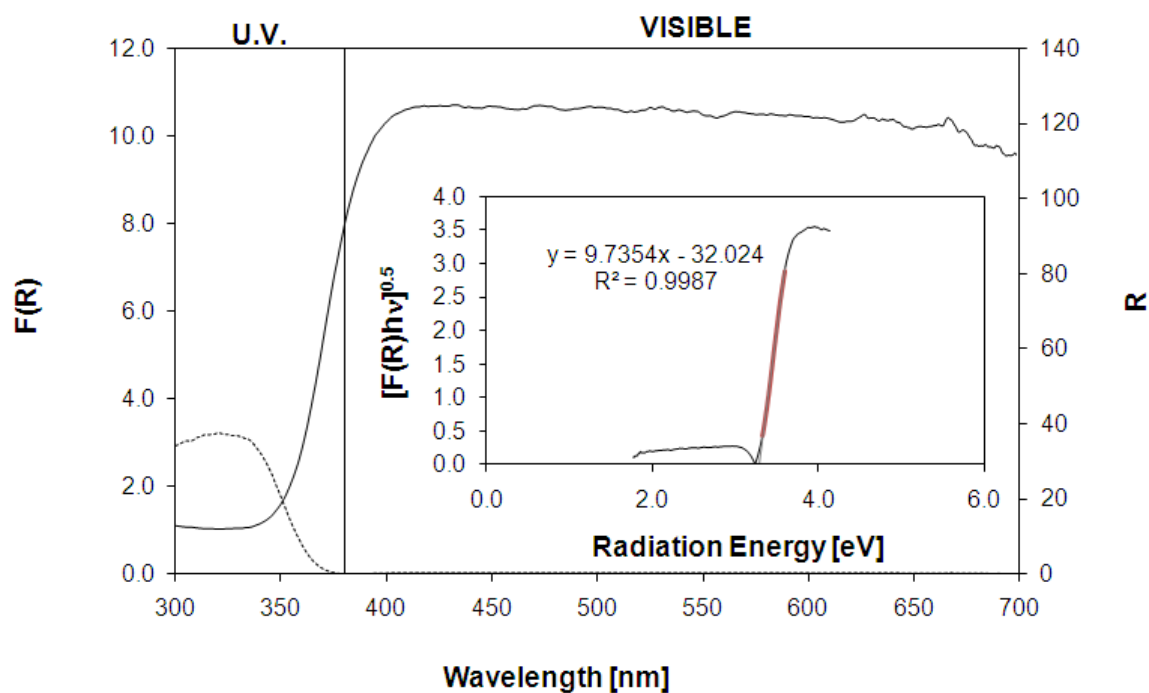


Figure 3.1 – U.V.-vis Diffuse Reflectance spectrum for m-TiO₂ (— R; --- F(R)).

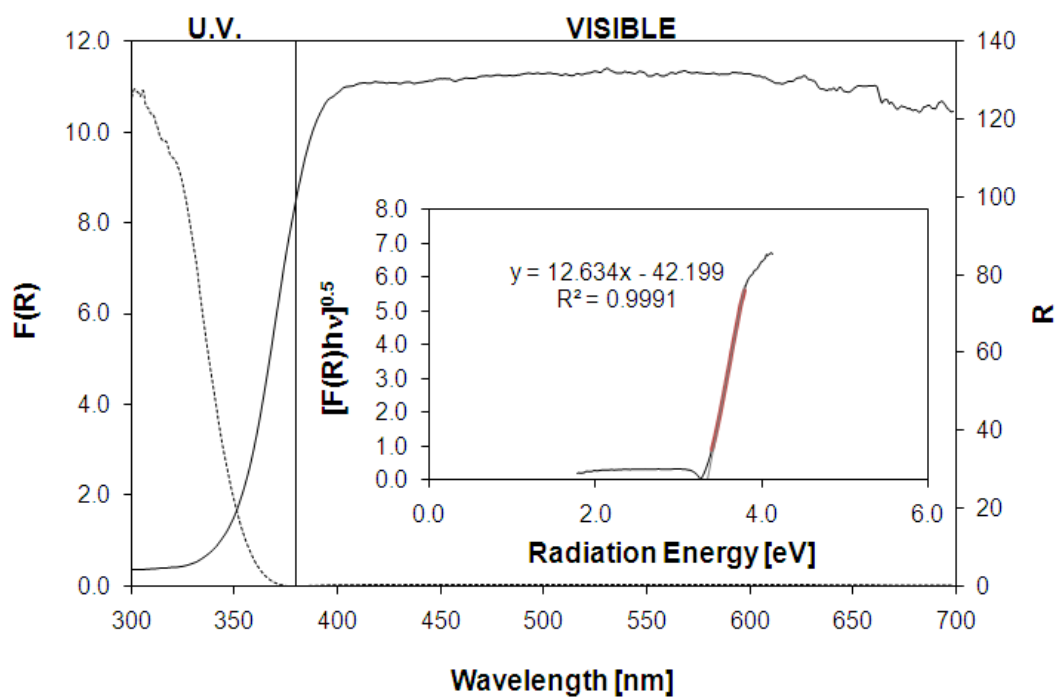


Figure 3.2 – U.V.-vis Diffuse Reflectance spectrum for n-TiO₂ (— R; --- F(R)).

3.1.1.2. Crystallinity and Polymorphism – X-Ray Diffraction

The results of X-ray diffraction analyses are shown in Figure 3.3. The peak positions confirm that anatase is the only detectable TiO_2 polymorph^{5,6}. Neither rutile/brookite peaks nor other crystalline substances have been detected. This is in agreement with what is declared by the manufacturers, i.e both the samples are solely anatase.

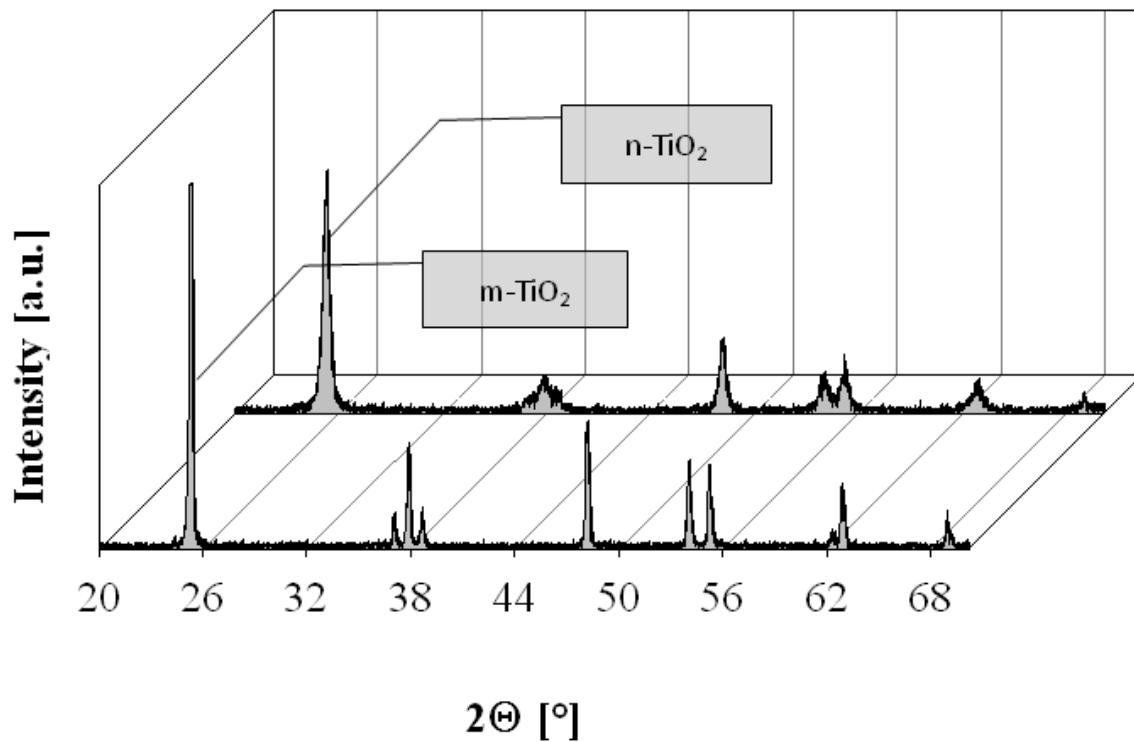


Figure 3.3 – XRD patterns for m- and n- TiO_2 .

Nevertheless the two patterns differ in resolution and peak broadening. These differences can be attributed to particle size only. The shape of XRD peaks depends on three main factors:

- i. Particle size;
- ii. Field strain;
- iii. Instrument effects;

The three contributions can be summarised in the following Equation:

$$FWHM_i^2 = \left(\frac{A}{\cos \theta_i} \right)^2 + (B \tan \theta_i)^2 + C^2 \quad (3.2)$$

where FWHM the Full Width at Half Maximum of peak i , θ_i the Bragg's diffraction angle of the peak i , A , B and C three experimental constants depending respectively on particle size, field strain and instrument characteristics^{7,8}. For crystallites bigger than about 100 nm there is no significant peak broadening due to particle size and the XRD peaks look very narrow and well resolved^{7,8}. This is what is observed for m-TiO₂ (where crystallite size is expected to be around 170 nm). Intensity of signals is really high and peaks are very well resolved. On the other hand, when crystallite size is between 10 and 100 nm, XRD peaks broaden significantly and both signal intensity and resolution decrease. In such conditions, strain field and instrument effects can be neglected and the parameter A can be expressed through the relation:

$$A = \frac{0.9\lambda}{d} \quad (3.3)$$

where λ is the X-ray wavelength and d the average particle diameter (considering the approximation that particle are spheres). By substituting Equation 3.3 in Equation 3.2, neglecting the other two contributions as explained before to derive the explicit form of d , the Scherrer Equation (Equation 2.9) is obtained:

$$d = \frac{0.9\lambda}{FWHM \cos\theta_i} \quad (2.9)$$

n-TiO₂ lies exactly in this second case. Being a well crystallised TiO₂, its less intense, broader and not well resolved XRD peaks, compared to m-TiO₂, suggest much smaller crystallite size. Measuring the FWHM of the main anatase peak (101) at about $2\theta = 25.2^\circ$ for three different patterns of the sample and applying the Scherrer Equation, a value for n-TiO₂ particle size of 16.6 ± 2.0 nm was derived. This seems to be in good agreement with data declared by the manufacturer of about 17 nm. Particle size of both m-TiO₂ and n-TiO₂ will be further discussed in section 3.1.1.4.

3.1.1.3. *Thermokinetics of TiO₂ surface dehydration – Thermogravimetry, Differential Thermal Analysis and Diffuse Reflectance Infrared Fourier Transform Spectroscopy*

Figure 3.4 shows the TG, DTG and DTA profiles for both m-TiO₂ and n-TiO₂.

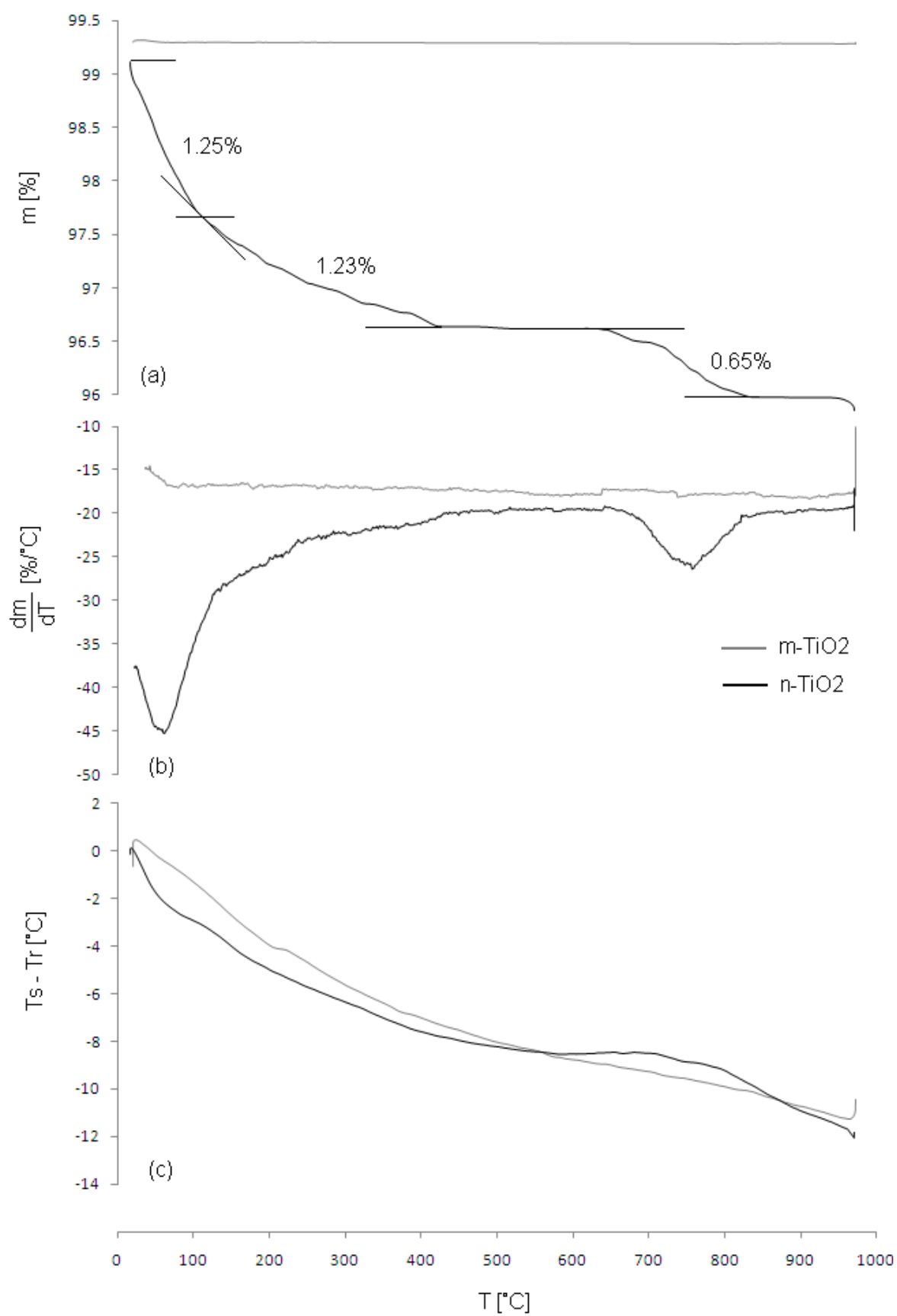
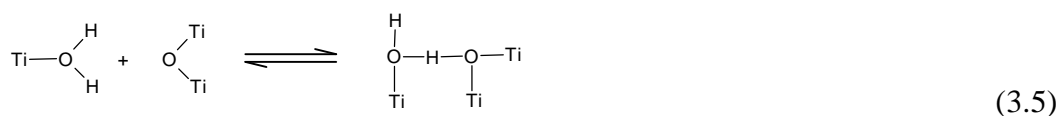


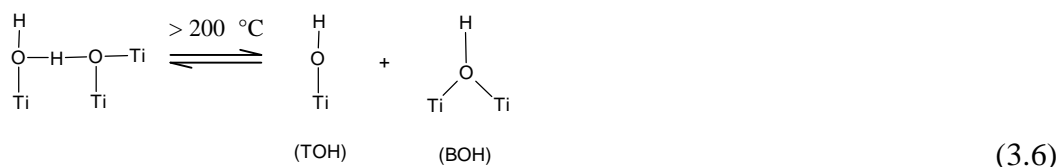
Figure 3.4 – TG (a), DTG (b) and DTA (c) profiles for m-TiO₂ and n-TiO₂.

m-TiO₂ did not show any measurable thermal phenomena. Its TG profile is flat all over the scanned temperature range, so is the DTG. In agreement with the thermogravimetric results, DTA did not exhibit any significant endo- or exothermic events.

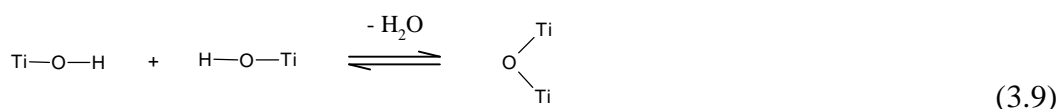
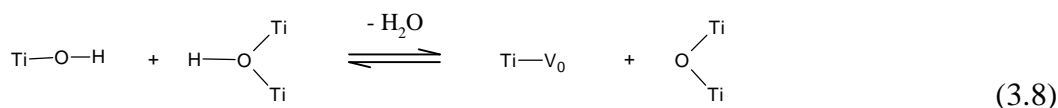
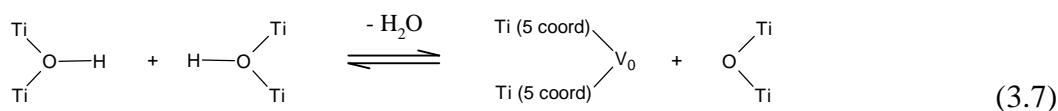
More interesting is the behaviour of n-TiO₂. TG showed at least three distinct thermal processes. A low temperature weight loss which ended around 110 °C, a subsequent weight loss which reached a steady state around 500 °C and a third weight loss which started at 600 °C and it was completed around 850 °C. DRIFT spectroscopy helps to identify the nature of such thermal events. Figure 3.5 shows TG analysis with DRIFT spectra as insets. In the first weight loss step between 20 °C and 110 °C, DRIFT spectra (inset (a)) showed a broad band between 3300 and 3200 cm⁻¹. This is associated with O–H stretching of molecular H – bonded water. The sharp band at 1623 cm⁻¹ is relative to *in plane* O–H bending of the same molecular water. These bands systematically decrease in intensity with increasing temperature and indicate molecular water removal from the TiO₂ surface⁹. Previous works^{9, 10} already showed that adsorbed molecular water can still exist at 200 °C and the persistence of bands at 3200 and 1623 cm⁻¹ in inset (b), obviously with reduced area confirms this. However, above 150 °C a new band at about 3670 cm⁻¹ was formed. This band may be assigned to those surface hydroxyl groups which, being no longer involved in H bonds with molecular water, are now free to vibrate at this frequency. Furthermore, at temperatures higher than 200 °C even *chemisorbed molecular* water may dissociate. Water on TiO₂ surfaces mainly chemisorbs on oxygen vacancies (V_O) (crystal defects), as reported by Trimboli et al.⁹, Henderson et al.^{10, 11}, Liu et al.¹², extensively discussed in the review by Fu et al.¹³ and confirmed by *ab initio* density-functional theory (DFT) calculations by Iacomino et al.¹⁴. In anatase crystals, Ti atoms occupy centres of octahedra and coordinate six oxygen atoms. Surface oxygen vacancies lead to five – coordinated titanium atoms able to bind the oxygen of water molecules (Equation 3.4). Eventually one of the two hydrogen atoms forms a hydrogen bond with a neighbour bridging oxygen^{9, 10, 13} (Equation 3.5).



Trimboli et al.⁹ and Henderson et al.^{10, 11} reported the dissociation of the water adduct in Equation 3.5 into *terminal* OH groups (TOH, O–H stretching at 3710 cm⁻¹) and *bridging* OH groups (BOH, O–H stretching at 3660 cm⁻¹) at temperatures higher than 200 °C (Equation 3.6).



Our experimental data seem to fully confirm this route. Inset (c) shows a distinct signal at 3670 cm⁻¹ (BOH) with a shoulder around 3719 cm⁻¹ (TOH) at a temperature higher than 200 °C. The area of these signals increases in spectra of samples treated at about 350 – 400 °C (inset (e)) and decreases with further temperature increase suggesting water removal due to TOH and BOH condensation:



This contributes to the weight loss measured by TG at temperatures higher than 350 °C. The continuous weight loss above 200 °C coupled with the DRIFT signal at 3200 cm⁻¹, which monotonically decreases in area and yet is still present at 500 °C, suggest also a continuous molecular water removal. However, no molecular physisorbed or H – bonded water can survive these temperatures. Parkins¹⁵ assumed this signal to be associated with strongly chemisorbed water at isolated sites which does not undergo dissociation as highlighted above. The remaining water present on the surface (both molecular water and dissociated water) is removed at very high temperature (600 – 850 °C) as indicated by the TG trend. This confirms once again results previously observed for other metal oxide surfaces¹⁶ about presence of water up to 800 – 900 °C.

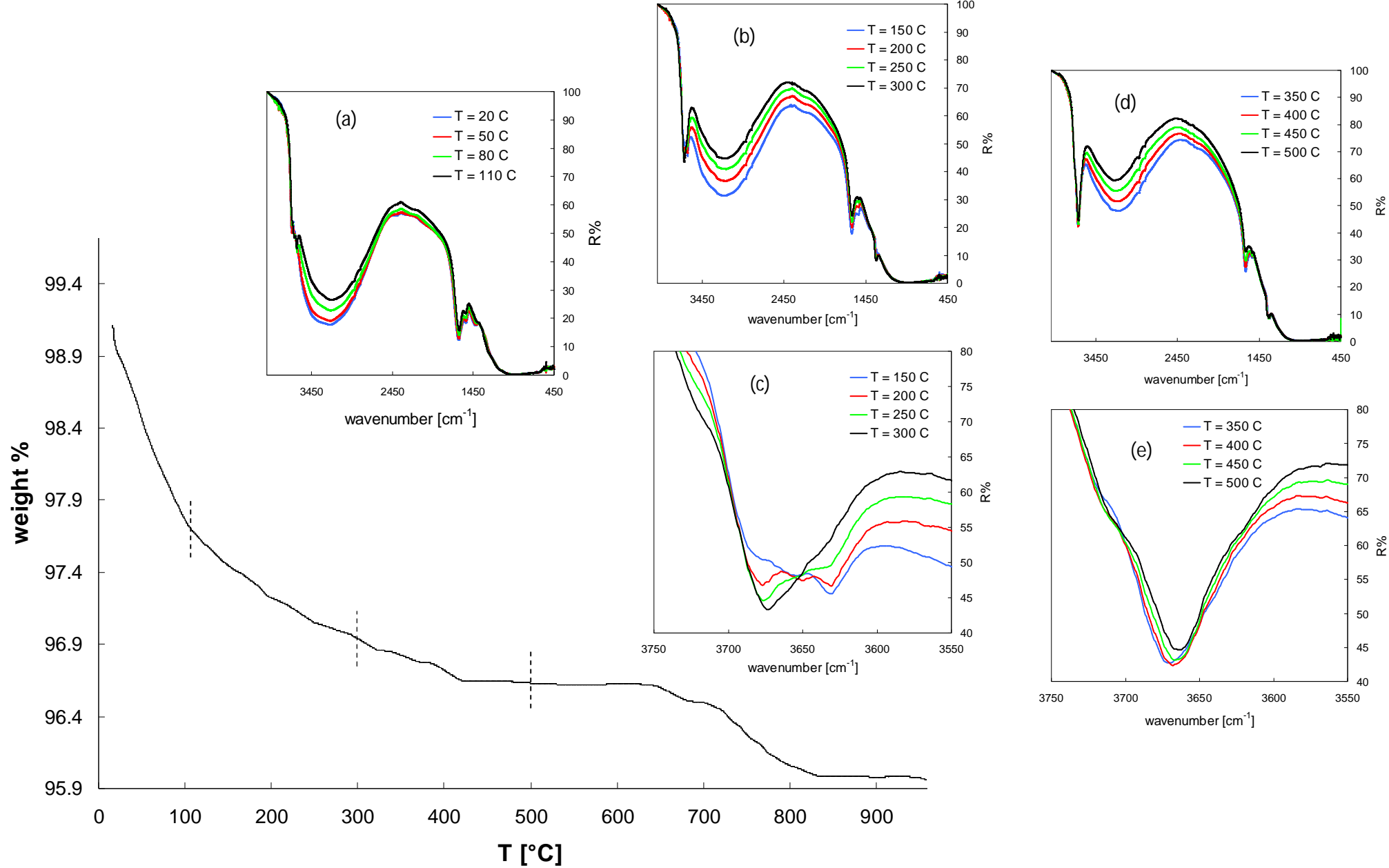


Figure 3.5 – TG and DRIFT spectra for n-TiO₂.

3.1.1.4. Particle size and morphology - Transmission Electron Microscope imaging

Figure 3.6 shows the transmission electron micrographs obtained for m-TiO₂, inset (a), and n-TiO₂, inset (b).

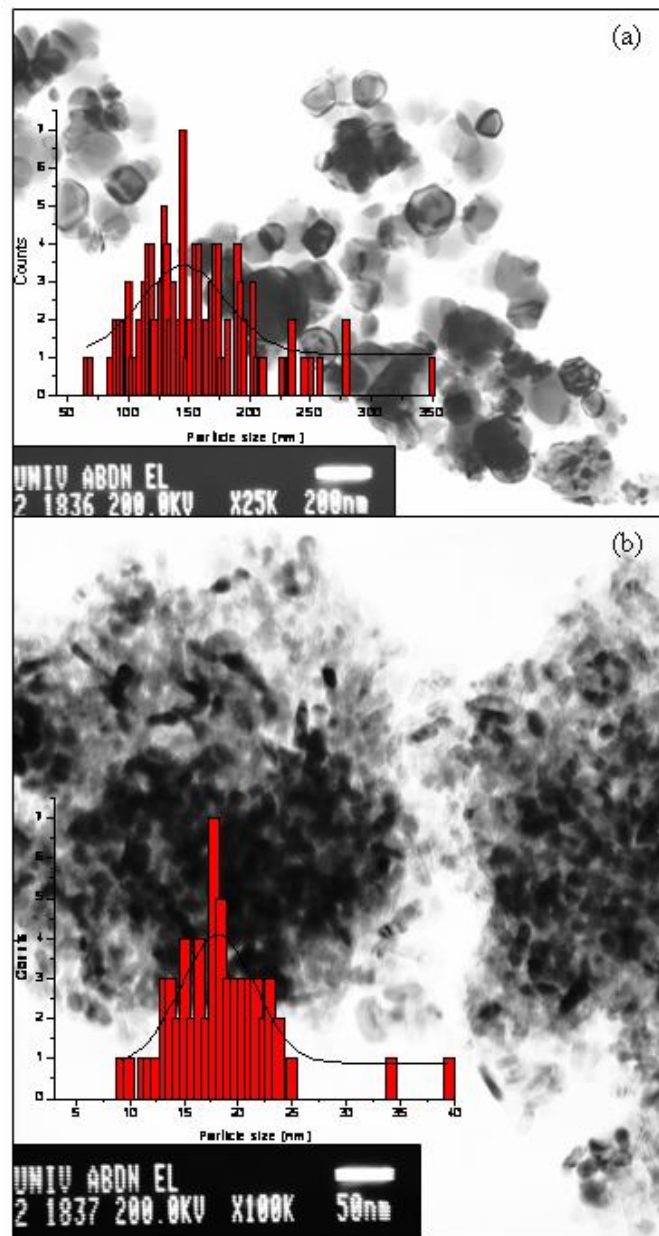


Figure 3.6 – Transmission electron micrographs for m-TiO₂ (a) and n-TiO₂ (b).

The scale of the micrographs highlights a large difference in crystallite size for the two samples studied. Furthermore, these images reveal important characteristics about particle agglomerates and porosity. m-TiO₂ shows clusters constituted by a few crystallites whilst n-TiO₂ clusters are generated by a large number of crystallites. The relatively larger dimension of m-TiO₂ particles is also responsible for the larger inter-particle porosity that this sample exhibits if compared to n-TiO₂. Image analysis was carried out on both the samples, measuring the size of more than one hundred particles for each sample, and generated the statistical distributions showed in Figure 3.6. The average particle sizes obtained were:

$$\bar{d}_{m-TiO_2} = 153.7 \pm 48.1 \text{ nm}$$

$$\bar{d}_{n-TiO_2} = 18.4 \pm 5.0 \text{ nm}$$

These results (Table 3.1) are in good agreement with manufacturers' product specifications (Table 2.2) and with data obtained using the Scherrer Equation (Equation 2.9) applied to XRD patterns.

3.1.2. Surface properties

3.1.2.1. *Specific Surface Area and Inter-particle porosity – N₂ adsorption (B.E.T. and B.J.H. models)*

Multilayer N₂ physisorption isotherms at 77 K on m-TiO₂ and n-TiO₂ are shown in Figure 3.7. n-TiO₂ showed a clear Type II isotherm, indicative of chemical affinity between adsorbate, N₂, and TiO₂ surface and characteristic of porous materials with pores distributed around a single size which is in the transitional range mesoporosity – macroporosity, i.e.: from a few tens to a few hundred Angstroms. m-TiO₂ on the other hand, showed a similar Type II isotherm where the much lower level of N₂ adsorption and the smaller area of the hysteresis loop are consistent with this sample showing larger crystallites than the nanosized product. The phenomenon of hysteresis in adsorption – desorption isotherms highlights different *pathways* for adsorption and desorption

mechanisms respectively. Hysteresis can be explained in terms of capillary condensation governed by the Kelvin Equation:

$$\ln \frac{P}{P_0} = -\frac{2H\gamma V}{RT} \quad (3.10)$$

where P is the actual N_2 pressure, P_0 the vapour pressure of N_2 at 77 K, H the mean curvature of the meniscus generated by N_2 vapour condensation in the capillary pore, γ the liquid – vapour surface tension, V the molar volume of the liquid, R the universal gas constant and T the temperature. Considering pore with cylindrical geometry, the meniscus mean curvature, H can be expressed as:

$$H = \frac{\cos \theta}{r_{g,i}} \quad (3.11)$$

where θ is contact liquid – pore wall contact angle and $r_{g,i}$ the geometrical radius of the pore i . This Equation governs all equilibrium systems involving menisci and accounts for condensation of a vapour species inside a capillary at pressure P below the saturation vapor pressure P_0 . In a *bottle – neck* geometry pore, condensation starts at the *bottom* of the bottle at a pressure given by:

$$P_a = P_0 \exp\left(-\frac{2\gamma V \cos \theta}{RT r_1}\right) \quad (3.12)$$

where r_1 is the radius at the bottom of the bottle shaped capillary. The pore continues to be filled up more or less rapidly with further addition of gas until saturation: $\left(\frac{P_k}{P_0}\right) = 1$.

On the desorption route, however, the pore starts to be emptied at the *neck* of the bottle when the pressure is:

$$P_d = P_0 \exp\left(-\frac{2\gamma V \cos \theta}{RT r_2}\right) \quad (3.13)$$

where r_2 is the radius at the neck of the bottle shaped capillary. Therefore:

$$\forall r_2 < r_1 \Rightarrow \frac{P_d}{P_a} = \frac{\exp(1/r_1)}{\exp(1/r_2)} < 1 \quad (3.14)$$

Equation 3.14 simply reads: for a given amount of adsorbate condensed in the pore, the pressure at which this amount is left in the pore during desorption is always lower than the pressure at which this same amount is condensed during adsorption, explaining the higher position of the desorption curve compared to that of the adsorption curve defining the hysteresis loop in Figure 3.7.

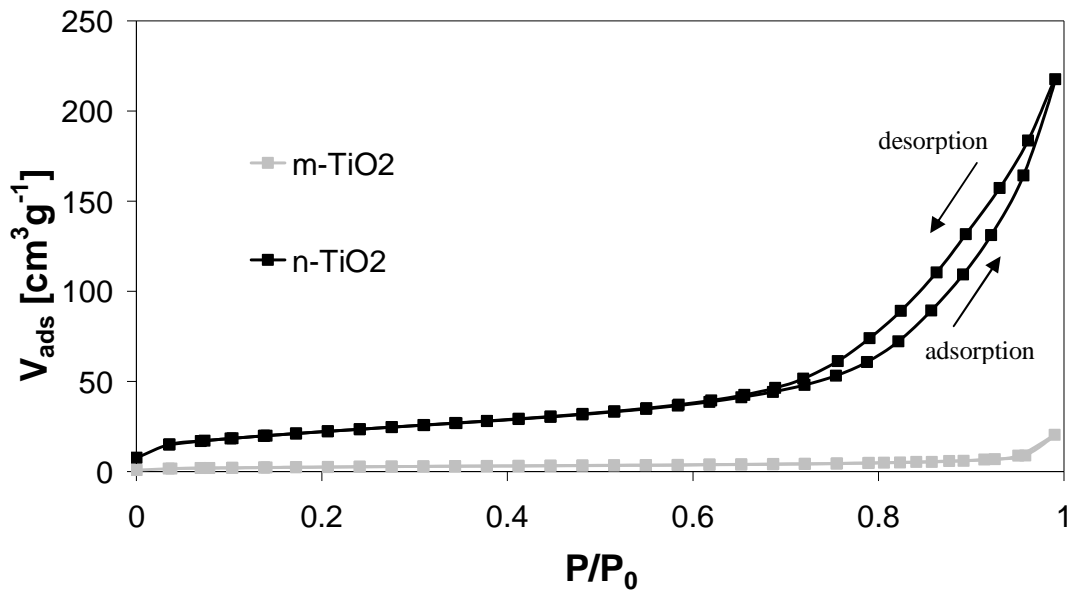


Figure 3.7 – N₂ physisorption isotherms at 77 K for m-TiO₂ and n-TiO₂.

Although the simple bottle – neck theory qualitatively explains the adsorption – desorption hysteresis, it fails if used for quantitative interpretations. A more general explanation of hysteresis is provided by Foster ¹⁷ assuming an *open pore* structure of the adsorbent.

Figure 3.8 shows the mesopore volume distribution analysis obtained using the BJH model. n-TiO₂ exhibited a pore distribution centred on 80 Å. This is a direct consequence of the type II N₂ adsorption isotherm. On the other hand, no mesoporosity has been observed for m-TiO₂. Coupling of BJH analysis with TEM micrographs shows that the

pore volume measured through the BJH model on N₂ adsorption data is mainly related to the volume arising from particle agglomeration rather than intra particle pore volume. The smaller n-TiO₂ particles (18.4 ± 5.0 nm by TEM) generate clusters with mesopores of several tens of angstroms whilst the bigger m-TiO₂ particles generate clusters with macropores; size distribution data for these cannot be obtained using the BJH model since its applicability range is restricted to the mesopore field only.

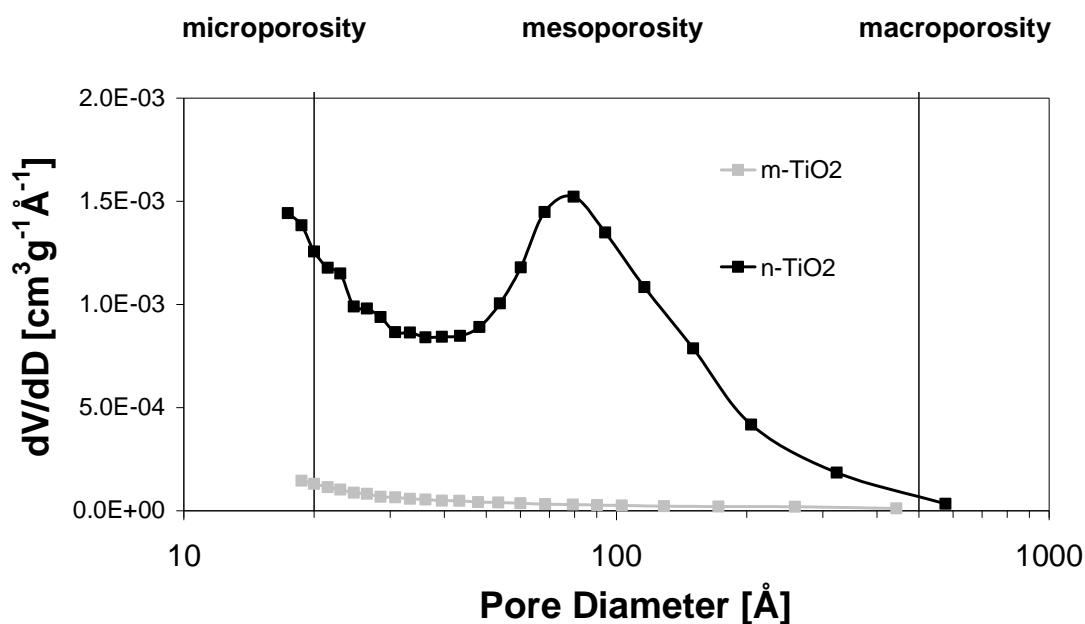


Figure 3.8 – BJH pore distribution analysis for m-TiO₂ and n-TiO₂.

Specific surface area data have been also used to derive particle size through the simple geometrical model described in section 2.2.2.1 and by Equation 2.15. There is good agreement between the techniques and the results are consistent with the manufacturers' data on particle size.

3.1.2.2. Surface composition analysis – X-Ray Photoelectron Spectroscopy and Energy Dispersion Spectroscopy

Figure 3.9 shows XPS spectra of m-TiO₂ and n-TiO₂. The Ti 2p^{3/2} and Ti 2p^{1/2} peaks at 459.2 eV and 465.1 eV respectively (doublet separation of about 5.9 eV) together with the satellite peak shifted by about 13.8 eV from the main Ti 2p^{3/2} peak, are typical of

TiO₂ ¹⁸. The **O** 1s region is different for the two samples. n-TiO₂ showed a mean peak at 530.0 eV, evidence of an unmodified surface ¹⁹. The shoulder around 532.0 eV means that the surface is partially covered with OH groups ^{20, 21}. m-TiO₂ has an **O** 1s peak at about 531.0 eV and a shoulder around 533 eV. Nevertheless this signal seems to overlap with another small peak around 535.0 eV (see deconvolution in Figure 3.9). The latter is not an unambiguous signal and could be attributed to the oxygen of various groups. Nevertheless the peak at 535 eV could be attributed to P – O groups on the surface of m-TiO₂ due to simultaneous presence at 133.4 eV of a **P** 2p^{3/2} peak, Figure 3.10(a). Binding energies around 133 – 134 eV are typical of phosphorous bound to oxygen atoms. No phosphorous was detected on the surface of n-TiO₂. XPS analysis also revealed the presence of K for m-TiO₂ and traces of N for n-TiO₂., Figure 3.10(b) and 3.10(c). Na and S were also detected, Figure 3.10(d) and 3.10(e). This is characteristic for titanias produced according to the sulphate process. S comes from the raw materials used in manufacturing and Na from NaOH used to neutralise the hydrolysis product (i.e. acidic TiO₂ produced by hydrolysis of TiOSO₄).

Table 3.1 – Particle size evaluation by TEM, XRD and BET.

Sample	Particle size			
	Product Spec	TEM	XRD	BET
	<i>nm</i>	<i>nm</i>	<i>nm</i>	<i>nm</i>
m-TiO ₂	170	153.7±48.1	–	177.6
n-TiO ₂	17	18.4±5.0	16.6±2.0	19.5

EDS also revealed the presence of P and K for m-TiO₂. n-TiO₂ exhibited traces of K but no P at all. These analytical findings for m-TiO₂ seem to confirm the presence of K and P disclosed in one of the manufacturer's patent ²²: the hydrous TiO₂ is calcined in the presence of a P compound in an amount between 0.15 % and 0.55 weight %, expressed as P₂O₅, and in the presence of a K compound in an amount between 0.20 % and 0.60 weight %, expressed as K₂O ²². Figure 3.11 shows the quantitative analysis performed by EDS using P and K K lines and expressed as P₂O₅ and K₂O. The results of 0.25 ± 0.02 %

for P_2O_5 and $0.19 \pm 0.05 \%$ for K_2O are within the ranges declared in the manufacturer's patent ²².

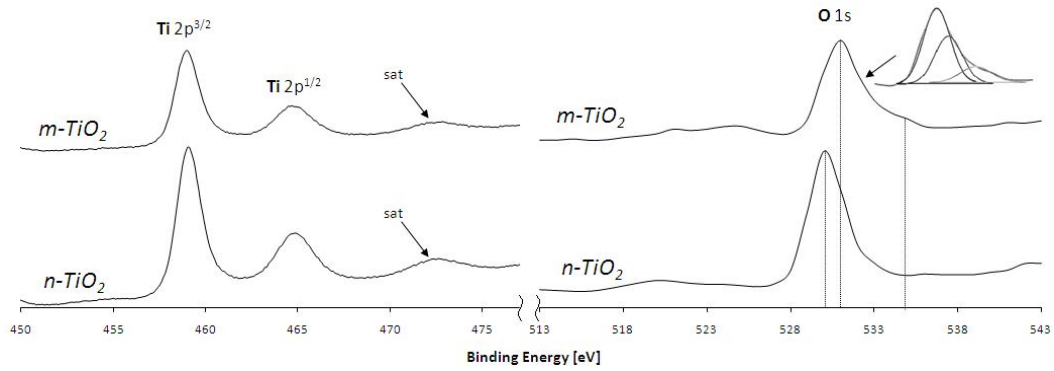


Figure 3.9 – m-TiO₂ and n-TiO₂ XPS spectra (Ti 2p and O 1s regions).

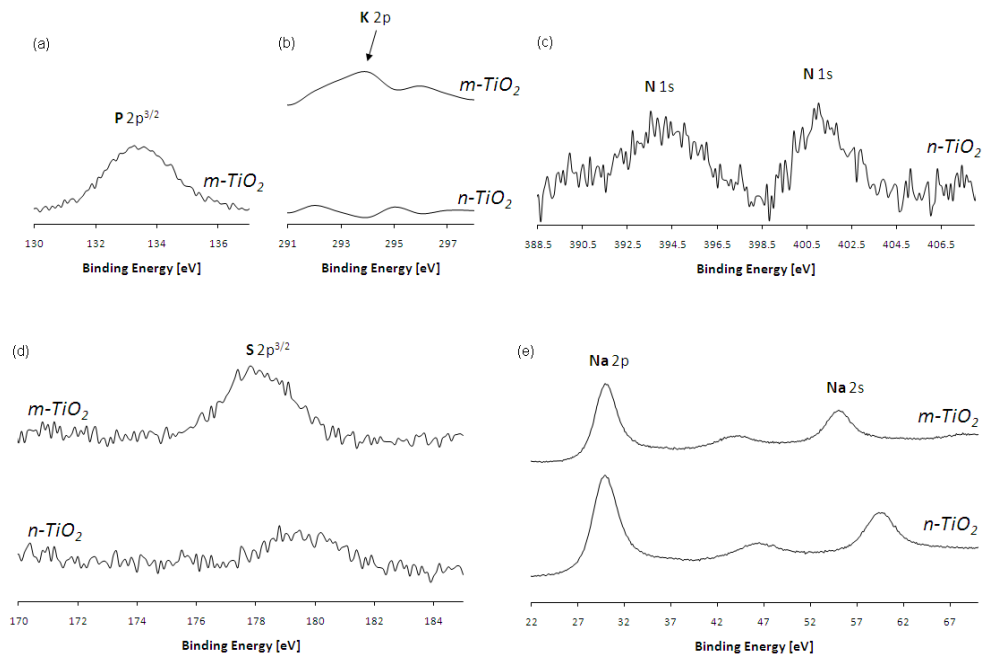


Figure 3.10 – m-TiO₂ and n-TiO₂ XPS spectra.

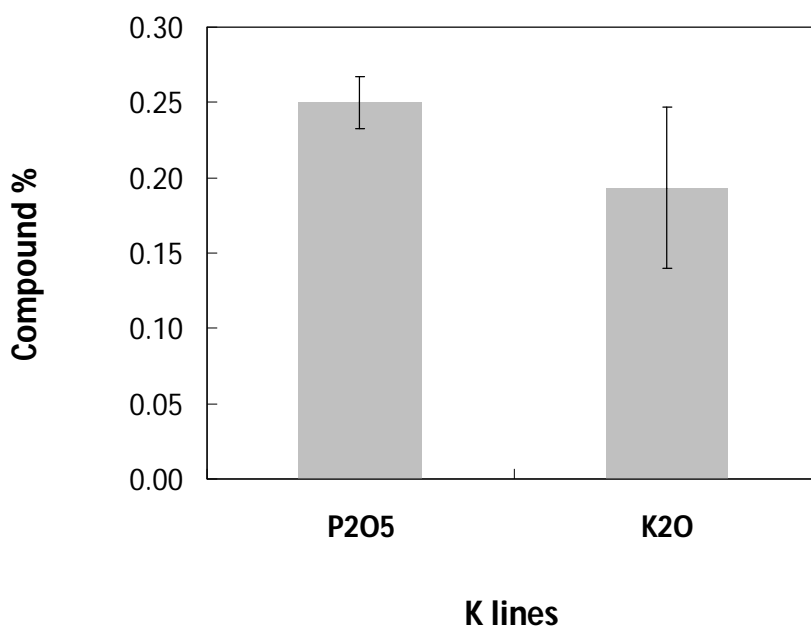


Figure 3.11 – EDS results for m-TiO₂. P expressed as P₂O₅ and K as K₂O.

3.1.2.3. *Electrokinetic properties – ζ -potential and surface charge density*

Figure 3.12 and Figure 3.13 show ζ -potential and surface charge density trends for the two titania samples investigated. ζ -potential trend for n-TiO₂ is typical for titania particles as reported by other authors²³⁻²⁵. The pH for which the ζ -potential equals zero, named the iso-electric point (IEP), was found to be at pH 6.5. The PZC found for n-TiO₂ by the method of zero change of pH reads 6.5 too (see Figure 3.13, surface charge density), indicating that the solution contains indifferent electrolytes only^{26, 27}. The IEP for m-TiO₂ was found at pH 2.1. The actual PZC is difficult to measure for m-TiO₂ because of the large variation of the titrant volume added for a small variation of pH at low pHs. However the trend indicates also a similar value to the IEP; indeed, once again, the solution contains indifferent electrolytes only.

The ζ -potential of m-TiO₂ is clearly modified relative to that of n-TiO₂, essentially by chemical modification of the surface. The atypical ζ -potential trend, the high surface

charge density and the low IEP (pH = 2), can be interpreted together with XPS data. XPS identified P – O bonds on the m-TiO₂ surface. Nelson et al.²⁶ observed that specifically adsorbed phosphates on titanium dioxide surfaces shift the IEP from about pH 7 to pH 2. In the case of m-TiO₂ there is no specific adsorption of any phosphate so P – O groups must rather be part of the surface structure. It has become apparent that m-TiO₂ is treated with a P compound during calcination²². The thermal process allows foreign ions to move to the surface and become part of the final product surface structure. XPS also showed that surfaces are partially hydroxylated, therefore the really low IEP measured for m-TiO₂ (and the possible value of the PZC suggested from the trend in Figure 3.13) is likely to be associated with P – OH surface groups, with deprotonation starting at much lower pH than for Ti – OH groups. Surface titanol groups, Ti – OH, are amphoteric and their ionisation equilibria can be written as²⁸:



with $pKa_1^s \approx 4.2$ ²⁸ and $pKa_2^s \approx 8$ ²⁸ (data for the nanosized Evonik Degussa P25 TiO₂). Surface titanol groups are in the Ti – OH form at a pH equal to the PZC, which, thermodynamically can be derived from the two acidic constants²⁸:

$$PZC = \frac{pKa_1^s + pKa_2^s}{2} \quad (3.17)$$

Equation 3.17 yields 6.1, very similar to the experimental value of 6.5 obtained by titration for n-TiO₂. At pHs lower than PZC partial protonation of Ti – OH leads to positive Ti – OH₂⁺ sites and at pHs higher than PZC partial deprotonation of Ti – OH leads to negative Ti – O⁻ sites (see reference²⁸ for surface speciation).

P – OH groups undergo similar mechanisms of protonation/deprotonation leading to positive and negative surfaces, but are much more acidic, accounting for the lower PZC of the P-containing m-TiO₂.

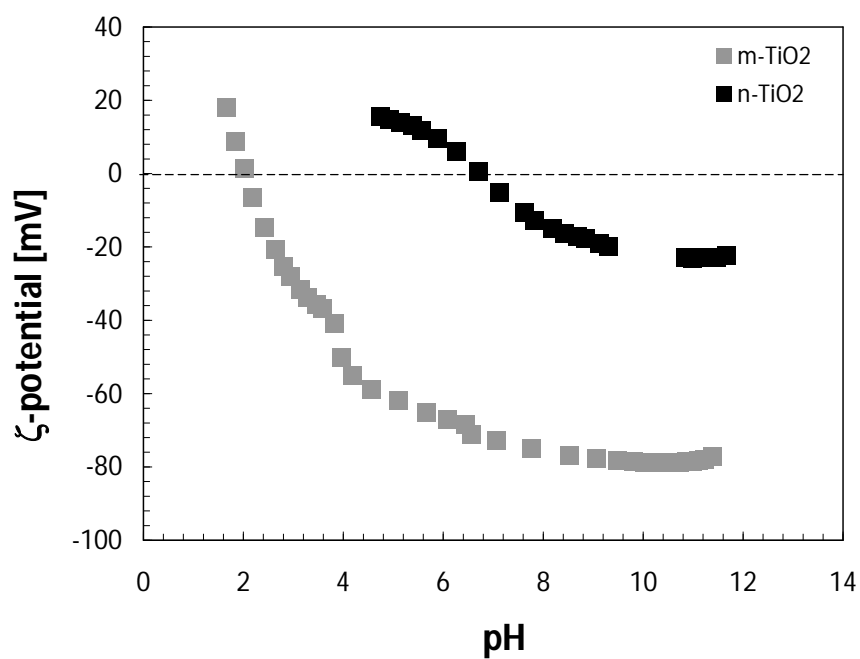


Figure 3.12 – m-TiO₂ and n-TiO₂ ζ-potentials vs pH. 1% TiO₂ suspensions in 0.01 M NaNO₃ solution.

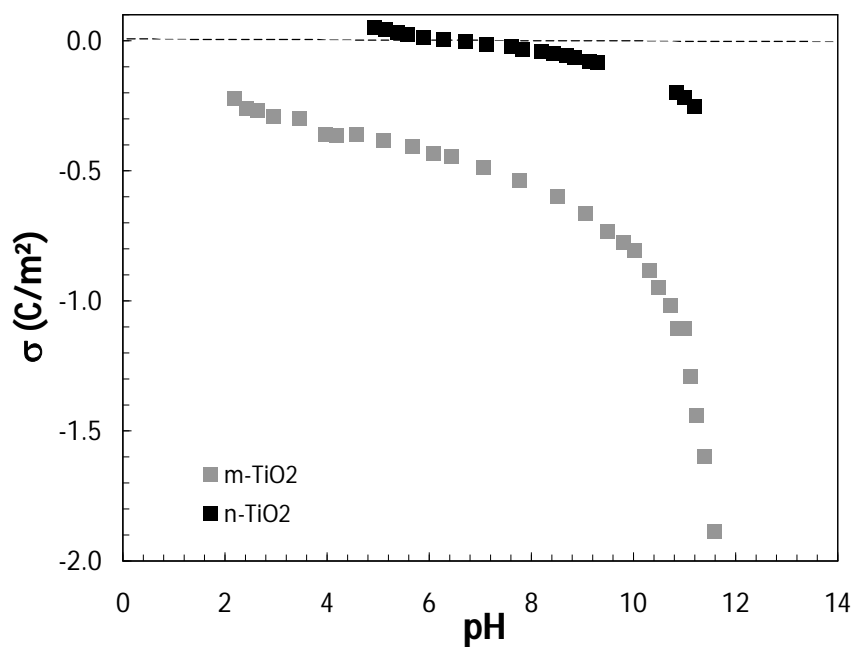


Figure 3.13 – m-TiO₂ and n-TiO₂ surface charge densities.

3.1.2.4. Dispersion stability – sedimentation test

3.1.2.4.1. m-TiO₂ and n-TiO₂ dispersions in the presence of Na⁺, Cl⁻ or deionised water

The stability of TiO₂ dispersions was tested in HCl, deionised water and NaOH, pH = 2, pH = 7 and pH = 12.5 respectively. According to the Deryagin-Landau-Verwey-Overbeek (DLVO) theory^{29, 30}, dispersion/agglomeration of particles are controlled by the balance between attractive and repulsive forces. Since these systems contain only 1:1 electrolytes, a mean field approach is able to describe the electric double layer interactions: repulsive contribution of entropic origin and attractive contribution resulting from Van der Waals (VDW) forces. ζ -potential can therefore be used as a parameter to interpret/predict dispersion or aggregation phenomena. A common sedimentation test to verify dispersion stability³¹ (Figure 3.14) highlighted that at pH = 2 in HCl, the m-TiO₂ dispersion is not stable and it readily sediments. At this pH there is no net surface charge on particles (IEP and PZC at pH = 2), interactions only come from attractive VDW forces so aggregation and sedimentation can be predicted. However, n-TiO₂ at the same pH shows a ζ -potential of about +20 mV (extrapolation of the trend in Figure 3.12 and²³⁻²⁵). This is enough to prevent sedimentation and the dispersion is perfectly stable at 24 h but also after 4 days. Furthermore, according to Mandzy et al²⁴, a potential of about |25 – 30| mV is the minimum threshold to *electrostatically stabilise* a *nanosized* TiO₂ dispersion (in presence of indifferent electrolytes only) mainly by breaking up big agglomerates, reducing their dimensions to primary particle size, and avoiding re-agglomeration. At pH = 7 (deionised water), the situation is exactly the reverse. The PZC is nearer 7 for n-TiO₂ so its dispersion is unstable. m-TiO₂, having a ζ -potential of about -75 mV at this pH, provides stable dispersion. At pH = 12.5 both of the samples show non-zero ζ -potentials: about -25 mV for n-TiO₂ and about -80 mV for m-TiO₂ (Figure 3.12) and, as expected, are highly dispersed with no significant differences in stability within 24 h. However, after 4 days m-TiO₂ looked better dispersed than n-TiO₂. This difference is likely to be associated with its higher ζ -potential which is able to compensate the greater VDW attractive interaction.

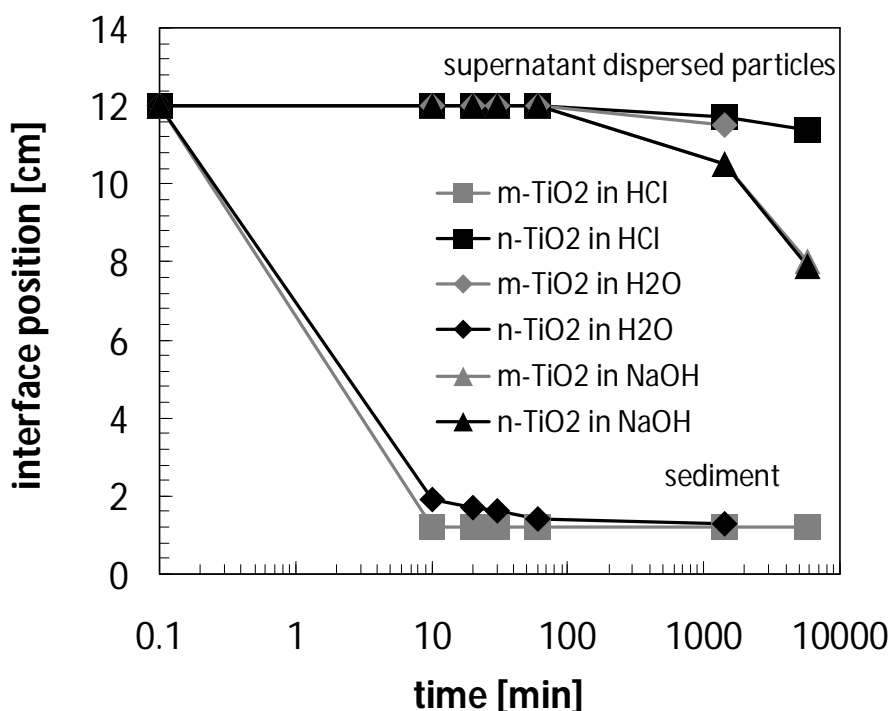


Figure 3.14 – Sedimentation test for m-TiO₂ and n-TiO₂ in HCl (pH = 2), deionised water (pH = 7) and NaOH (pH = 12.5).

3.1.2.4.2. m-TiO₂ and n-TiO₂ dispersions in the presence of K⁺

The same dispersions of m-TiO₂ and n-TiO₂ at pH = 12.5 have been prepared using a KOH solution (Figure 3.15). The potassium ion is considered to be an indifferent electrolyte too (no specific adsorption inside the Stern layer) but it is less polarising than sodium. Its hydration shell is smaller and weaker than the sodium one (see Table 3.2) and, as a result, stronger interactions between hydrated K⁺ ions and TiO₂ surface may occur. According to Shaw²⁷, K⁺ is expected to slightly destabilise colloidal suspensions. Monovalent electrolytes may increase flocculation according to their hydrated ionic radii²⁷. The smaller the solvated ionic radius the closer the counter-ion approaches the particle surface and the stronger the resulting interaction. Thus, monovalent cations can be arranged in a series of decreasing flocculating power (increasing solvated radius, see Table 3.2). This has been observed to be true for n-TiO₂ where, although within 24 h no particular differences with the Na⁺ case have been noticed, after 4 days titania powder

completely settled in KOH while the same dispersion in NaOH was still highly stable. For m-TiO₂ the observed situation is again totally different. The ζ -potential trend in Figure 3.12 is still valid because there are just indifferent electrolytes in solution, so high dispersion stability is expected due to the high ζ -potential value. However, this dispersion settled within one hour. A specific interaction between the high potassium activity environment and the P, K modified surface of m-TiO₂ seems to exist, even though the nature of such interaction is not completely clear and further investigations might be needed.

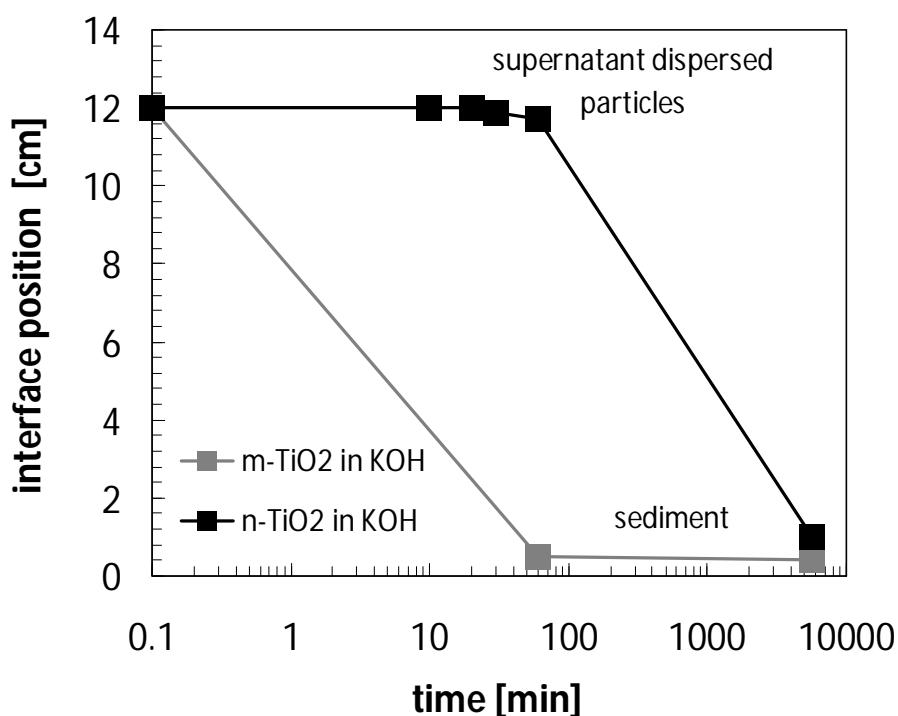


Figure 3.15 – Sedimentation test for m-TiO₂ and n-TiO₂ in KOH (pH = 12.5).

3.1.2.4.3. m-TiO₂ and n-TiO₂ dispersions in the presence of Ca²⁺

Divalent (and even more, trivalent) cations are known to decrease colloidal stability (increasing flocculation)³². Their higher charge makes them more polarising than monovalent cations and the coulombic attraction between the divalent cations and the negatively charged surface, as well as the coulombic repulsion amongst the cations

themselves, is greater than in the case of monovalent ions; this results in the so-called ion-ion correlations in the electrical double layer. In the conditions of high surface charge densities and in the case of multivalent counterions (highly coupled systems), ion-ion correlations can be at the origin of a surface *overcharging* phenomena and apparent surface charge reversal (CR)³³⁻³⁵. They introduce an attractive electrostatic contribution between particles with the same charges³⁶. Such phenomena have been demonstrated by many authors working on different colloidal systems and have been confirmed by several simulations³⁷⁻⁴³ as identified in two recent reviews^{44, 45}. Labbez et al. recently obtained important results quantifying such charge correlations for colloidal silica dispersions³³.

Table 3.2 – Data on hydration of aqueous Group IA ions and NH_4^+ .

	Cs^+	\approx	Rb^+	$<$	NH_4^+	\approx	K^+	$<$	Na^+	$<$	Li^+
hydrated											
ionic radius	2.28 ⁴⁶		2.28 ⁴⁶		≈ 2.32 ⁴⁶		2.32 ⁴⁶		2.76 ⁴⁶		3.40 ⁴⁶
[Å]							3.31 ⁴⁷		3.58 ⁴⁷		
Approximate	9.9 ⁴⁶						10.5 ⁴⁶		16.6 ⁴⁶		25.3 ⁴⁶
hydration											
numbers	6 ⁴⁸						7 ⁴⁸		13 ⁴⁸		22 ⁴⁸
Hydration											
Enthalpy	264 ⁴⁶		293 ⁴⁶				322 ⁴⁶		406 ⁴⁶		519 ⁴⁶
[kJ mol⁻¹]							295 ⁴⁹		365 ⁴⁹		

These effects on different TiO_2 samples have been proved here. Experimental results confirmed first evidences of TiO_2 charge reversal in the presence of Ca^{2+} discussed by Mange et al.⁴⁰ and Böhmer et al.⁵⁰. Moreover, charge correlation effects observed can be used to explain TiO_2 aggregation/dispersion in real cement structures.

ζ -potential measurements performed on m- TiO_2 and n- TiO_2 at different Ca^{2+} activities showed different trends to those for the Na^+ case (Figure 3.16). As mentioned before, in

alkaline conditions n-TiO₂ titanol groups are partially ionised to Ti-O⁻ leading to a negative surface charge. Increasing calcium concentrations decrease the absolute value of ζ -potential until Ca²⁺ ions completely balance the surface charge and the overall potential at the shear plane is zero. *This new IEP is not at the PZC.* Although the actual TiO₂ surface is still negatively charged, the net charge at the shear plane is zero due to negative/positive charge compensation. With further increase in calcium concentration, the surface attracts counterions in excess of its own nominal charge³³ and the net charge detected at the shear plane is now positive and indeed the ζ -potential reversed (Figure 3.16). OH⁻ ions in the diffuse layer balance the excess of the positive charge. Ion – ion correlations are here responsible for this overcharging and subsequent CR^{33, 50}.

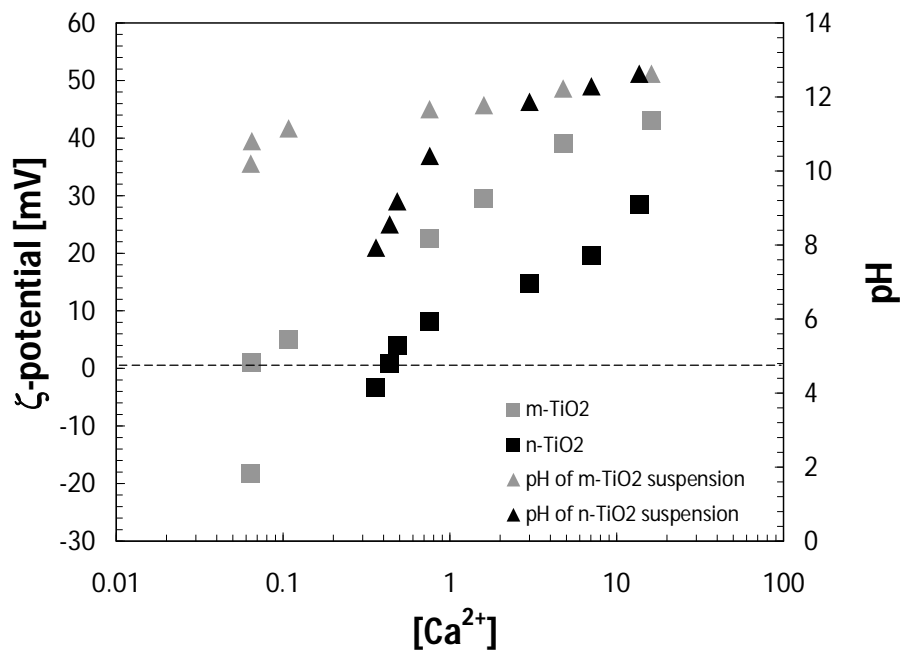


Figure 3.16 – m-TiO₂ and n-TiO₂ ζ -potentials vs [Ca²⁺].

For m-TiO₂ the process is analogous but, once again, the ionisation chemistry of the surface is affected by the presence of P – OH and not driven by Ti – OH groups only. This, together with the much smaller specific surface area, is responsible for the different IEP.

Dispersions prepared for both m-TiO₂ and n-TiO₂ at pH = 12.5 in Ca(OH)₂ solutions revealed a high instability although both the systems were far away from their own IEPs (Figure 3.17). The high level of aggregation induced by the Ca²⁺ ions is also confirmed by the good transparency of the supernatant liquid after complete sedimentation. This is the consequence of the attractive electrostatic interactions promoted by ion-ion correlations, already observed also for C-S-H (calcium silica hydrate gel) particles^{36, 38, 39}.

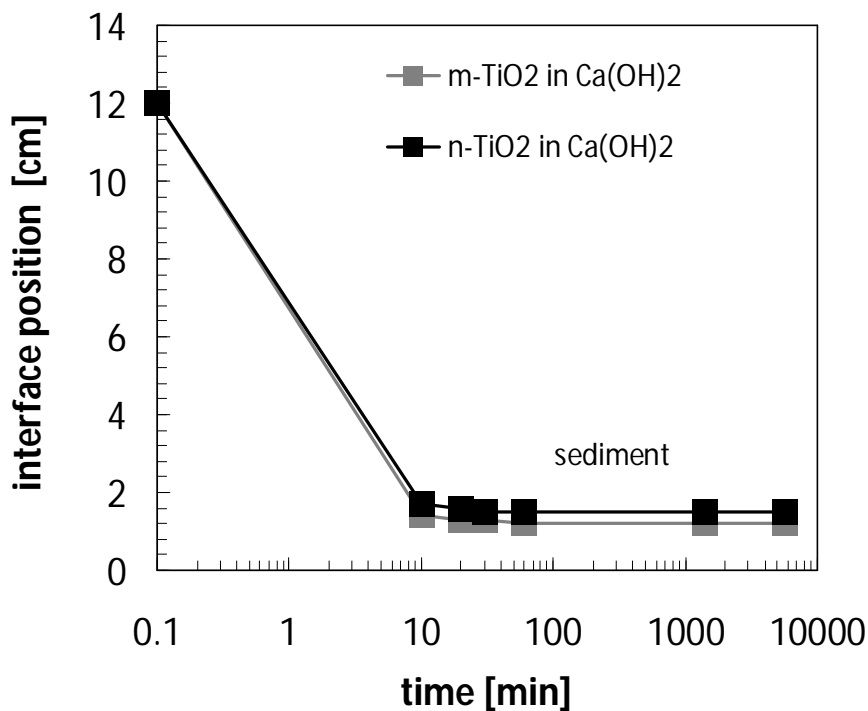


Figure 3.17 – Sedimentation test for m-TiO₂ and n-TiO₂ in Ca(OH)₂ (pH = 12.5).

3.1.2.4.4. m-TiO₂ and n-TiO₂ dispersions in the presence of SO₄²⁻

The stability of TiO₂ systems at pH = 2 in presence of SO₄²⁻ ions (H₂SO₄ solution) has been found to be very similar to the case of Ca²⁺ (Figure 3.18). Phenomena described in the previous section can be used again here to interpret the experimental evidence of dispersion reduced stability.

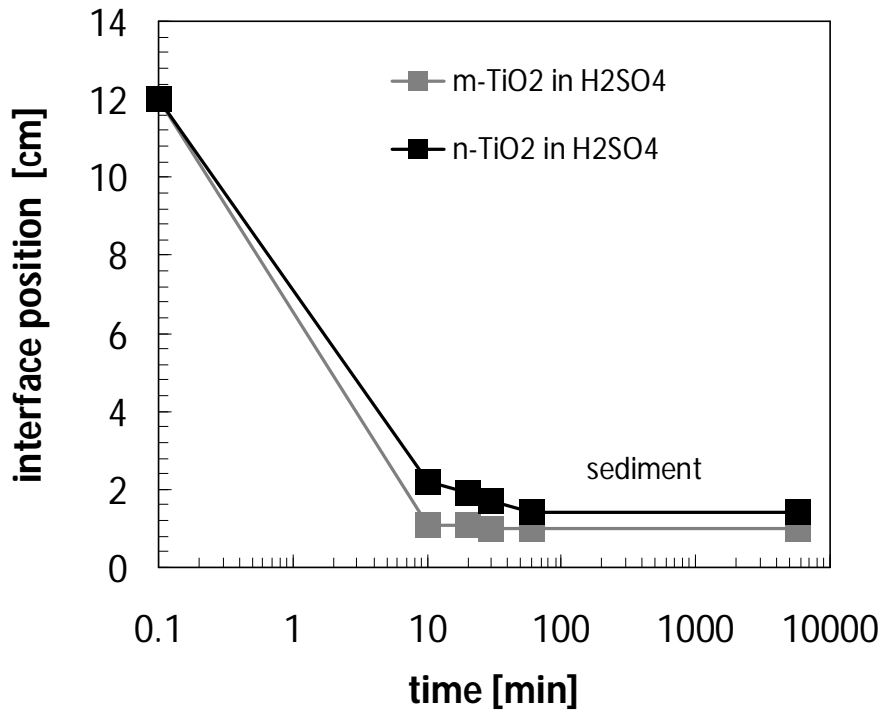


Figure 3.18 – Sedimentation test for m-TiO₂ and n-TiO₂ in H₂SO₄ (pH = 2).

3.1.2.4.5. m-TiO₂ and n-TiO₂ dispersions in the presence of Na⁺, K⁺, Ca²⁺ and SO₄²⁻, i.e. synthetic cement pore solution

The synergistic effect of all the previously discussed ions has been studied for titania dispersions in an ionic soup used to model the cement pore solution. The composition of the synthetic pore solution according to Houst et al.⁵¹, is given in Table 2.3 and accounts for a measured pH of 12.87 ± 0.02 . Neither of the two dispersions is stable in this ionic solution (Figure 3.19) and a significant sediment is formed even after 10 minutes only (similar to the H₂SO₄ and Ca(OH)₂ systems as expected). Figure 3.20 shows the appearance of such dispersions from 10 minutes to 30 minutes. The clarity of the supernatant solution and the height of the sediment give rise to interesting observations.

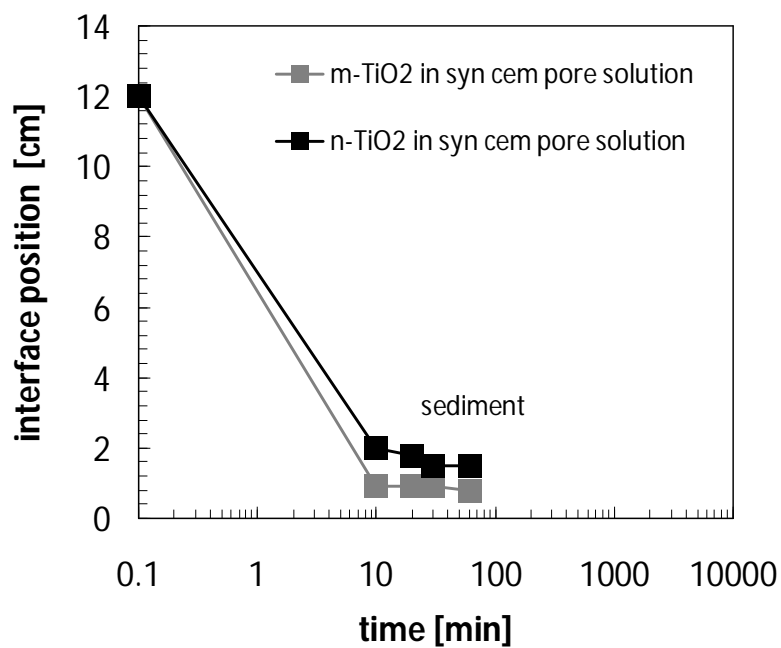


Figure 3.19 – Sedimentation test for m-TiO₂ and n-TiO₂ in synthetic cement pore solution (pH = 12.87).

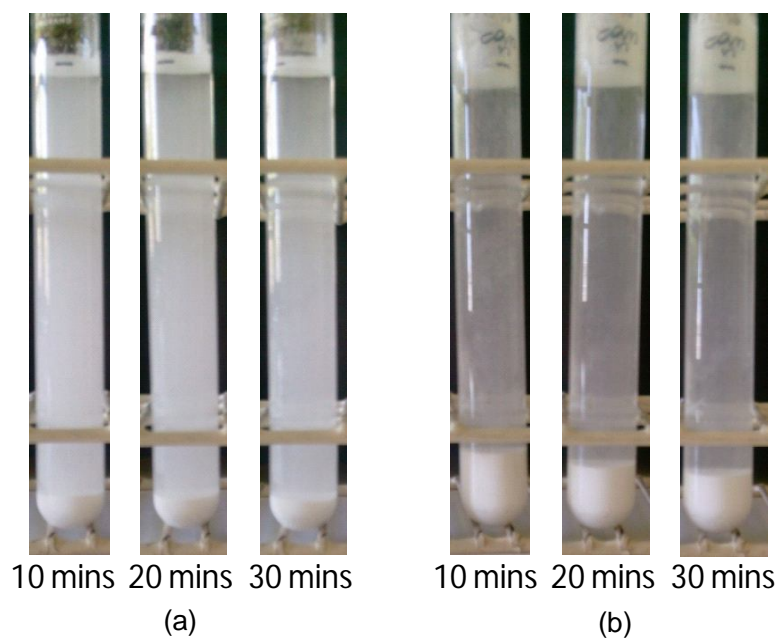


Figure 3.20 – Sedimentation test for: (a) m-TiO₂ and (b) n-TiO₂ in synthetic cement pore solution (pH = 12.87).

After 10 minutes, m-TiO₂ showed a compact and small precipitate which did not change significantly in volume with time. Furthermore the supernatant solution did not appear totally clear both at 10 minutes and at longer times. According to Shaw²⁷ this is evidence of small particle aggregates which settle very compactly (small inter-aggregate volume) and leave the supernatant solution turbid due to even smaller aggregates kept dispersed by Brownian motion (*deflocculated* sediment). On the other hand n-TiO₂ showed the opposite behaviour. The higher level of sediment formed after 10 minutes which, reduced with time, and the clearer supernatant solution (at any time) suggest bigger particle aggregates. Their bigger size prevents a compact early stage settling (higher inter-aggregate volume and consequent higher sediment height). The volume of the sediment decreases in time due to space rearrangements caused by gravity. Nevertheless the supernatant solution appears clearer at any time because the bigger aggregates are less affected by thermal motion (*flocculated* sediment). The graphical model describing these different sedimentation phenomena is shown in Figure 3.21.

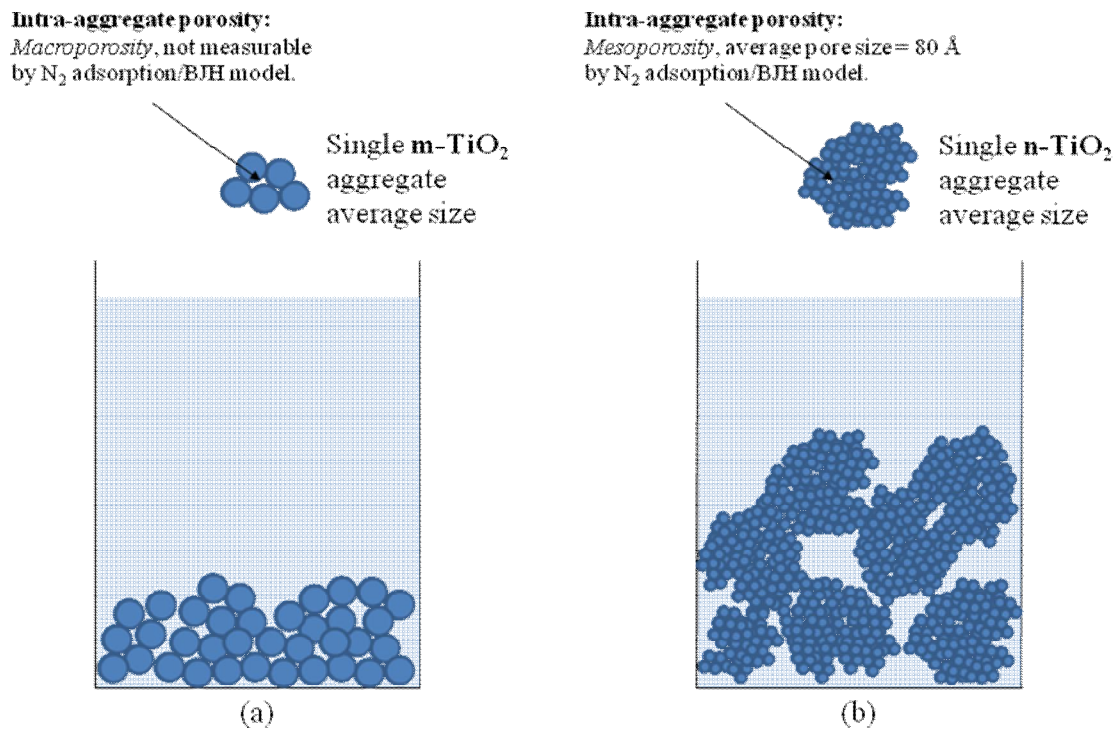


Figure 3.21 – Flocculating/deflocculating sedimentation model. (a) m-TiO₂, deflocculated sediment; (b) n-TiO₂, flocculated sediment.

3.1.3. Photocatalyst characterisation summary

As a useful reference point in the thesis and to facilitate the reader during the discussion of the photocatalytic performances in relation to the photocatalyst properties, we resume in Table 3.3 the main physico – chemical properties evaluated.

Table 3.3 – TiO₂ main physico-chemical properties investigated.

Physico-Chemical		Unit	Sample	
Property			m-TiO ₂	n-TiO ₂
Crystal phase		–	Anatase	Anatase
Band gap		<i>eV</i>	3.29 ± 0.02	3.34 ± 0.02
S _{BET}		<i>m² g⁻¹</i>	8.7	78.9
BJH Φ _{pore}		Å	> 500	79.6
Surface modification		–	P, K	None
IEP (*)		<i>pH unit</i>	2.1	6.5
PZC (#)		<i>pH unit</i>	≈ 2	6.5
	Product spec	<i>nm</i>	170	17
Particle	TEM	<i>nm</i>	153.7 ± 48.1	18.4 ± 5.0
size	XRD	<i>nm</i>	–	16.6 ± 2.0
	BET	<i>nm</i>	177.6	19.5

(*) Iso Electric Point; (#) Point of Zero Charge

3.2. Photocatalytic performance

3.2.1. Self-cleaning effect – Rhodamine B (RhB) test

The degradation of colour of RhB was quantitatively measured by light absorption as a function of wavelength by reflecting light from the cement surface on which the dye was deposited (section 2.4.1). In this way, diffuse reflectance spectra were obtained as shown in Figures 3.22, 3.23 and 3.24. The peak area of the main absorption centred around 541.5 nm is indicative of the concentration of the intact dye molecule and it can be observed that under illumination, the area reduces as a function of time, i.e. the dye molecule degrades. It can be noted that there is also degradation of colour in samples which do not contain photocatalyst and this highlights an important source of misrepresentation of catalyst efficiency where controls are not used. The loss of colour by photolytic degradation of the dye is quite common in fact; this effect is observed as coloured fabrics are bleached in sunlight. However, even by taking account of this effect, it can be shown that there is an enhanced degradation of colour in the presence of photocatalyst.

An interesting feature of these data is the shift to lower wavelengths of absorption maxima exhibited by samples which experienced exposure to daylight during the dye deposition step. This feature is not reproduced when dye is deposited in the dark. A similar effect (hypsochromic shift) was observed by Chen et al ²³, who discriminated between different degradation mechanisms as a function of the different illumination conditions experienced. The lower energies available from visible light are insufficient to induce photo-activation of TiO₂ but they can lead to dye sensitisation and degradation of colour by this mechanism (Figure 3.25(b)). As a result, the selective stepwise de-ethylation of RhB amino groups, responsible for the hypsochromic shift ²³, leads to a sequence of structurally similar degradation products which absorb radiation at progressively lower wavelengths. Where samples were prepared in the dark, the only light exposure was to UV radiation which promotes true photocatalytic processes and reduces the hypsochromic effect (3.25(a)). Clearly, degradation mechanisms are important in understanding optimisation of photocatalyst efficiencies. However, it is evident from the above that photocatalysis can encompass more than one process.

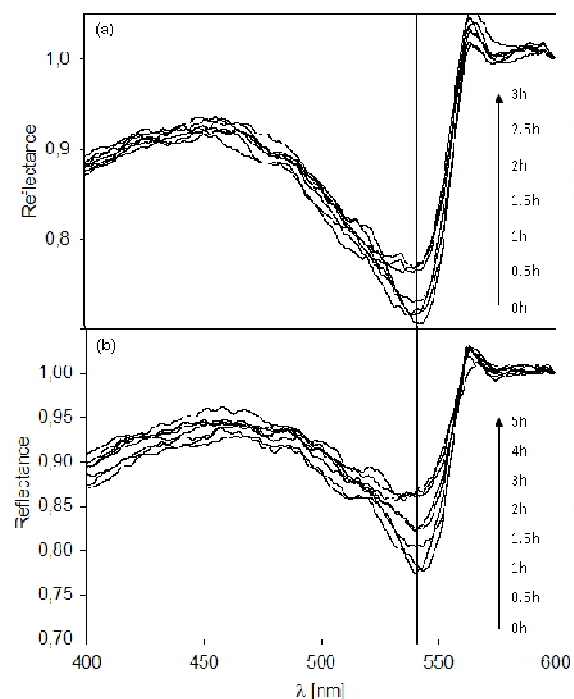


Figure 3.22 – Diffuse reflectance spectra at various illumination time for white cement pastes without photocatalyst: (a) RhB deposition and conditioning under daylight, (b) RhB deposition and conditioning in darkness.

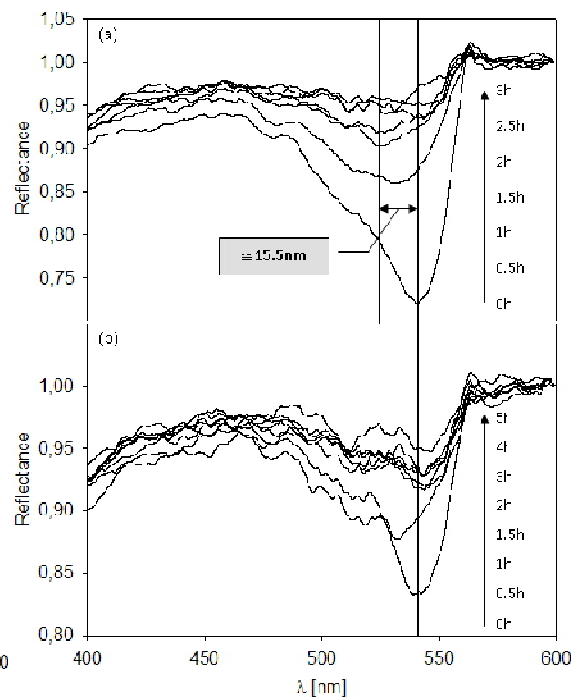


Figure 3.23 – Diffuse reflectance spectra at various illumination time for white cement pastes containing m-TiO₂: (a) RhB deposition and conditioning under daylight, (b) RhB deposition and conditioning in darkness.

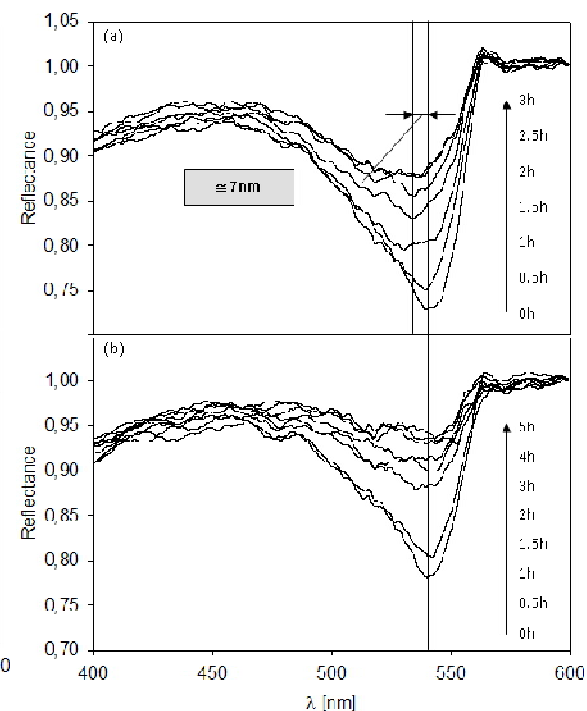


Figure 3.24 – Diffuse reflectance spectra at various illumination time for white cement pastes containing n-TiO₂: (a) RhB deposition and conditioning under daylight, (b) RhB deposition and conditioning in darkness.

Whilst UV exposure promotes conventional photocatalysis-induced redox processes on the surface of TiO_2 , diagnosis of reaction pathways is complicated by the dye sensitisation mechanism and the influence of resulting products. A further physical implication is the particle size of the photocatalyst. The dye sensitisation route would appear to be less dependent on the normally expected nano-dimensionality of the catalyst because charge recombination effects must be less significant, i.e. degradation is not dependent on the production of electron-hole pairs. It is therefore difficult to reconcile higher degradation rates for RhB on micro-sized TiO_2 , with conventional photocatalytic mechanisms and the dominant effect under the conditions used in the study must therefore be correlated to other physical – chemical properties of the photocatalyst particles in the cement environment.

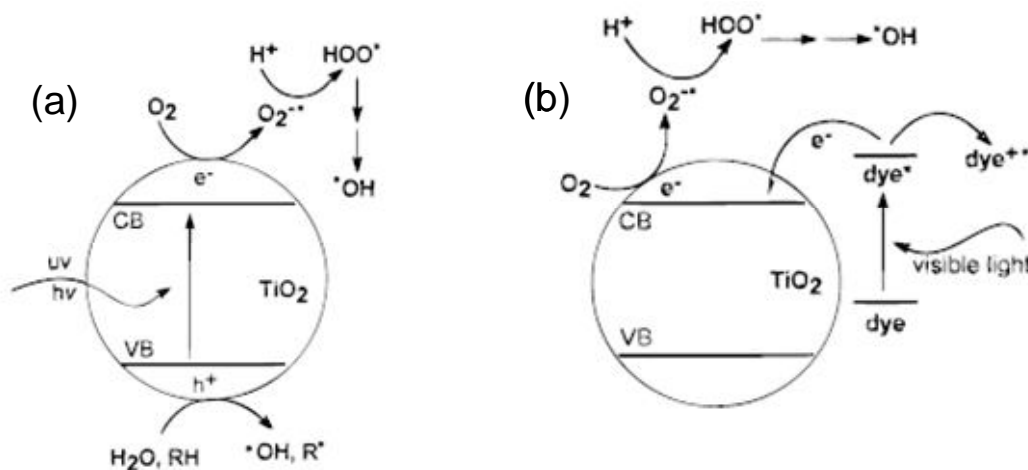


Figure 3.25 – RhB- TiO_2 system under: (a) U.V. light irradiation: *photo-sensitised* pathway²³; (b) visible light irradiation: *dye-sensitised* pathway²³.

These results have been presented at the 13th *International Conference on TiO_2 photocatalysis: fundamentals and applications*, San Diego CA, USA, 2008 and published in A. Folli, U. H. Jakobsen, G. L. Guerrini and D. E. Macphee, *J. Adv. Oxid. Technol.*, 2009, **12**, 126-133⁵².

3.2.2. Depollution – NO_x oxidation test and modelling

3.2.2.1. NO_x oxidation test with mortar specimens

Figures 3.26 (a), 3.26 (b) and 3.26 (c), show the nitric oxide, NO, concentration profiles obtained during the NO_x oxidation test at three different flow rates and under illumination (section 2.4.2.1). In each graph trends obtained with photocatalytic cement mortars (either with m-TiO₂ or n-TiO₂) are compared to trends exhibited by TiO₂-free white cement mortars. The flat character of profiles where TiO₂ is not present indicates very low impact on NO oxidation by the cement environment itself. Trends also suggest that the lower the flow rate the lower the NO concentration at 90 minutes (assumed as pseudo steady concentration), hence the higher the conversion.

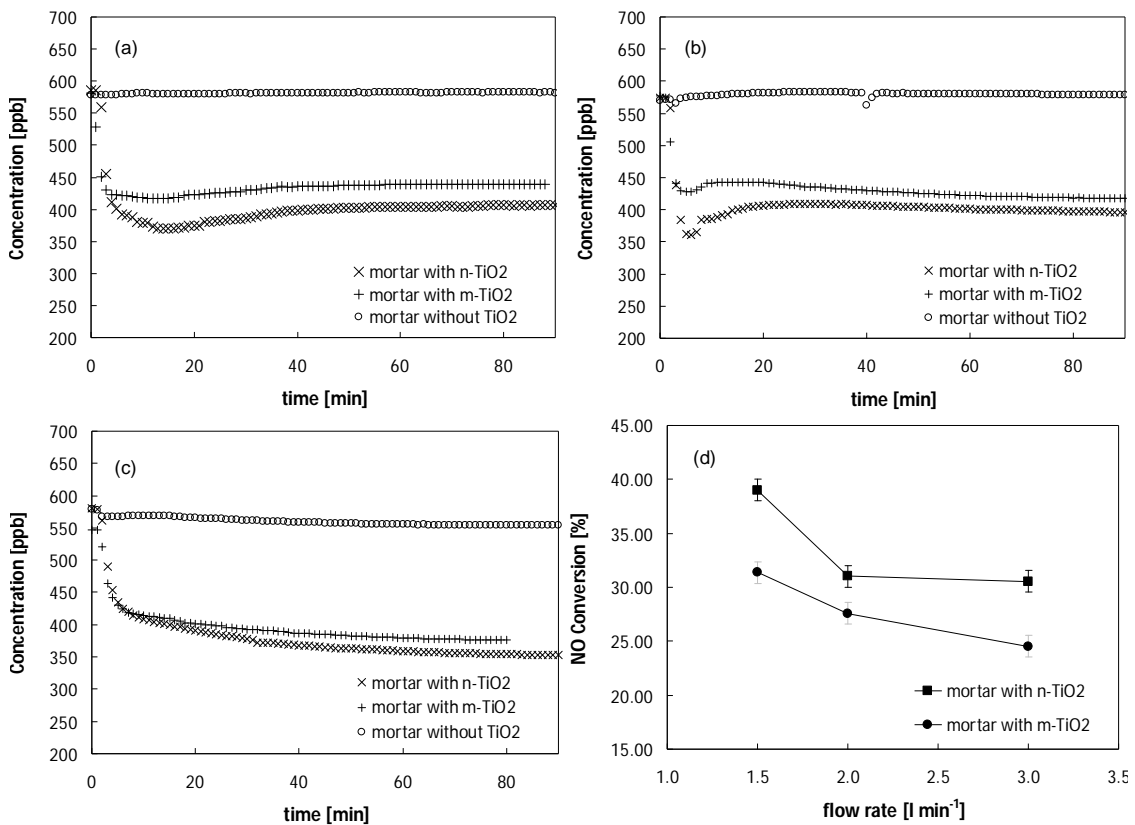


Figure 3.26 – NO concentration profiles at: (a) 3 l min⁻¹, (b) 2 l min⁻¹, (c) 1.5 l min⁻¹. (d) NO conversion versus flow rate.

The photocatalytic oxidation of NO on pure TiO₂ is a complex series of chemical equilibria as described in section 1.1.1. Adsorbed H₂O and O₂ react with valence band positive holes and conductance band electrons respectively, generating adsorbed hydroxyl radicals, HO·,^{53, 54}. These radicals directly react with NO and, according to another series of chemical equilibria, they convert NO into nitric acid, HNO₃, passing through unstable nitrous acid, HONO and nitrogen dioxide, NO₂^{53, 54}. This general reaction mechanism can still support NO oxidation over TiO₂ in the cement environment but due to the very high pH typical of cementitious materials, the reaction products and intermediates are likely to be associated with nitrates, NO₃⁻, and nitrites, NO₂⁻, rather than nitric and nitrous acids. Nevertheless, a few questions are still unanswered; for instance, the potential negative impact on the cementitious structure of the acidic species produced. OH⁻ present in cement (mainly in cement pore solution) buffer the acidic species formed during the oxidation of NO, i.e. HONO and HNO₃. Once this buffer capacity is no longer sustained by the alkaline liquor in the pores, the formed acidic species might further decrease the pH of the system below the stability limit of the C-S-H phase (around 11.5⁵⁵) and therefore promote decalcification of the latter. This issue is relevant in terms of durability of the cementitious structure. An accurate mass balance is therefore required to quantitatively assess the impact of photocatalytic oxidation products but this is complex and evidence for such calculations has not yet been found.

The NO concentration after 90 minutes (assumed as pseudo steady conversion) versus flow rate is reported in Figure 3.26 (d) for both white cement mortars containing m-TiO₂ and white cement mortars containing n-TiO₂. A comparison between the two trends suggests that n-TiO₂ generally performs better than m-TiO₂. Indeed for all the gas flow rates investigated, the NO conversion exhibited by mortars containing n-TiO₂ is higher than mortars containing m-TiO₂. In this case, results are in agreement with what is expected on the basis of the different specific surface areas of the two TiO₂ powders. Note however that specific surface areas failed to explain the higher activity towards RhB degradation exhibited by samples containing m-TiO₂.

3.2.2.2. Overall kinetics of photocatalytic oxidation of NO

n-TiO₂ (the better performing of the two catalysts in oxidising NO) has been deposited on the surface of glass beads and used in a further study (section 2.4.2.3) to highlight the role of TiO₂ surface water in the photocatalytic oxidation of NO as well as the reaction regimes and possible deactivation phenomena. An image of a typical n-TiO₂ coated glass beads is shown in Figure 3.27.

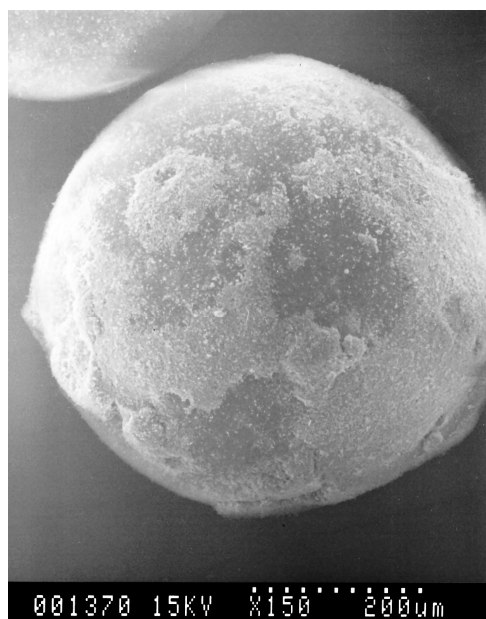


Figure 3.27 – SEM micrograph of an n-TiO₂ coated glass bead.

Two preliminary *blank* tests (Figure 3.28 and 3.29) indicated no significant NO conversion due to the effect of UV light in the absence of TiO₂ and no reaction with adsorbed species on TiO₂ surface in the darkness, respectively was observed. Pseudo steady state conversions for sample GB20 have been studied at two different gas flow rates, 50 and 100 ml min⁻¹, and two different initial NO concentrations, 50 and 25 ppm, to derive kinetic constant and NO adsorption coefficient for assumed Langmuir – Hinshelwood (L–H) kinetics.

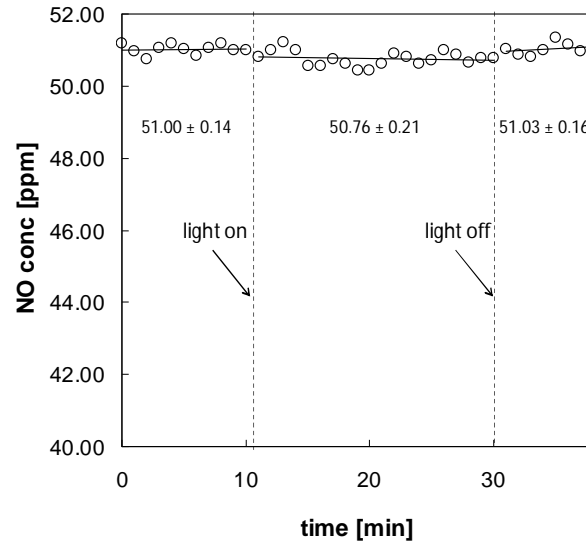


Figure 3.28 – Effect of photolysis on NO (only uncoated glass beads present).

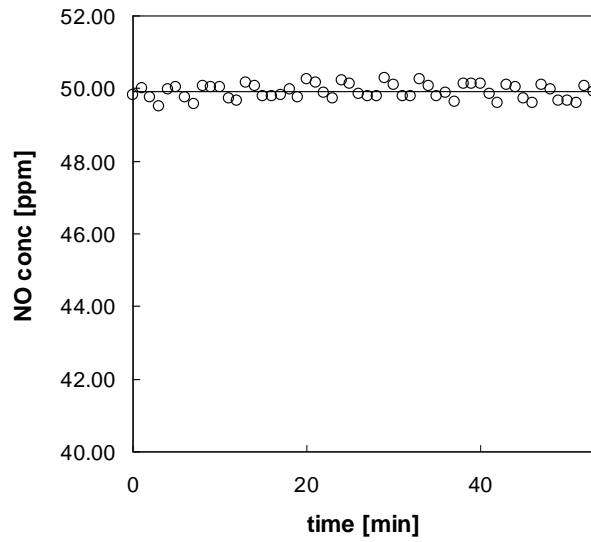


Figure 3.29 – Effect of the adsorbed water on NO oxidation in the dark.

The superficial velocity in the reactor, u , and the average gas transit time, τ , can be calculated according to Equations 3.18 and 3.19:

$$u = \frac{F}{S} \quad (3.18)$$

$$\tau = \frac{L}{u} \quad (3.19)$$

where: F is the gas flow rate, S the bed cross section, equal to 3.14 cm^2 (2 cm diameter) and L , the illuminated bed depth, equal to 0.2 cm, i.e. the total bed thickness. This assumption is valid since the photocatalytic bed is constituted by TiO_2 coated glass beads and not TiO_2 powder^{56, 57}. u is then used to derive the axial Peclet number, Pe_a , product of Reynolds number and Schmidt number according to Equation 3.20:

$$\text{Pe}_a = \frac{uL}{D_e} \equiv \text{Re} \cdot \text{Sc} \quad (3.20)$$

where D_e is the diffusion coefficient of NO in air, equal to $0.151 \text{ cm}^2 \text{ s}^{-1}$.

Table 3.4 – Fix bed reactor fluid dynamic parameters.

Sample	F $ml \text{ min}^{-1}$	u $cm \text{ s}^{-1}$	τ ms	Pe_a -
GB20	50	0.265	755	0.35
GB20	100	0.531	377	0.70

Table 3.4 summarizes results obtained for u , τ and Pe_a for the two different flow rates investigated. The Peclet number represents the ratio between convective (uL) and diffusive transport (D_e). In the photocatalytic bed here considered the axial Peclet numbers for both the gas flow rates adopted are below 1, i.e. diffusion prevails over convection. The reactor does *not* have plug flow behaviour: NO concentration profile inside the fixed bed is flat and does not depend on the distance (length of the fixed bed). Therefore it can be treated as a simpler continuous stirred tank reactor (CSTR) or well – mixed reactor. Combining the mass balance for a CSTR in Equation 3.21:

$$F(C_{NO,in} - C_{NO,out}) = Vr \quad (3.21)$$

with the L–H kinetics in Equation 3.22:

$$\frac{kK C_{NO,out}}{1 + K C_{NO,out}} = r \quad (3.22)$$

the following expression is derived:

$$\frac{\tau}{C_{NO,in} - C_{NO,out}} = \frac{1}{kKC_{NO,out}} + \frac{1}{k} \quad (3.23)$$

where: r is the reaction rate, $C_{NO,in}$ is the NO concentration at the entrance of the photocatalytic bed and therefore equal to the initial concentration of NO in the gas stream, either 50 or 25 ppm, $C_{NO,out}$ is the concentration at the exit of the photocatalytic bed, k the kinetic constant and K the L–H adsorption coefficient. From the linear regression using Equation 3.23 ($R^2 = 0.998$), we observed the following overall constants: $k = 3.02 \cdot 10^{-4} \text{ mol m}^{-3} \text{ s}^{-1}$ and $K = 1.24 \cdot 10^3 \text{ m}^3 \text{ mol}^{-1}$. These values are in good agreement with data already present in literature^{53, 54} and provide solid evidence that, with the reactor used, the photocatalytic oxidation of NO follows the same kinetics already observed by other authors^{53, 54}. This has been considered as a validation to justify the reliability of our further conversion data.

3.2.2.3. Surface hydration, N mass balance and regimes of NO oxidation

Figure 3.30 shows the outlet NO, NO₂ and NO_x ($C_{NOx} = C_{NO} + C_{NO_2}$) gas phase concentration profiles for n-TiO₂ coated glass beads irradiated with UVA light with an inlet NO/air gas stream at 50 ml min⁻¹ and NO concentration equal to 50 ± 0.5 ppm. Three *light on – off* cycles were monitored for each of the three samples.

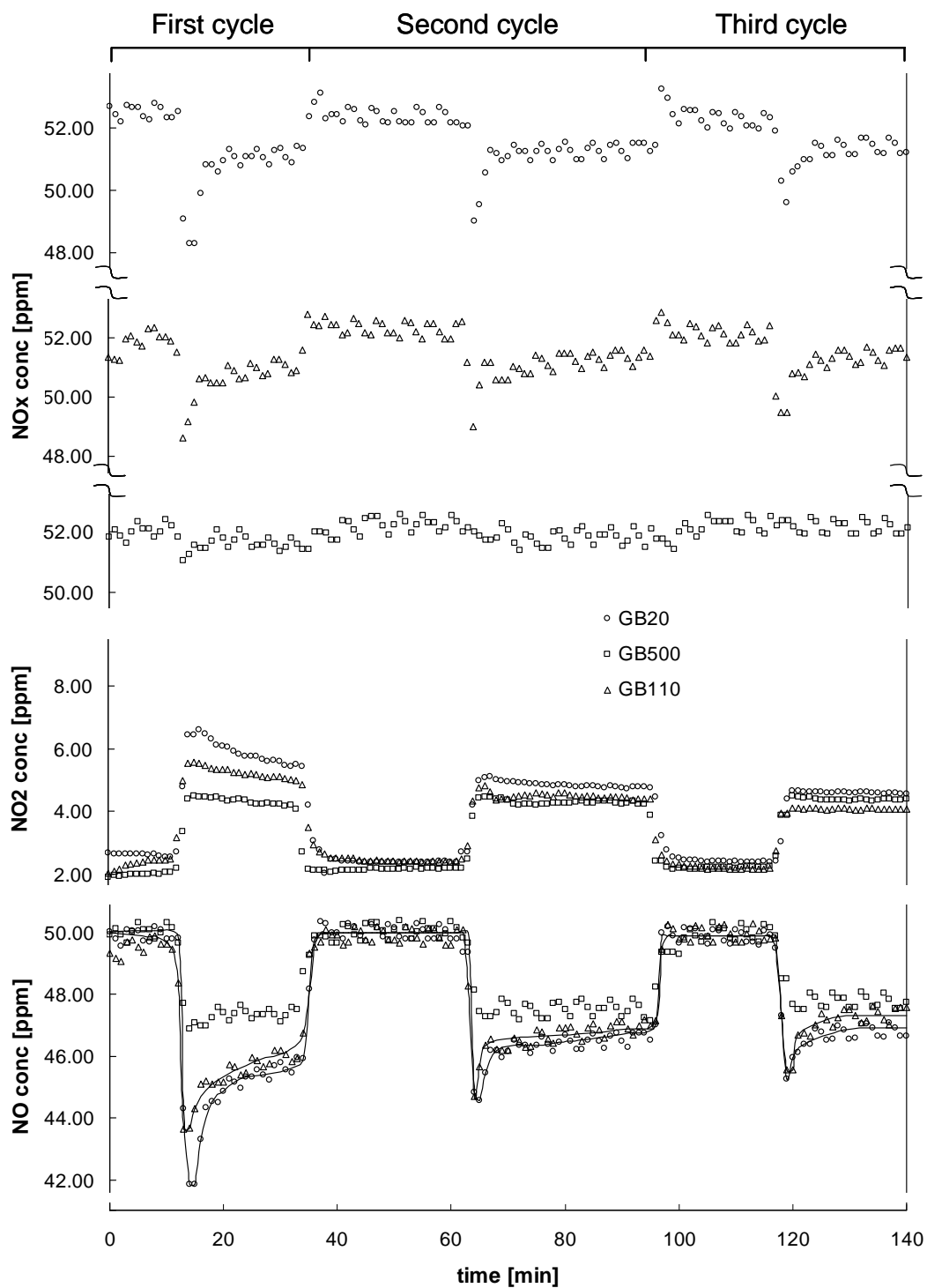


Figure 3.30 – NO, NO₂ and NO_x concentration profiles.

Before the first cycle, NO gas was flowed through the reactor in the dark until TiO₂ surfaces were saturated (i.e. until $C_{\text{NO,out}} = C_{\text{NO,in}}$). When light was switched on, the initial

drop in NO concentration was 8.2 ppm for GB20, 6.3 ppm for GB110 and 3.1 ppm for GB500, generating a well resolved peak for GB20 and GB110 but a very small one for GB500. This initial NO removal appears to follow the same decreasing trend as is observed for the initial TiO₂ surface hydration as a function of increasing temperature, i.e.: GB20 > GB110 > GB500 (Figures 3.5 and 3.31).

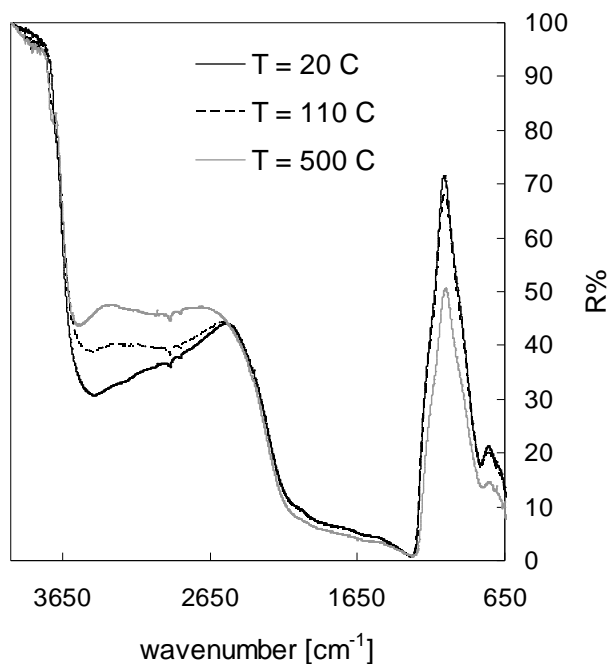


Figure 3.31 – DRIFT spectra of n-TiO₂ coated glass beads at 20 °C, 110 °C and 500 °C.

NO₂ concentrations achieved a maximum value corresponding with the minimum in NO but do not account for the total NO loss in the gas phase. Indeed the NO_x balance showed a drop with peaks similar to the NO profiles. A possible mechanism, consistent with these observations, is shown in Figure 3.32.

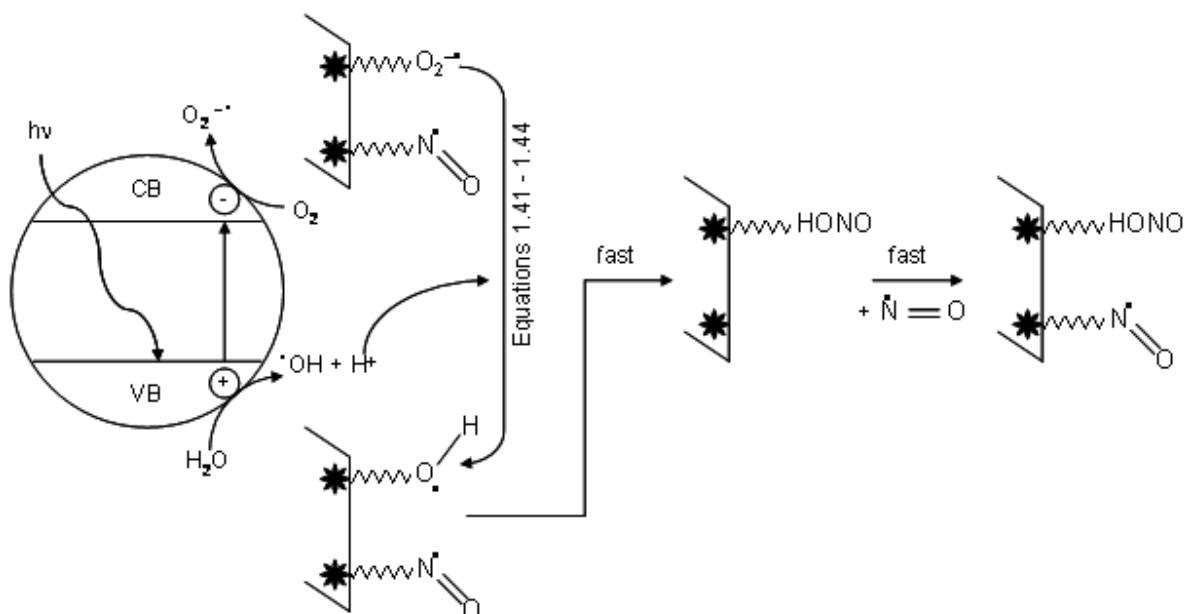


Figure 3.32 – NO photoadsorption on light activated TiO₂ (* adsorption site; \\\\ undefined bond).

When light is turned on, •OH radicals are formed from the interaction between water and photogenerated positive holes (Equation 1.39, donor route) and also via oxygen and photogenerated electrons (Equations 1.40 – 1.44, acceptor route). This latter route however is kinetically disadvantaged compared to the donor route because the transfer of the photogenerated electron to the adsorbed molecular oxygen is the slowest amongst all of the TiO₂ charge transfer processes (Equation 1.40 and Equation 1.55 in Table 1.8 that we show again here to facilitate the reader). The adsorbed NO reacts very quickly with the adsorbed •OH radicals forming the HONO adduct (Figure 3.32). An active site is now vacant and further NO is adsorbed at a higher rate than the conversion of HONO to NO₂. The oxidation of HONO (and/or NO₂⁻) to NO₂ (at this early stage in the cycle considered slower than NO adsorption) depends also on the content of water since the initial NO₂ formation follows the same decreasing trends as are observed for surface hydration, i.e.:

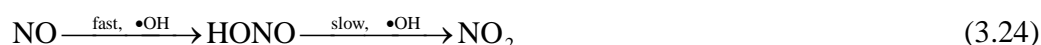
$$C_{\text{NO}_2, \text{GB20}} = 6.59 \text{ ppm} > C_{\text{NO}_2, \text{GB110}} = 5.53 \text{ ppm} > C_{\text{NO}_2, \text{GB500}} = 4.50 \text{ ppm}.$$

Table 1.8 – Primary processes and associated characteristic time domains in the TiO₂-sensitized photoreactions⁵⁸. (*) Characteristic time for this reaction refers to organic molecules only. No data available for NO.

Primary process	Equation	Characteristic time
Charge carrier generation		
$\text{TiO}_2 + h\nu \longrightarrow \text{h}^+ + \text{e}^-$	(1.48)	fs (very fast)
Charge carrier trapping		
$\text{h}^+ + \text{Ti}^{\text{IV}}\text{OH} \longrightarrow \{ \text{Ti}^{\text{IV}}\text{OH}^\bullet \}^+$	(1.49)	10 ns (fast)
$\text{e}^- + \text{Ti}^{\text{IV}}\text{OH} \longleftrightarrow \{ \text{Ti}^{\text{III}}\text{OH} \}$	(1.50)	100 ps (shallow trap, dynamic equilibrium)
$\text{e}^- + \text{Ti}^{\text{IV}} \longrightarrow \text{Ti}^{\text{III}}$	(1.51)	10 ns (deep trap)
Charge carrier recombination		
$\text{e}^- + \{ \text{Ti}^{\text{IV}}\text{OH}^\bullet \}^+ \longrightarrow \text{Ti}^{\text{IV}}\text{OH}$	(1.52)	100 ns (slow)
$\text{h}^+ + \{ \text{Ti}^{\text{III}}\text{OH} \} \longrightarrow \text{Ti}^{\text{IV}}\text{OH}$	(1.53)	10 ns (fast)
Interfacial charge transfer		
$\{ \text{Ti}^{\text{IV}}\text{OH}^\bullet \}^+ + \text{org} \longrightarrow \text{Ti}^{\text{IV}}\text{OH} + \text{ox org}$	(1.54)	100 ns (slow) (*)
$\{ \text{Ti}^{\text{III}}\text{OH} \} + \text{O}_2 \longrightarrow \text{Ti}^{\text{IV}}\text{OH} + \text{O}_2^{\bullet-}$	(1.55)	ms (very slow)

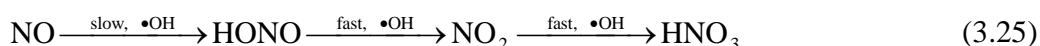
The proposed mechanism of a fast NO reactive *photoadsorption* and a slower initial conversion to NO₂ is consistent with: i. the dependency of the area of the adsorption peaks (Figure 3.30) on the extent of surface hydroxylation (molecular and dissociated surface water) exhibited by GB20, GB110 and GB500; ii. the light – assisted formation of surface ·OH radicals through water and light generated positive holes being a very fast process (Equation 1.49, Table 1.8)⁵⁸, iii. the Langmuir – Hinshelwood kinetics used previously and employed by other authors^{53, 54, 59}.

Summarizing the entire initial mechanism in a single equation, we obtain:



Equation 3.24 is consistent with what Devahasdin et al.⁵³ hypothesised as a general *initial regime* or *fast initial adsorption plus reaction*.

After this initial stage, the NO conversion decreases significantly for GB20 and GB110. GB500 shows only a very small variation. NO₂ concentration in this period of time decreases. This is a typical feature of transient behaviour where NO conversion to HONO is the rate determining step and NO₂ is an intermediate which is subsequently oxidised. The final product is HNO₃ / NO₃⁻:



Once again the NO₂ profiles and the NO_x balance provide information on the role of surface water. The rate of conversion of NO₂ (slope of the concentration profile) seems to depend again on the amount of ·OH radicals, hence water, on the surface since it follows the usual trend GB20 > GB110 > GB500, suggesting also greater amount of nitrates formed for GB20. NO_x balance confirms this hypothesis. Throughout the first cycle, NO_x balance in the gas phase does not reach the initial value in the dark and the deficit related to the missing N in the gas phase, considered equal to the amount of NO₃⁻ formed and adsorbed on the TiO₂ surface, is: 0.41 μmol m⁻² for GB20, 0.36 μmol m⁻² for GB110 and 0.16 μmol m⁻² for GB500.

When light is turned off after the first cycle, the reaction quenches immediately. NO and NO₂ concentrations return to the initial values and NO_x balance in the gas phase reaches 100 %. The quick character of the initial concentration recovery (experienced also after the second cycle) when light is switched off is clear evidence and further proof that photocatalytic oxidation of NO is a radical – based process.

In the second and third light off – on cycles, we note the same observations as for cycle 1. When light is turned, a fast NO reactive photoadsorption occurs with generation of NO₂ which approaches the transient period summarized by Equation 3.25. However, from cycle to cycle, we can observe that, for GB20 and GB110:

- i. the area of the peak related to the initial fast reactive photoadsorption of NO continuously decreases from cycle to cycle;

ii. NO concentration monotonically increases while NO₂ concentration monotonically decreases; despite the fact that GB20 shows generally lower NO concentration and higher NO₂ concentration than GB110 (lower water content), the differences between the two samples become smaller as a function of number of cycles.

For GB500, the much reduced amount of water (molecular and dissociated) on the surface minimises considerably the effects observed for GB20 and GB110. The very small peak corresponding to fast reactive photoadsorption of NO experienced in the first cycle disappears completely in the following two. NO and NO₂ concentrations remain quite constant in the second and third cycles with good NO_x balance in the gas phase that suggests very low amount of nitrates formed in the first cycle, even less in the second and no measurable nitrates in the third (concentration of total NO_x in the gas phase in the dark is equal to that during illumination, i.e., the balance approximates 100 % with NO and NO₂ only).

This evidence is likely to be attributed to *deactivation* of the reactive surface by means of: water consumption during the reaction (which is not continuously supplied through the gas feed) and *irreversible adsorption* of nitrates which reduces the number of available adsorption sites.

Integration of the gaps in the NO_x balance can provide a quantitative view of the deactivation phenomena described above. Figure 3.33 shows the progressive reduction of specific surface area for the three batches due to nitrate formation, under the assumptions that: i. all the NO_x missing in the gas phase can be accounted for as NO₃⁻ formation; ii. NO₃⁻ does not desorb from the TiO₂ surface; iii. the average radius of NO₃⁻ is 1.96 Å⁶⁰. According to quantitative data shown in Figure 3.33, the deactivation of active sites due to adsorbed nitrates and consequent reduction in available surface area is occurring but the amount of available surface area is significantly still very high after a total illumination period of about 80 minutes. Therefore in this period of time, the consumption of water (molecular and dissociated) in the reaction might play a major role in the overall deactivation. The apparent absence of nitrate formation observed for GB500 in the third cycle is not completely understood yet, however different hypothesis

may be provided. Devahasdin et al.⁵³ observed no nitrate formation with NO₂ as the final oxidation product once all the sites responsible for NO₃⁻ formation are irreversibly occupied. Although this is likely to be the case after many hours of activity, in our conditions the available surface area is still high and it is difficult to reconcile this behaviour with occlusion of all the active sites. We propose alternatively that oxidation to nitrate is inhibited by the low availability of surface water, allowing oxidation of NO only to NO₂ and not further.

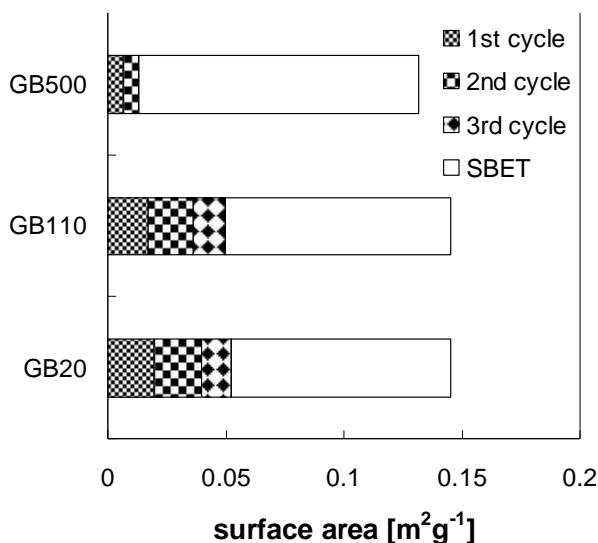


Figure 3.33 – Surface area loss due to NO₃⁻ formation and adsorption compared to the total BET specific surface area (data referred to the TiO₂ – coated glass beads).

Data obtained by integration of the areas related to the NO_x balance can also be used to plot the total amount of NO_x lost from the gas phase (considered equal to the total amount of NO₃⁻ formed) over the three cycles versus the water loss due to the pre-treatment that GB110 and GB500 experienced (Figure 3.34). Even though more data points are necessary to identify a better trend, Figure 3.34 suggests that, although the absolute amount of water lost between GB20 and GB110 is similar to the amount lost between GB110 and GB500, the total number of moles of NO₃⁻ produced by the latter is significantly lower. The reason might be found in the nature of water removed. DRIFT spectra showed that between 20 °C and 110 °C, H – bonded molecular water is removed; between 110 °C and 500 °C it is chemisorbed water (molecular and dissociated) which leaves the surface. Figure 3.34 therefore highlights that in the photocatalytic formation of

NO_3^- , chemisorbed water is much more active than H – bonded molecular water. This can be considered as further experimental justification for the use of a Langmuir – Hinshelwood kinetic model (L-H kinetics implies both reactants being first adsorbed).

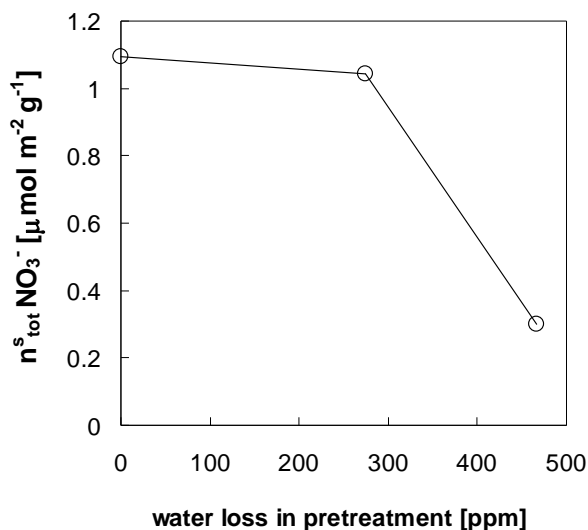


Figure 3.34 – Effect of initial water content on total moles of NO_3^- formed on TiO_2 surface.

3.2.2.4. Synergistic effect of the couple $\text{H}_2\text{O} - \text{O}_2$

Hashimoto et al.⁵⁹ proved that NO can also be oxidised, on light irradiated TiO_2 surfaces, by superoxide radicals, $\text{O}_2^{\cdot-}$ (Equation 3.31). Although our analysis focused on the effect of surface water and the data do not allow us to discriminate the contribution of adsorbed oxygen, this extra oxidation route through superoxide species must be active under our conditions as well and therefore contribute to the overall NO conversion. Since the generation of $\cdot\text{OH}$ radicals from molecular oxygen depends on the amount of water present (synergistic effect of $\text{H}_2\text{O} - \text{O}_2$; O_2 needs the protons exchanged by the reaction of water with positive holes - Equation 1.39), NO photocatalytic oxidation under conditions of water deficiency (GB500) might be characterised by a larger contribution of the superoxide route. This idea seems to fit quite well with the flat NO and NO_2 concentration profiles measured for GB500.

Finally, independent on the actual oxidising species that H_2O and O_2 produce, their coupling is necessary to sustain the activation of the photocatalyst since they are responsible for trapping and/or transferring the photogenerated charge carriers (conduction band electrons and valence band positive holes) that would otherwise promptly recombine. Significant removal of one of the two species (like in our case comparing GB20 with GB500) can therefore decrease the overall activity due to much higher levels of electron – hole recombination.

3.2.3. Influence of particle agglomeration/dispersion on photocatalytic performance: a surface chemistry approach

3.2.3.1. *TiO₂ dispersion in hardened cement: a particle aggregation model*

Results obtained for TiO_2 dispersions in synthetic cement pore solutions can be used to predict behaviour and properties of the two different titanias in a real cement environment. During the preparation of cement paste specimens (see section 2.3.1), cement, water and TiO_2 are mixed together by mechanical stirring as described in the experimental section. Hydration of cement powder quickly produces a liquor with composition and pH very similar to the ion soup identified in section 3.1.2.4.5. In such conditions, considering also that TiO_2 does not take part in any of the chemical reactions forming cement hydrated phases, it is assumed that m- TiO_2 and n- TiO_2 undergo aggregations as described in section 3.1.2.4.5. Mechanical stirring distributes particle aggregates all over the forming material. Once the cement has completely hardened the dispersion of the two TiO_2 s can be predicted according to the model shown in Figure 3.35. For an equal mass of TiO_2 introduced into cement, m- TiO_2 is expected to have smaller and better dispersed aggregates than n- TiO_2 for which aggregates are bigger and more difficult to spread.

Validation of this qualitative model has been carried out by SEM-EDS investigation on real cement paste specimens containing either m- TiO_2 or n- TiO_2 . Micrographs in Figure

3.36 were obtained for the surface layer of the cement samples (1 day cured) prepared with m-TiO₂ (Figure 3.35(a)) and n-TiO₂ (Figure 3.35(b)) whilst micrographs in Figure 3.37 are of sections cut perpendicularly to the surface and show the layers beneath the surface. Surface micrographs (Figure 3.36) show a higher degree of m-TiO₂ dispersion (white spots in Figure 3.36(a)). Cement prepared with nanosized n-TiO₂ show larger particle aggregates (a lower degree of dispersion (see Figure 3.36(b))). This is especially evident when the scale of the micrograph is considered. Nanoparticulate agglomerates seem to be at least 1 µm in dimension compared to m-TiO₂ agglomerates which seem to be smaller and divided into smaller sub-agglomerates. A similar situation is achieved in the bulk of the specimens, Figure 3.37. Figure 3.37(a), related to cement prepared with m-TiO₂, shows smaller and better dispersed TiO₂ particle aggregates compared with n-TiO₂-containing pastes, Figure 3.37(b). These results, also illustrated as Ti-element maps (Figure 3.38) of 14 day cured cements, are in perfect agreement with the model proposed in Figure 3.35.

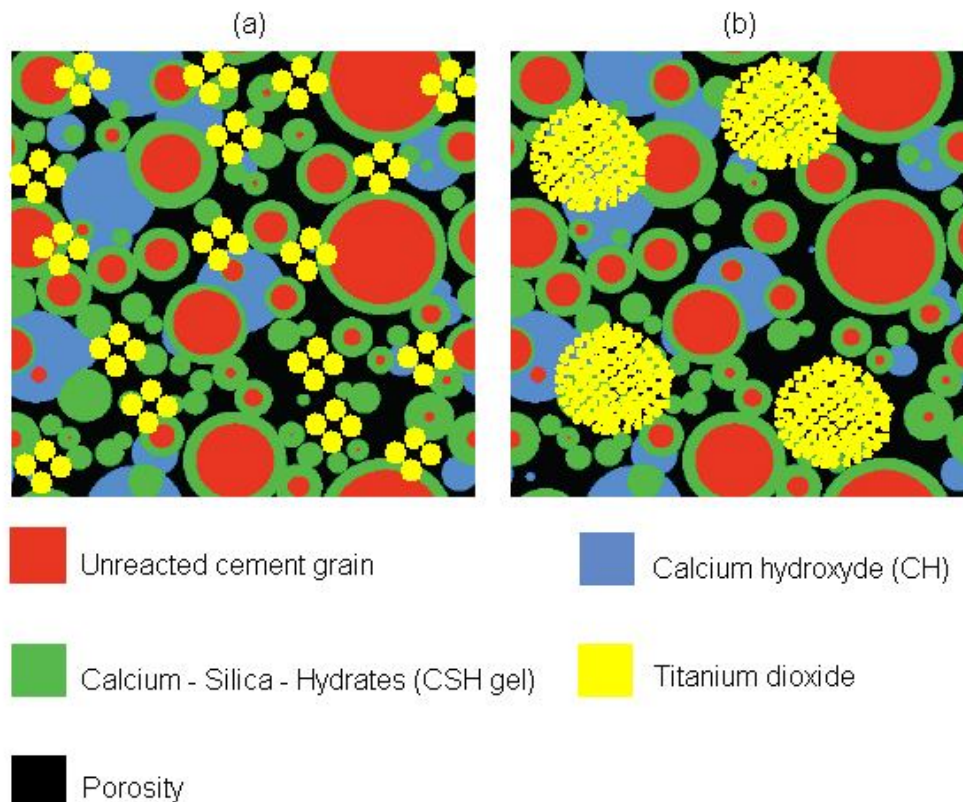


Figure 3.35 – Hardened cement structures with: (a) m-TiO₂ and (b) n-TiO₂.

3.2.3.2. *Impacts on photocatalytic performances*

Knowledge acquired through the study of titania surface chemistry can be used to modulate the overall photocatalytic activity of Portland cement containing TiO_2 . In simple slurry conditions indeed, n- TiO_2 is supposed to perform better than m- TiO_2 due to its much higher specific surface area. This is not always true in solid materials like cement where TiO_2 is highly agglomerated and the adsorption of target molecules depends on the 3D structure of the material, its porosity and, not least, the TiO_2 agglomerates porosity. In section 3.2.1, we highlighted that the degradation of Rhodamine B on the same cement specimens under UV light (a common test for the evaluation of the self-cleaning effect of photocatalytic concretes), was more efficient in the case of cement prepared with m- TiO_2 rather than n- TiO_2 . On the other hand, studies on degradation of NO_x (NO and NO_2)⁶¹ in similar specimens with UV light, showed better results using n- TiO_2 . Large molecules like Rhodamine B, with an average molecular diameter of about 1.6 nm⁶², can penetrate only with difficulty the interior of a n- TiO_2 cluster (pore size around 8 nm), but readily can access m- TiO_2 clusters (see Table 3.2). The smaller and better dispersed m- TiO_2 clusters on the surface of the specimens (Figure 3.36(a)) together with their macropores (Table 3.2), offer a higher *available* surface area for adsorption and consequent reaction of big molecules like Rhodamine B than the bigger and poorly dispersed n- TiO_2 clusters. Conversely, gaseous NO_x , due to the much smaller dimensions, 100 pm – 200 pm⁶³, can easily penetrate both m- TiO_2 and n- TiO_2 clusters and the higher specific surface area for n- TiO_2 (measured by N_2 adsorption) plays obviously a key role as expected.

The surface chemistry approach presented here to interpret and justify the photocatalytic performances versus RhB and NO_x previously described has been published on the Journal of the American Ceramic Society⁶⁴.

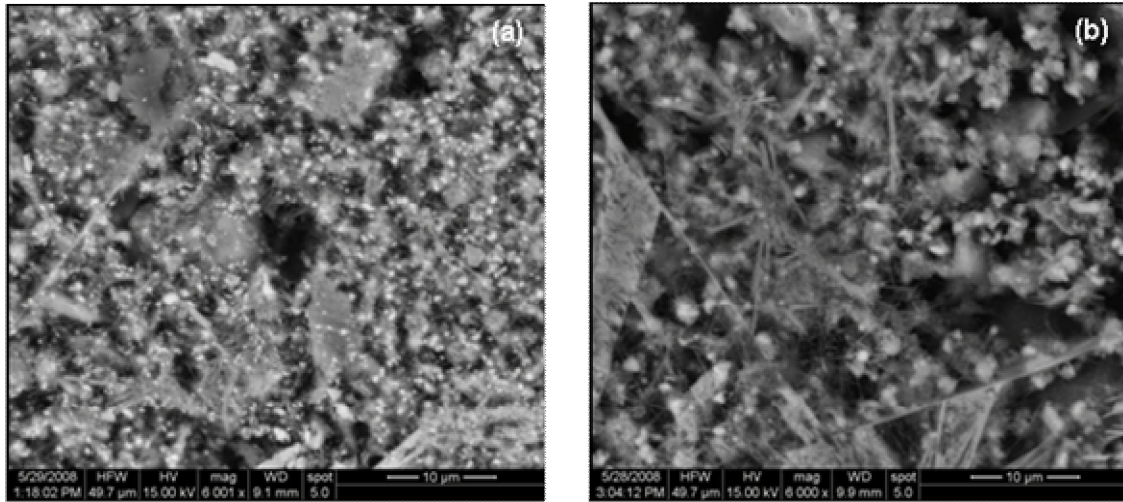


Figure 3.36 – SEM surface micrographs for cement specimens (1 day cured) prepared with: (a) m-TiO₂, (b) n-TiO₂. SEM conditions adopted: no impregnation, no coating, low vacuum mode.

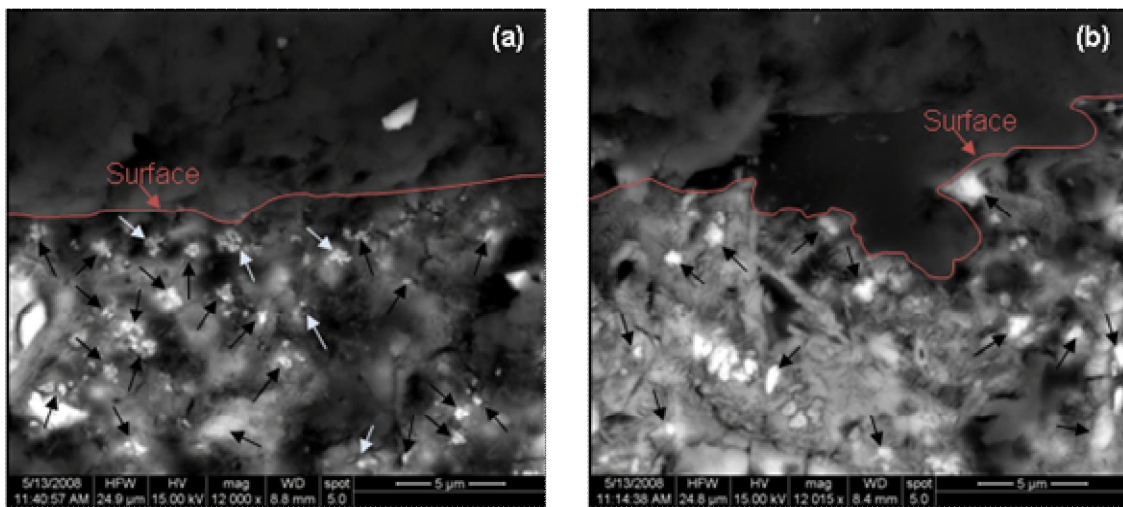


Figure 3.37 – SEM polished cross section micrographs for cement specimens (1 day cured) prepared with: (a) m-TiO₂, (b) n-TiO₂. SEM conditions adopted: impregnation⁶⁵,
⁶⁶, no coating, low vacuum mode.

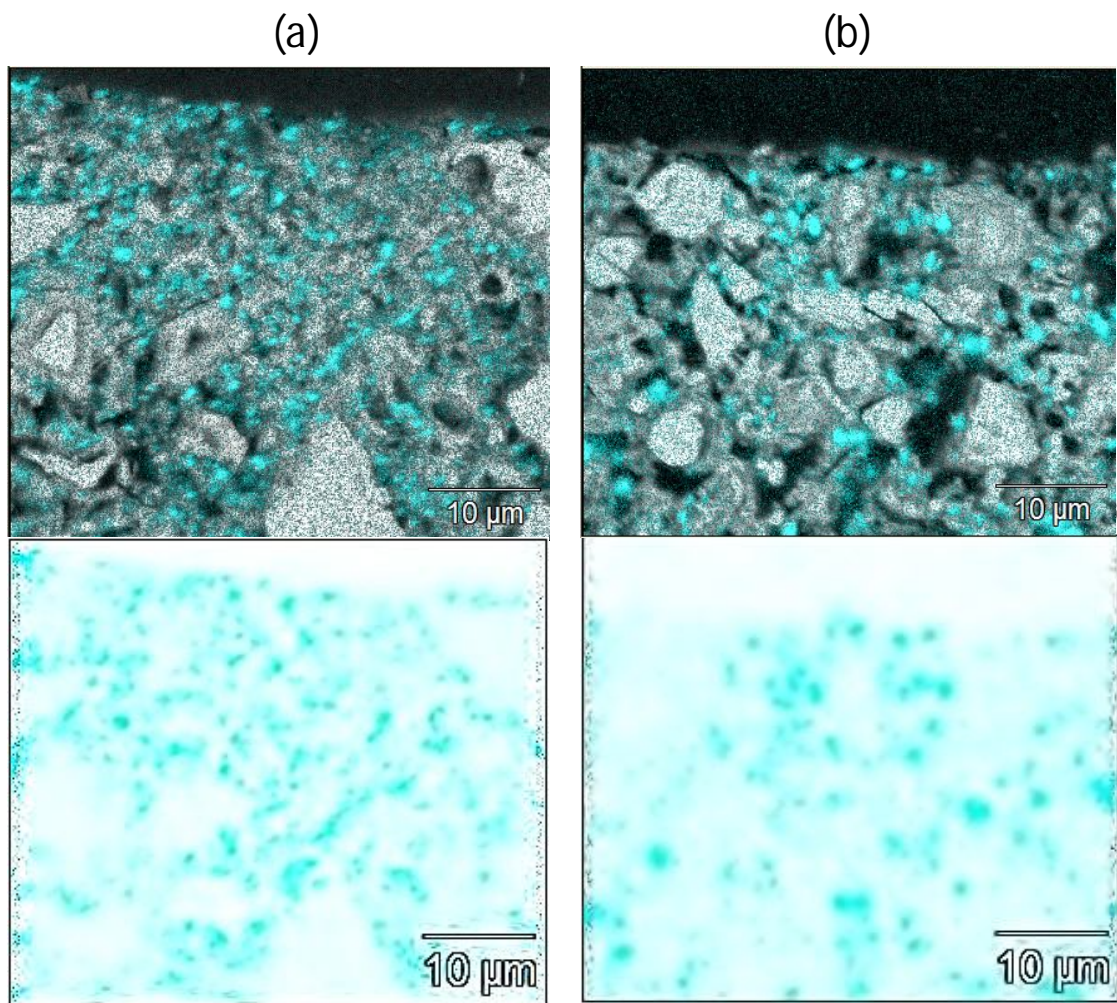


Figure 3.38 – SEM polished cross section micrographs for cement specimens (14 days cured) prepared with: (a) m-TiO₂, (b) n-TiO₂. SEM conditions adopted: impregnation⁶⁵,
⁶⁶, C coating, high vacuum mode.

3.3. Pilot test

3.3.1. Surface texture and surface microstructure design and engineering

Scanning electron micrographs in Figure 3.39 and Figure 3.40 show the surface microstructure obtained using, as casting surfaces, Zemdrain™ casting membrane and P 320 SiC paper respectively (section 2.5.1).

Surface texture obtained using the Zemdrain™ casting membrane (Figure 3.39) is characterised by a high degree of porosity leading to a highly open microstructure. On the other hand, although the surface obtained using the P 320 SiC paper showed a high degree of porosity too, the microstructure appears less open than the one obtained with the Zemdrain™ casting membrane. In fact Figure 3.40 shows a surface considerably covered with a layer that by SEM (backscattered electrons) appears lighter than the rest of the cement paste structures. EDS analysis showed that this layer is Portlandite, i.e. Ca(OH)_2 . During early setting (within 1 day from casting), water is trapped as a thin film between the SiC paper and the forming cement surface (Figure 2.19). This thin film of water provides a site for enhanced Portlandite formation on the cement surface. Portlandite is known to crystallise as thin plates, either parallel to the cement surface or perpendicular to it and deep into the forming structure, as evidenced by SEM images (Figure 3.40). Large portlandite plates on the cement surface might however have a negative effect on the self-cleaning properties of the cementitious structure containing TiO_2 . Figure 3.41 shows a magnified area of Figure 3.40, where Ca(OH)_2 plates cover and occlude TiO_2 particle agglomerates. In section 3.2.3.2 we highlighted that big molecules (like RhB) tend to be adsorbed on the surface and do not penetrate inside the cement structure. Clearly high levels of surface Ca(OH)_2 coverage may obstruct the adsorption of target molecules on TiO_2 particles.

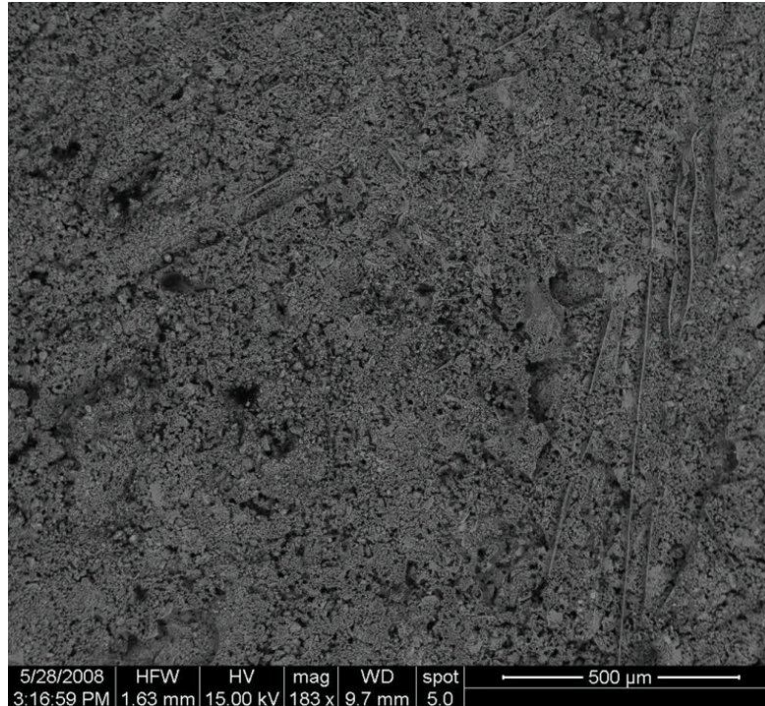


Figure 3.39 – Cement front casting surface obtained with Zemdrain™ membrane.

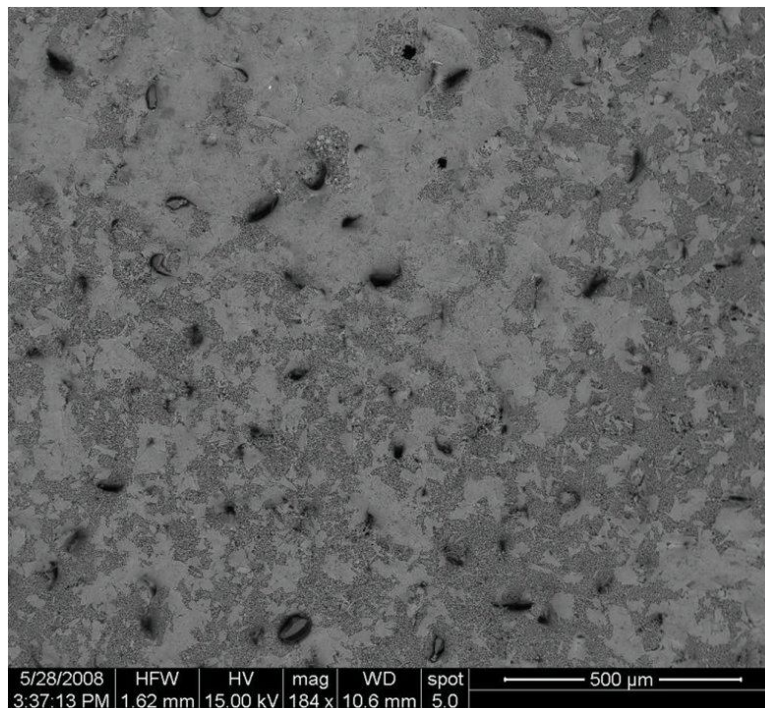


Figure 3.40 – Cement front casting surface obtained with P 320 SiC paper.

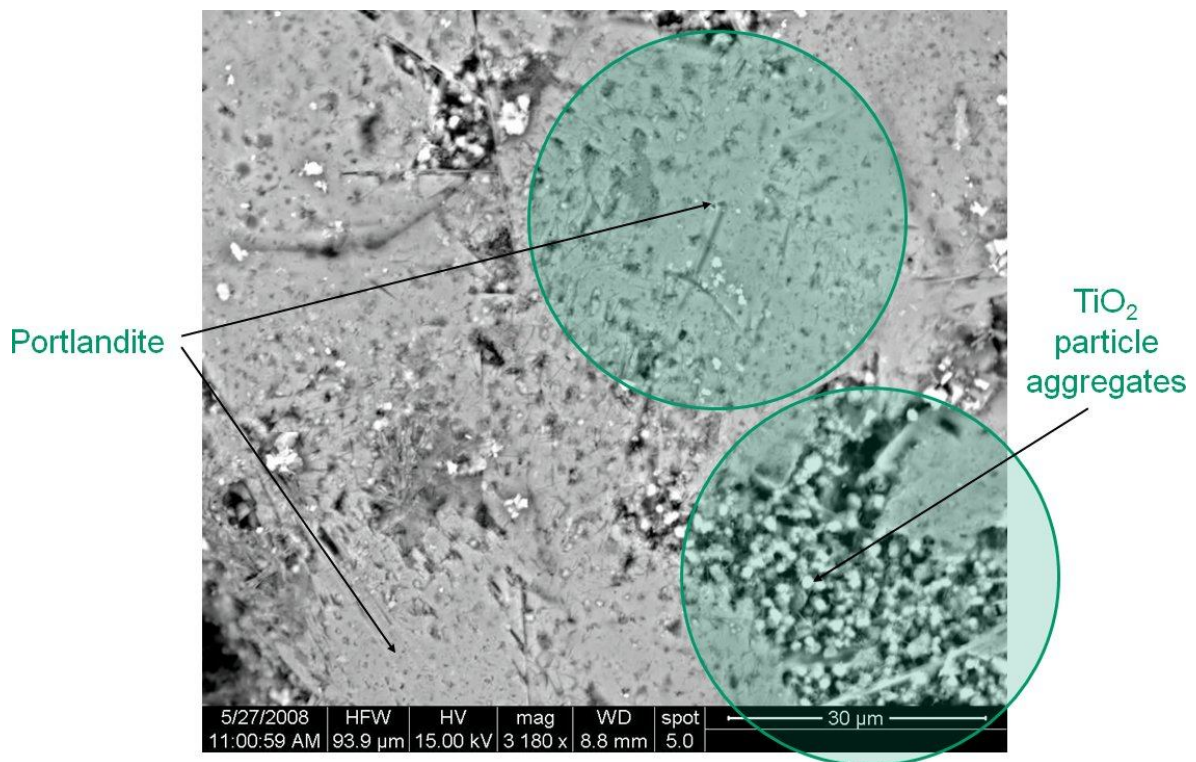


Figure 3.41 – Cement front casting surface obtained with P 320 SiC paper, magnified detail of Figure 3.40.

3.3.2. Aesthetic durability – Accelerated weathering test

Results for the accelerated weathering test conducted on white cement mortars containing (section 2.5.2) either m-TiO₂ or n-TiO₂ and with different surface finishing are shown in Figures 3.42, 3.43 and 3.44. S1, S2 and S3 are mortars with no photocatalyst and with flat and smooth surface, rough surface obtained with Zemdrain™ membrane and rough surface obtained with P 320 SiC paper respectively. These represent the controls used since they do not contain any photocatalyst. S1PM, S2PM, S3PM, S1PN, S2PN and S3PN are mortars with surface finishing corresponding to S1, S2, S3 but with either m-TiO₂ (PM) or n-TiO₂ (PN).

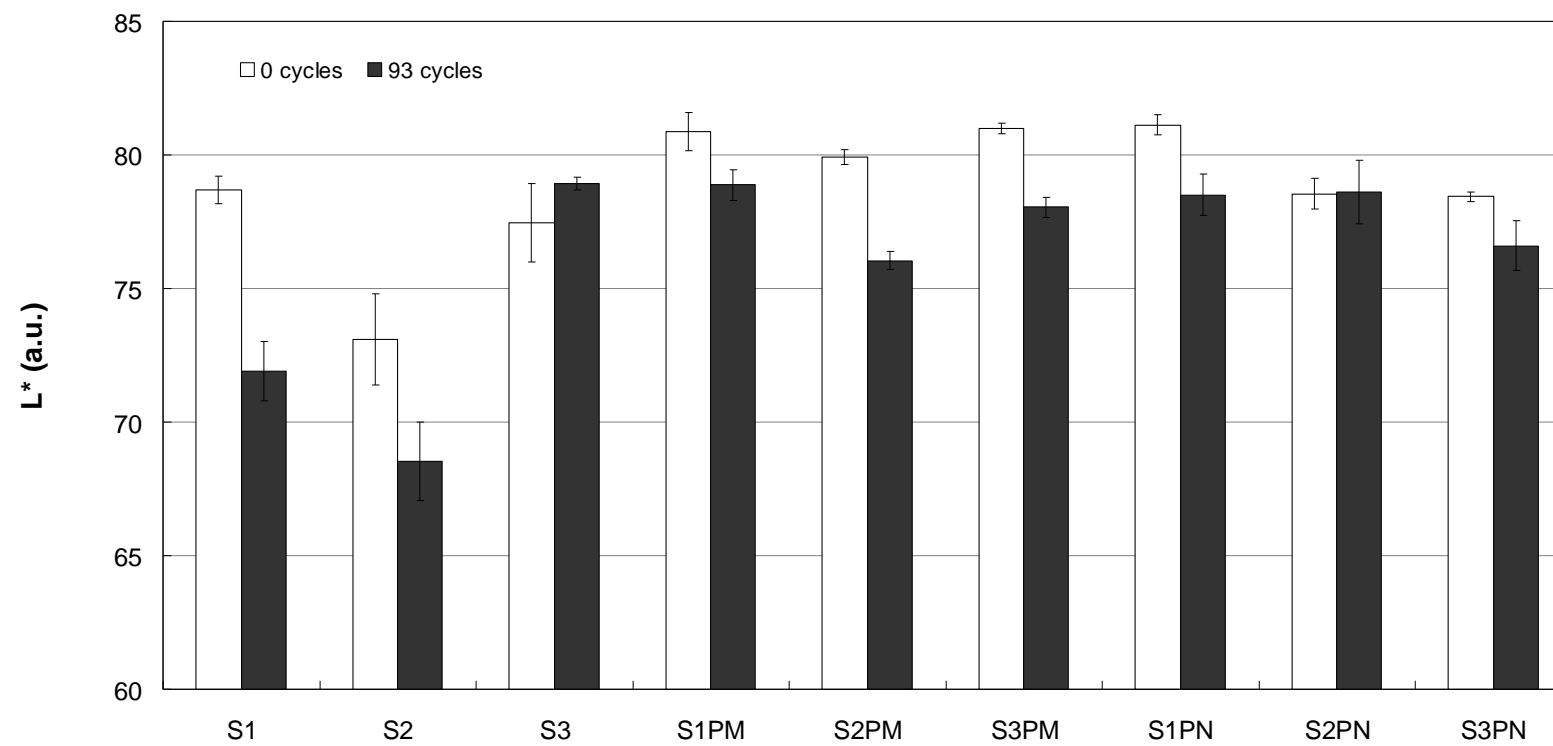


Figure 3.42 – Accelerated weathering test; L* axis (lightness).

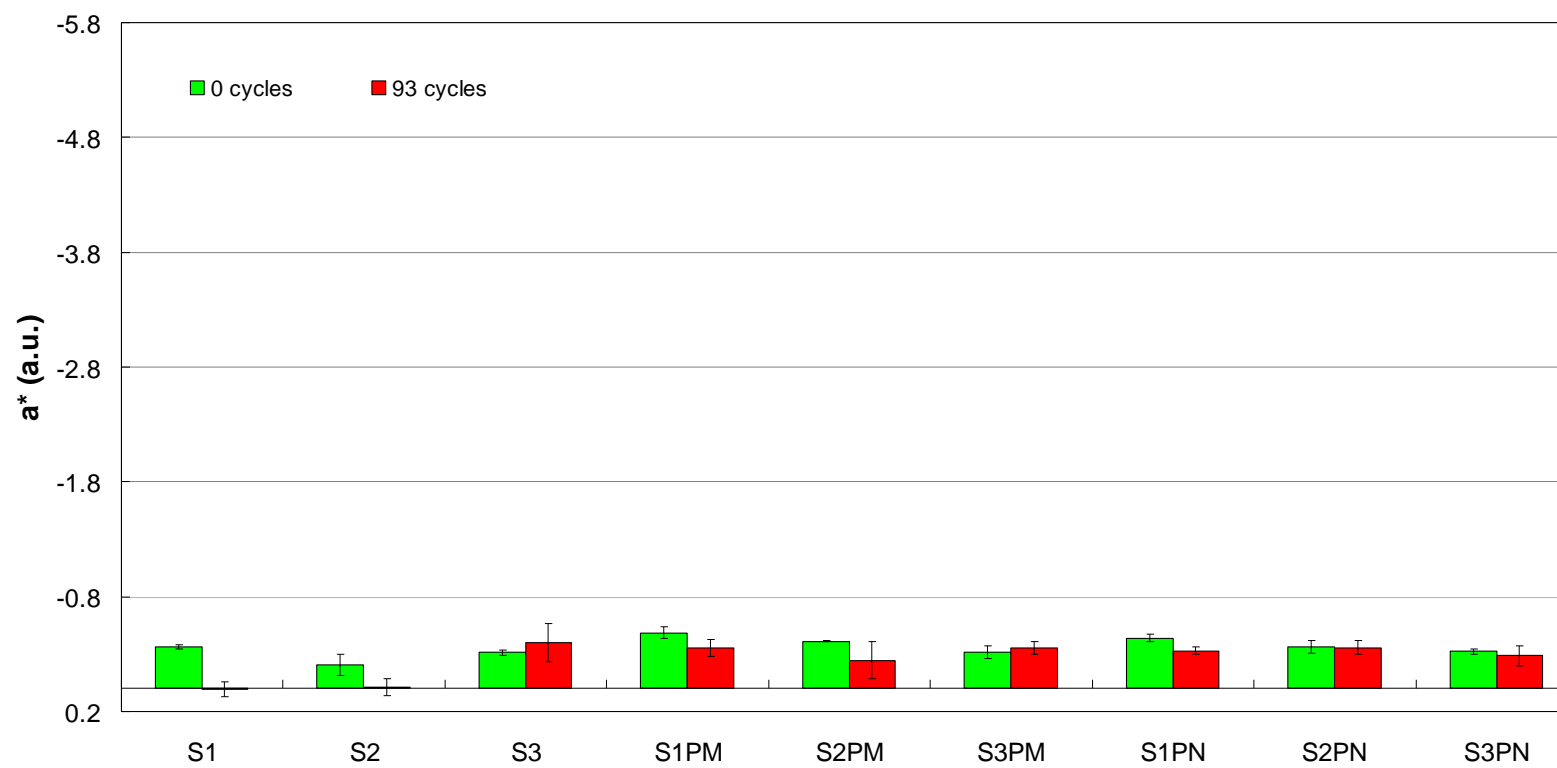


Figure 3.43 – Accelerated weathering test; a^* axis (red - green component).

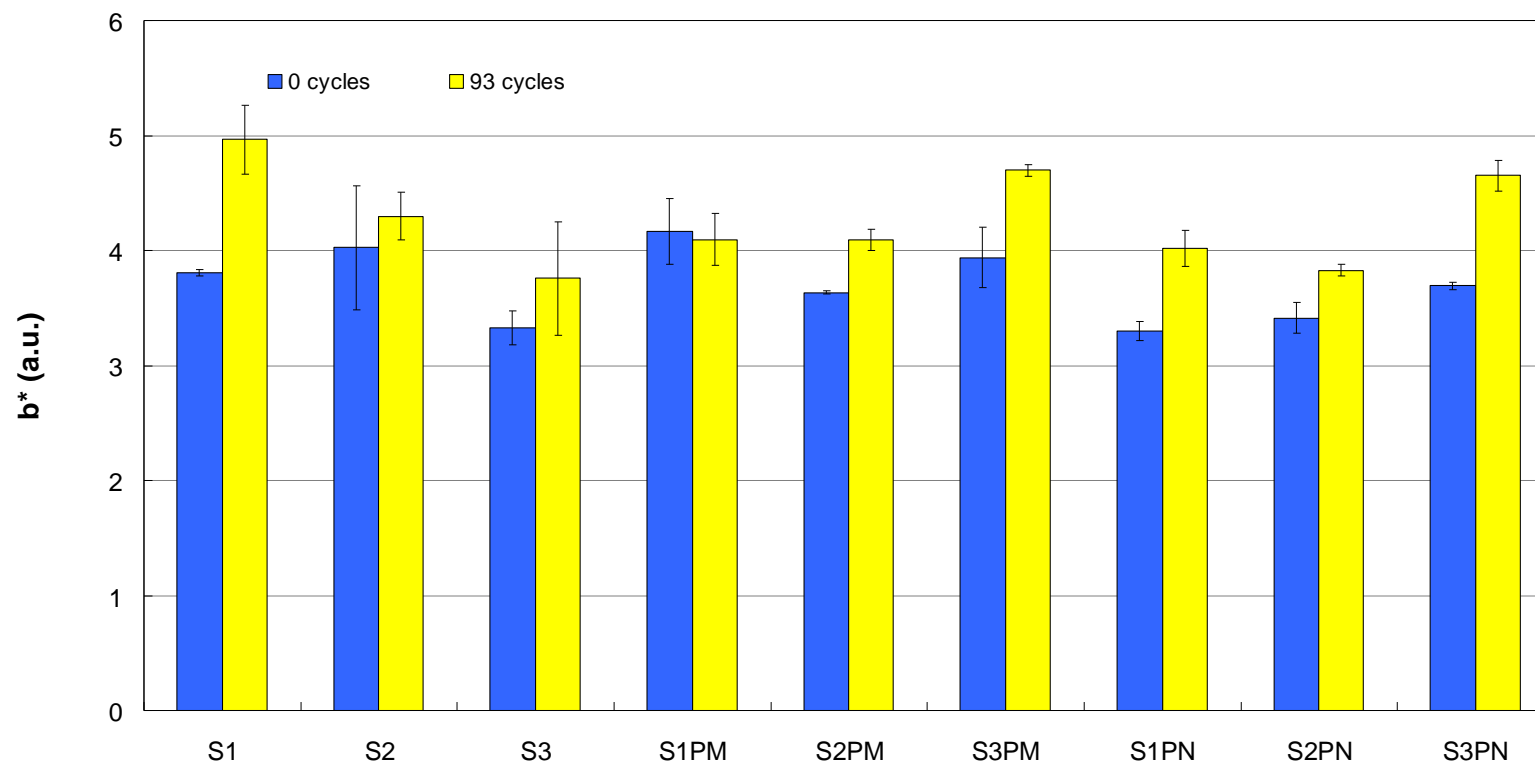


Figure 3.44 – Accelerated weathering test; b* axis (yellow – blue component).

In Figures 3.42 and 3.43, excluding the three samples with no photocatalyst (S1, S2 and S3), the values of lightness and red – green component for samples containing m-TiO₂ and n-TiO₂ showed no significant differences between the two rough surfaces compared to the flat and smooth one. The initial and final values measured for these colour parameters are comparable within the experimental errors. In Figure 3.44, for samples containing photocatalysts, surfaces prepared with P 320 SiC paper seemed to perform slightly worse than the others, however differences are not large. These observations clearly highlights that in terms of erosion and soiling the three surfaces prepared behave similarly. Due to this, parameters measured for mortars with no photocatalyst, with m-TiO₂ and with n-TiO₂ can be averaged over the three surfaces to better highlight the influence of the photocatalysts. Results are shown in Figures 3.45, 3.46 and 3.47.

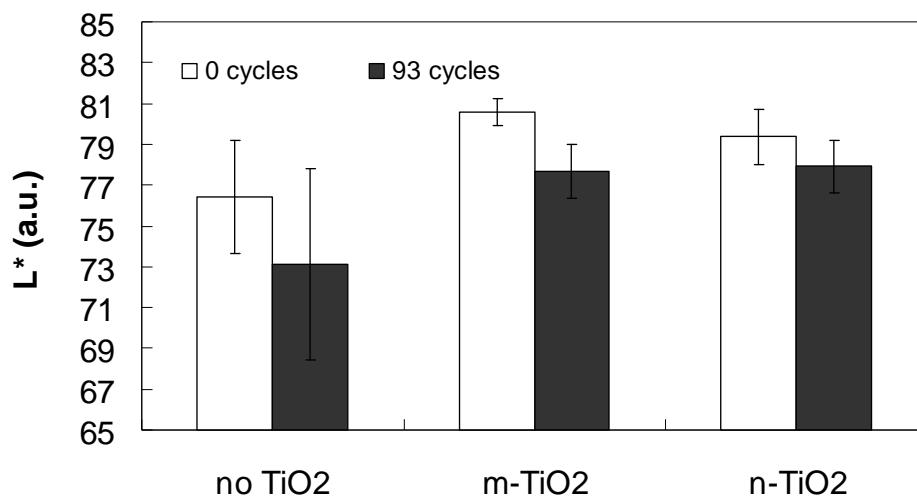


Figure 3.45 – Accelerated weathering test; L* axis (lightness), average values.

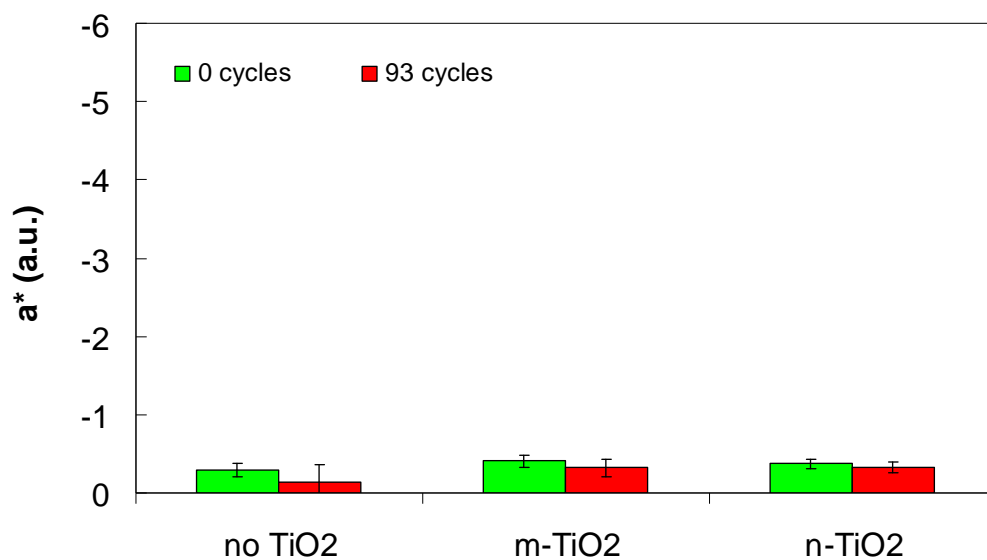


Figure 3.46 – Accelerated weathering test; a^* axis (red – green component), average values.

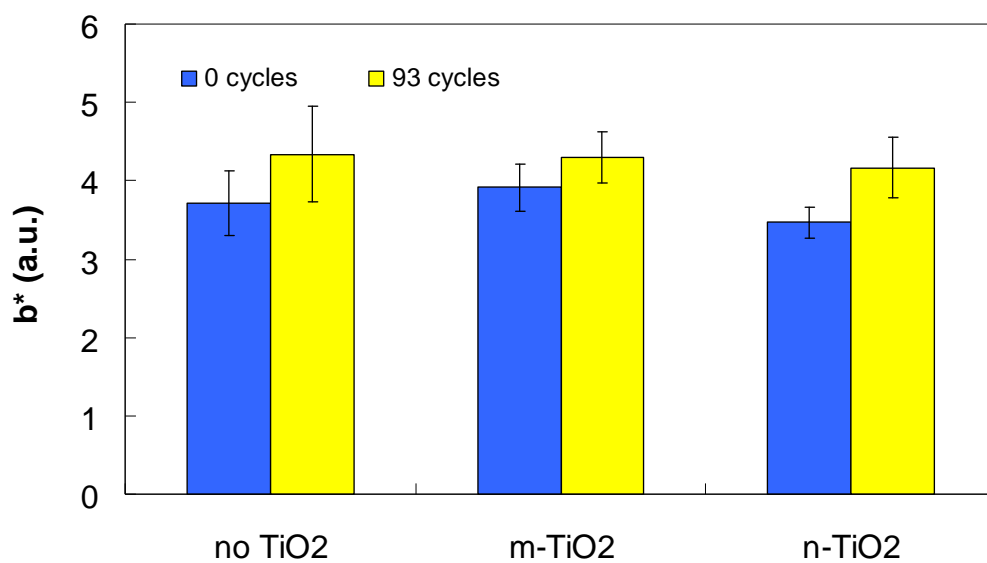


Figure 3.47 – Accelerated weathering test; b^* axis (yellow – blue component), average values.

Figures 3.46 and 3.47 show no significant benefit due to the presence of TiO_2 in the mortar structure, however Figure 3.45 clearly exhibits that mortars containing TiO_2 are whiter, when prepared, and remain whiter in time if TiO_2 is present. The effect of the intermixed TiO_2 is essentially dual:

- i. *Filler effect*: when intermixed, the very fine TiO_2 (in this case there is no great difference between m- TiO_2 and n- TiO_2) densifies the surface in much the same way as micro-silica or other fine fillers do. TiO_2 or any other fine filler therefore undoubtedly improve erosion resistance and reduce the amount of soiling penetrating the pores;
- ii. *Pigmentation effect*: white TiO_2 is the standard white pigment for a wide range of products to increase reflectance. This is not related to the ageing or the ageing resistance and would be obtained just as effectively with standard rutile TiO_2 of same fineness.

Benefits towards erosion and soiling resistances obtained by introducing TiO_2 in mortars are therefore not directly related to the photocatalytic activity of anatase TiO_2 . They are rather beneficial *side effects* that TiO_2 offers since it also behaves as a filler and white pigment.

References

1. H. Lin, C. P. Huang, W. Li, C. Ni, S. Ismatshah and Y. Tseng, *Appl. Catal. B-Environ.*, 2006, **68**, 1-11.
2. G. Burgeth and H. Kisch, *Coord. Chem. Rev.*, 2002, **230**, 41-47.
3. S. Sakthivel and H. Kisch, *Angew. Chem. Int.*, 2003, **42**, 4908-4911.
4. A. Mills and S. Le Hunte, *J. Photochem. Photobiol. A*, 1997, **108**, 1 - 35.
5. ATOMS_Software.
6. Bruker_EVA_X-ray_diffraction_pattern_database, *EVA X-ray diffraction pattern database*.
7. B. D. Cullity and S. R. Stock, *Elements of X-Ray Diffraction*, 3rd edn., Prentice-Hall Inc., 2001.
8. R. Jenkins and R. L. Snyder, *Introduction to X-Ray Powder Diffractometry*, 1st edn., John Wiley & Sons Inc., 1996.
9. J. Trimboli, M. Mottern, H. Verweij and P. K. Dutta, *J. Phys. Chem. B*, 2006, **110**, 5647-5654.
10. M. A. Henderson, *Langmuir*, 1996, **12**, 5093-5098.
11. M. A. Henderson, W. S. Epling, C. H. F. Peden and C. L. Perkins, *J. Phys. Chem. B*, 2002, **107**, 534-545.
12. P. Liu, W. Duan, W. Liang and X. Li, *Surf. Interface Anal.*, 2009, **41**, 394-398.
13. X. Fu, W. A. Zeltner and M. A. Anderson, *Stud. Surf. Sci. Catal.*, 1996, **103**, 445.
14. A. Iacomino, G. Cantele, D. Ninno, I. Marri and S. Ossicini, *Phys. Rev. B*, 2008, **78**, 075405.
15. N. D. Parkyns, in *Chemisorption and Catalysis*, ed. P. Hepple, Elsevier, London, 1970, pp. 150-171.
16. L. Alarcon-Ruiz, G. Platret, E. Massieu and A. Ehrlacher, *Cem. Conc. Res.*, 2005, **35**, 609-613.
17. A. G. Foster, *Trans. Farad. Soc.*, 1932, **28**, 645-657.
18. P. Stefanov, M. Shipochka, P. Stefchev, Z. Raicheva, V. Lazarova and L. Spassov, *J. Phys.*, 2008, **100**, 1-4.
19. Y. L. Lin, T. J. Wang and Y. Jin, *Powder Tech.*, 2002, **123**, 194-198.
20. J. Pouilleau, D. Devilliers, H. Groult and P. Marcus, *J. Mater. Sci.*, 1998, **32**, 5645.
21. A. Iwabuchi, C. Choo and K. Tanaka, *J. Phys. Chem. B*, 2004, **108**, 10863-10871.
22. , 1996.
23. F. Chen, J. Zhao and H. Hidaka, *Intern. J. Photoenergy*, 2003, **5**, 209-217.
24. N. Mandzy, E. Grulke and T. Druffel, *Powder Tech.*, 2005, **160**, 121-126.
25. Y. Masuda and K. Kato, *Cryst. Growth and Design*, 2008, **8**, 3213-3218.
26. B. P. Nelson, R. Candal, R. M. Corn and M. A. Anderson, *Langmuir*, 2000, **16**, 6094-6101.
27. D. J. Shaw, *Introduction to Colloid and Surface Chemistry*, Butterworths, London, 1966.
28. C. Kormann, D. W. Bahnemann and M. R. Hoffmann, *Environ. Sci. Tech.*, 1991, **25**, 494-500.
29. B. V. Derjaguin and L. P. Landau, *Acta Phys. Chim. USSR*, 1941, **14**, 633.
30. E. J. W. Verwey and G. T. J. Overbeek, *Theory and stability of lyophobic colloids*, Elsevier, Amsterdam, 1948.
31. Z. Jingxian, J. Dongliang, L. Weisensel and P. Greil, *J. Eur. Ceram. Soc.*, 2004, **24**, 2259-2265.
32. G. T. J. Overbeek, *Pure Appl. Chem.*, 1980, **52**, 1151-1161.

33. C. Labbez, B. Jönsson, M. Skarba and M. Borkovec, *Langmuir*, 2009, **25**, 7209-7213.
34. C. Labbez, A. Nonat, I. Pochard and B. Jönsson, *J. Colloid Interf. Sci.*, 2007, **309**, 303-307.
35. J. Lyklema, *Colloid Surface A*, 2006, **291**, 3-12.
36. B. Jönsson and H. Wennerström, *J. Adhes.*, 2004, **80**, 339-364.
37. L. Guldbrand, B. Jönsson, H. Wennerström and P. Linse, *J. Chem. Phys.*, 1984, **80**, 2221.
38. B. Jönsson, A. Nonat, C. Labbez, B. Cabane and H. Wennerström, *Langmuir*, 2005, **21**, 9211-9221.
39. C. Labbez, B. Jönsson, I. Pochard, A. Nonat and B. Cabane, *J. Phys. Chem.*, 2006, **110**, 9219-9230.
40. F. Mange, P. Couchot, A. Foissy and A. Pierre, *J. Colloid Interf. Sci.*, 1993, **159**, 58-67.
41. Z. Tang, L. E. Scriven and H. T. Davis, *J. Chem. Phys.*, 1992, **97**, 9258.
42. J. P. Valleau, R. Ivkov and G. M. Torrie, *J. Chem. Phys.*, 1991, **95**, 520.
43. H. Wennerström and B. Jönsson, *J. Phys. France*, 1988, **49**, 1033.
44. P. Attard, *Adv. Chem. Phys.*, 1996, **92**, 1-159.
45. M. Quesada-Perez, E. Gonzalez-Tovar, A. Martin-Molina, M. Lozada-Cassou and R. Hidalgo-Alvarez, *ChemPhysChem*, 2003, **4**, 234-248.
46. F. A. Cotton and G. Wilkinson, *Advanced Inorganic Chemistry*, 5 edn., Wiley-Interscience, USA, 1988.
47. A. G. Volkov, S. Paula and D. W. Deamer, *Bioelectrochem. Bioenerg.*, 1997, **42**, 153-160.
48. A. J. Rutgers and Y. Hendriks, *Trans. Farad. Soc.*, 1962, **58**, 2184-2191.
49. H. Binder and O. Zschornig, *Chem. Phys. Lipids*, 2002, **115**, 39-61.
50. M. R. Böhmer, Y. E. A. Sofy and A. Foissy, *J. Colloid Interf. Sci.*, 1994, **164**, 126-135.
51. Y. F. Houst, P. Bowen, F. Perche, A. Kauppi, P. Borget, L. Galmiche, J.-F. Le Meins, F. Lafuma, R. J. Flatt, I. Schober, P. F. G. Banfill, D. S. Swift, B. O. Myrvold, B. G. Petersen and K. Reknes, *Cem. Conc. Res.*, 2008, **38**, 1197-1209.
52. A. Folli, U. H. Jakobsen, G. L. Guerrini and D. E. Macphee, *J. Adv. Oxid. Technol.*, 2009, **12**, 126-133.
53. S. Devahasdin, C. J. Fan, K. Li and D. H. Chen, *J. Photochem. Photobiol. A*, 2003, **156**, 161-170.
54. H. Wang, Z. Wu, W. Zhao and B. Guan, *Chemosphere*, 2007, **66**, 185-190.
55. E. Revertegat, C. Richet and P. Gégout, *Cem. Conc. Res.*, **22**, 259-272.
56. D. F. Ollis, *Ind. Eng. Chem. Res.*, 2002, **41**, 6409-6412.
57. A. Chen, G. Lu, Y. Tao, Z. Dai and H. Gu, *Mater. Phys. Mech.*, 2001, **4**, 121-124.
58. M. R. Hoffmann, S. T. Martin, W. Choi and D. W. Bahnemann, *Chem. Rev.*, 1995, **95**, 69-96.
59. K. Hashimoto, K. Wasada, N. Toukai, H. Kominami and Y. Kera, *J. Photochem. Photobiol. A*, 2000, **136**, 103-109.
60. W. L. Masterton, D. Bolocofsky and T. P. Lee, *J. Phys. Chem.*, 1971, **75**, 2809-2815.
61. UNI_11247, 2009, 1-11.
62. C. H. Hou, X. Wang, C. Liang, S. Yiacoumi, C. Tsouris and S. Dai, *J. Phys. Chem. B*, 2008, **112**, 8563-8570.
63. A. F. Wells, *Structural Inorganic Chemistry*, 5th edn., Oxford University Press, Oxford, UK, 1984.
64. A. Folli, I. Pochard, A. Nonat, U. H. Jakobsen, A. M. Shepherd and D. E. Macphee, *J. Am. Ceram. Soc.*, 2010, **93**, 3360-3369.
65. U. H. Jakobsen, D. R. Brown, R. J. Comeau and J. H. H. Henriksen, in *Eurosem*, 2003.
66. U. H. Jakobsen, L. Laugesen and N. Thaulow, in *SP 191*, 2000, vol. Water-Cement ratio and other Durability Parameters: Techniques for determination.

Conclusions and Future Work

Application of TiO_2 photocatalysis to cement and concrete provides an efficient strategy to simultaneously obtain: self-cleaning of building facades, retardation of natural surface ageing as well as air pollution mitigation, simply with the support of sunlight, atmospheric oxygen and water present as humidity and/or rain water. In this PhD project, performances in degrading rhodamine B, RhB, (a common industrial test to evaluate self-cleaning activities), ability to retard natural ageing caused by processes such as soiling and erosion and performances in oxidising nitrogen oxide gaseous pollutants, NO_x , are presented for two different TiO_2 samples tested in cement and mortars, together with an insight into the fundamental chemistry about TiO_2 photosensitised reactions responsible for the degradation processes involved.

Discolouration of RhB on TiO_2 in cement involves not only a proper photocatalytic mechanism (TiO_2 – sensitised photoreaction) but also a dye – sensitised pathway. In the first mechanism light activates TiO_2 through promotion of electrons from the valence band to the conductance band. Adsorbed water and oxygen react with valence band positive holes (left after promotion) and conductance band electrons respectively to generate hydroxyl radicals, $\text{HO}\cdot$, which ultimately degrade the adsorbed dye. In the second mechanisms, electrons in the HOMO level of the dye undergo transitions to the LUMO level and are subsequently injected into the conductance band of TiO_2 . These electrons are therefore used by oxygen to generate oxidative species which degrade the already partially reacted dye. Dye – sensitised pathways are predominant when the system TiO_2/RhB is irradiated with visible light. The lower energies available from visible light are insufficient to induce photo-activation of TiO_2 but they can lead to dye sensitisation and degradation of colour by this mechanism. In these conditions, if RhB adsorbs on the TiO_2 surface through the positively charged amino groups (most likely since TiO_2 surfaces in highly alkaline conditions are negatively charged), a selective stepwise de-ethylation of RhB amino groups occurs. This mechanism is responsible for a sequence of structurally similar degradation products which absorb radiation at progressively lower wavelengths (hypsochromic shift in the UV-vis diffuse reflectance spectra). These findings, related to the photocatalytic degradation of RhB on photoactivated TiO_2 supported on cementitious materials, match very well what is already observed for slurry suspensions in terms of influence of the incident radiation.

The oxidation of NO_x on the other hand uniquely follows a photocatalytic pathway, where nitric oxide, NO, and nitrogen dioxide, NO₂, are oxidised to nitric acid, HNO₃, which, in the cement environment, readily transforms into nitrates, NO₃⁻ due to the high pH of the system. Furthermore, the oxidation of NO is assumed to go through an initial stage of fast NO reactive photoadsorption with formation of NO₂ which approaches a transition stage (and later on a pseudo steady state) where NO₂ is converted to NO₃⁻. All the steps from NO to NO₃⁻ in the regimes observed have been found to be ·OH radical – dependent, hence water content – dependent. Water consumption on the TiO₂ surface (if not continuously supplied) and irreversibly adsorbed NO₃⁻ species may be considered as the main factors for catalyst deactivation. Furthermore, kinetic data coupled with spectroscopic evidences about TiO₂ surface hydration also showed that in the photocatalytic formation of NO₃⁻, dissociated and molecular chemisorbed water is much more active than H – bonded molecular water. This general mechanism of NO_x oxidation on light sensitised TiO₂ is considered valid also in the case of TiO₂ contained in cementitious systems. It is believed that the much higher pH has the effect of readily transforming HONO and HNO₃ into NO₂⁻ and NO₃⁻. However more research is needed to identify if the high pH has any effect towards the stabilisation of the reaction intermediates, i.e. NO₂⁻, that in aqueous solution are known to be much more stable than their conjugated acid, HONO.

The study has also linked photocatalytic performances to TiO₂ surface/colloidal chemistry and structure of TiO₂ clusters in cement. TiO₂ primary and secondary particle size, dispersion and agglomerate porosity in cement define accessible surface area. In a highly coupled system like cement (high surface charge densities and presence of multivalent cations), ion-ion correlation forces in the electrical double layer can be at the origin of TiO₂ surface overcharging phenomena and apparent surface charge reversal. Ion-ion correlations introduce an attractive electrostatic contribution between particles with the same charges that is ultimately responsible for enhanced agglomeration of TiO₂ crystallites. This results in a bigger secondary particle size (size of the crystallite agglomerates) when compared to non-highly coupled systems (low surface charge densities and presence of monovalent cations and indifferent electrolytes). However the degree of agglomeration has been proven to be very different when comparing m-TiO₂

with n-TiO₂. The much smaller specific surface area and the surface chemical modification with P generating surface P – OH groups with a very different pK_a when compared with Ti – OH groups, are responsible for a much lower degree of agglomeration for m-TiO₂. As a result m-TiO₂ shows smaller and better dispersed agglomerates than n-TiO₂ even though the primary particle size (crystallite size) is bigger. Big particle agglomerate pores, small and highly dispersed agglomerates of m-TiO₂ offer a higher available surface area for adsorption and reaction of big molecules like RhB which hardly penetrate n-TiO₂ particle agglomerate pores. On the other hand, very small molecules like nitrogen oxides which can easily penetrate into n-TiO₂ agglomerate pores too, are better degraded by n-TiO₂. Indeed in this case, dispersion and agglomerates porosity are not crucial; the available surface area is most likely to be due to the specific surface area determined by primary particle size.

Not least in importance, an accelerated ageing test conducted on mortars containing TiO₂ revealed that the presence of titania is also beneficial to retard deterioration of facades (by erosion and soiling) due to its filler and pigmentation effects.

The present study has also allowed identification of key aspects that may be the subject for future works. The first one is related to the overall efficiency of TiO₂ in cement in relation to the surface/colloidal chemistry which defines particle agglomeration and dispersion in cement matrixes. Effective surface modifications to inhibit massive particle agglomeration in n-TiO₂ in cement for example should lead to a much higher *available* surface area for big molecules (like RhB) to be adsorbed, therefore increasing the degradation rate of large molecule pollutants. In this way, it might be possible to obtain a multifunctional concrete element with optimised performances for self-cleaning and depollution using one TiO₂ sample only. A second key issue is related to a potential negative impact on the cementitious structure associated with the acidic species produced during the oxidation of NO and NO₂. Over very long time periods, nitric acid produced by the oxidation of NO and NO₂ might lead to partial decalcification of the calcium silicate hydrate (C-S-H) phase. Investigations in this direction and accurate mass balances are required to quantitatively assess the impact of photocatalytic oxidation products. However this can be rather complex and evidences for such calculations have not yet been found. Finally, as already mentioned above, further research is needed to identify if

some NO_x oxidation intermediates are stabilised by the very high pH of the system, causing changes in the overall oxidation mechanism. If so, carbonation of cement would have to be taken into account too, since it causes pH to drop over time.

The work here presented has served as a solid experimental and theoretical support to design a new EU funded project (FP7 Eco Innovation Scheme) called **Visible Light Active PhotoCATalytic Concretes for Air Pollution Treatment (Light²CAT)**. This new project, starting in early 2012, will be dealing with the development of a new generation of photocatalytic cementitious materials and concretes implementing visible light sensitive TiO₂s as well as tackling those issues described before that yet need to be addressed. The methods to obtain visible light sensitization will be scanned over a wide range of techniques such as: metal ion coupling, selective surface hydrogenation as well as crystal structure engineering to alter the ordinary band structure of the TiO₂ semiconductor lattice. The main scope of Light²CAT is to significantly improve the performances of photocatalytic concretes in *Northern latitudes* where, due to atmospheric and sunlight conditions, the efficiencies of photocatalytic concretes based on ordinary TiO₂ cannot be as high as in Southern Europe (ordinary TiO₂ is activated by UV light only). Light²CAT involves 12 partners amongst Universities and Research Institutions, SMEs and larger multinational companies as well as public bodies and Governmental Institutions, over a total of 5 European Countries, namely: Denmark, Sweden, UK, Spain and Italy. Light²CAT project has a total budget of about 5 M € with an overall EU contribution equal to 3.6 M €